Durham E-Theses

Rapid Detection of Earthquake-triggered Landslides from Satellite Radar

KATY ALINE BURROWS

How to cite:

BURROWS, KATY ALINE (2020) Rapid Detection of Earthquake-triggered Landslides from Satellite Radar. Doctoral thesis, Durham University.

Use policy

Rapid Detection of Earthquake-triggered Landslides from Satellite Radar

Katy Burrows

A thesis presented for the degree of
Doctor of Philosophy

Department of Earth Sciences
The University of Durham
United Kingdom
26th October 2020

Rapid Detection of Earthquake-triggered Landslides from Satellite Radar
Katy Burrows

Abstract

Triggered landslides pose a major risk following large earthquakes in mountainous areas and disrupt emergency response efforts. If information on the spatial distribution of these landslides can be generated quickly enough, it is therefore invaluable to emergency response coordinators. At present, this information is commonly generated manually from optical satellite imagery, which is labour-intensive and can be delayed or left incomplete due to cloud cover. This means a complete picture of triggered landsliding is often unavailable within the time frame of the emergency response. Alternatively, empirical models can predict landslide probability based on factors such as shaking intensity and slope steepness within hours of an earthquake, but these models are static in time and not always reliable as they do not contain any observations of landslides.

Satellite radar offers a third alternative method of generating landslide information for emergency response. These data can be acquired through cloud and are now available within days of any continental earthquake. Radar data are sensitive to landslides, which alter the scattering properties of the Earth's surface, so could be used to generate all-weather information on landslide spatial distributions within days of an earthquake. Satellite radar data are routinely used to generate other products for emergency response, but for landslide detection, the testing and development of radar methods is not yet sufficiently advanced for them to be widely applied. In this thesis, I present new methods of landslide detection based on satellite radar coherence, a measure of the level of noise in an interferogram that reflects physical changes in the Earth's surface such as landslides. I carry out systematic testing of new and existing methods of coherence-based landslide detection across four case study earthquakes using data from two satellite radar sensors, allowing identification of which method is preferable depending on the data available after an earthquake. Finally I experiment with combining empirical models and radar coherence methods. Overall, I demonstrate that useful information on landslide intensity can be generated within two weeks of an earthquake using satellite radar data, and that the addition of these data to empirical models can significantly improve their performance.

Supervisors: Richard Walters, David Milledge, Alexander Densmore and Dino Bellugi

Acknowledgements

First I would like to acknowledge Rich Walters, Dave Milledge and Alex Densmore who have formed a brilliant supervisory team. I have learned a huge amount about radar, landslides, emergency response, statistics and research more generally from discussions with them, and could not have carried out this project without their help. I would also like to thank my fourth supervisor Dino Bellugi, who I was able to visit at the University of Berkeley, California and who provided lots of advice on the machine learning aspect of my project.

My PhD was funded through an 'Action on Natural Disasters' scholarship from the Institute of Hazard, Risk and Resilience at Durham University, and I am extremely grateful for the opportunities this programme provided. This PhD programme was funded by donors and my research would not have been possible without their generosity. I have also greatly benefited from the companionship of the other Action on Natural Disasters PhD scholars: Gopi, Samprada and Sheena.

I was also lucky enough to be a member of COMET during my PhD studies, which allowed me to interact with an InSAR community across the U.K. and provided access to training courses and meetings. In particular, Karsten Spaans was extremely helpful in setting up and explaining software used in Chapter 3.

I would also like to thank the postgraduate community in the Earth Science and Geography departments at Durham University, whose company, whether for tea, cake, pizza, walks or trips to the pub, has made my time in Durham far more enjoyable. In particular, thank you to Tammy, Madeleine, Katharine, Olly, Chris, Emma, Eloïse, Sean, Sarah, Miles, Tim, Nico and Simon. Finally I would like to thank Mathieu, my friends Jess, Sam, Lucy and Becca and my family, who are all simply great people that I am lucky to know.

Finally I would like to thank my examiners Nick Rosser and Sang-Ho Yun for their time in reading my thesis and conducting my viva, which was very enjoyable.

Contents

Declaration

The work in this thesis is based on research carried out at the Department of Earth Sciences, University of Durham, England. No part of this thesis has been submitted elsewhere for any other degree or qualification, and it is the sole work of the author unless referenced to the contrary in the text.

Publications

Some of the work presented in this thesis has been published in journals - the relevant publications are listed below. In each case, I was responsible for data processing and curation, development of the methodology and preparation of the manuscript. The text of both papers has been edited in some places to fit better within the thesis.

Chapter 3 has been published in the peer reviewed journal *Remote Sensing*

Burrows, K., Walters, R.J., Milledge, D., Spaans, K. and Densmore, A.L., A new method for large-scale landslide classification from satellite radar. *Remote Sensing*, 11(3), p.237. `https://doi.org/10.3390/rs11030237`, 11(3), p.237. 2019.

Chapter 4 is currently in review in the journal *Natural Hazards and Earth System Sciences*, and is available online as a discussion paper.

Burrows, K., Walters, R. J., Milledge, D., and Densmore, A. L., A Systematic Exploration of Satellite Radar Coherence Methods for Rapid Landslide Detection, *Nat. Hazards Earth Syst. Sci. Discuss.*, `https://doi.org/10.5194/nhess-2020-168`, in review, 2020.

List of Figures

List of Tables

Nomenclature

ALOS-2 Advanced Land Observing Satellite 2

AUC area under the curve

ARIA Advanced Rapid Imaging and Analysis

Bx-S boxcar - sibling

CSK COSMO SkyMed

DEM digital elevation model

DU Durham University

ESA European Space Agency

ROC receiver operating characteristic

ICIMOD International Centre for Integrated Mountain Development

InSAR Interferometric SAR

ISRO Indian Space Research Organisation

JAXA Japanese Space Agency

MAE mean absolute error

MDA MacDonald, Dettwiler and Associates Ltd.

MLI Multi-looked Intensity

NDVI Normalised Difference Vegetation Index

NGA National Geospatial-intelligence Agency

PALSAR-2 Phased-Array L-band Synthetic Aperture Radar 2

RMSE root mean squared error

SAR synthetic aperture radar

SLC Single-look complex

SRTM Shuttle Radar Topography Mission

USGS United States Geological Survey

Introduction

Triggered landslides following an earthquake disrupt emergency response efforts and have been shown to pose the highest risk to life of all secondary earthquake hazards (Marano et al., 2010). Landslides triggered by a single large earthquake can result in tens of thousands of fatalities. According to the dataset of Nowicki Jessee et al. (2020), there have been over 200,000 recorded fatalities due to earthquake triggered landslides between 1811 and 2016 (Figure 1.1). Triggered landslides also obstruct the emergency response to the earthquake and isolate remote communities through damage to power, communication and transportation infrastructure and can lead to further hazards such as dam-outburst floods (Cui et al., 2009; Global Logistics Cluster, 2015). Landslide inventories are thus compiled for two main reasons: first to inform the emergency response following the event (e.g. Kargel et al., 2016; Bessette-Kirton et al., 2019); and second to further our understanding of the physical slope failure processes that cause the landslides (e.g. Ferrario, 2019; Roback et al., 2018), informing risk assessment and susceptibility maps for future events.

1.1 Uses of landslide datasets and their information requirements

When generating landslide information either for emergency response or for research, the completeness and accuracy of the dataset are two of the most important considerations; however, beyond this, the two purposes have very different information requirements. Figure 1.2 shows an example of a landslide dataset compiled for research purposes following the M_w 7.0 2016 Kumamoto, Japan earthquake (Xu et al., 2018) and one compiled for emergency response following Hurricane Maria in Puerto-Rico (Bessette-Kirton et al., 2019). Both were generated using optical

Figure 1.1: Global map of earthquake-triggered landslide fatalities recorded between 1811-2016 (from Nowicki Jessee et al., 2020, Open and closed symbols represent whether or not the event was used in the modelling of that study.). Reproduced with permission from: Springer, Landslides, "A global dataset and model of earthquake-induced landslide fatalities" Nowicki-Jessee et al. © Springer-Verlag 2020

satellite imagery, but the end products are very different: individual landslide polygons were mapped by Xu et al. (2018), while Bessette-Kirton et al. (2019) have produced a map of gridded landslide density.

Detailed landslide inventories can be used for a wide range of research purposes. These include physical and empirical modelling of landslide hazard (e.g. Chang et al., 2007; Nowicki Jessee et al., 2018; Scaringi et al., 2018); estimations of sediment transport volumes associated with landslides (e.g. Li et al., 2016), which can affect geochemical cycles (Frith et al., 2018) and long-term landscape evolution (Li et al., 2014). For all of these applications, landslide inventories must be compiled in great detail, with landslides recorded as polygons (Harp et al., 2011). Care must be taken to avoid merging two adjacent landslides into a single event, as this would distort any empirical models generated from the inventory (Marc and Hovius, 2015). Information on the area and shape of each landslide is important, and in some cases, the source area and runout area of the landslides are recorded separately (e.g. Roback et al., 2018).

In an emergency response context, information on landslides following an earthquake is used to improve resource allocation. The speed at which the information is generated is therefore critical, as it must be available during the decision making process in order to be of use. As a guideline, for the data to be useful, they must be generated within two weeks of an event, and ideally an overview of the most severely impacted areas should be generated within 72 hours (Williams et al., 2018;
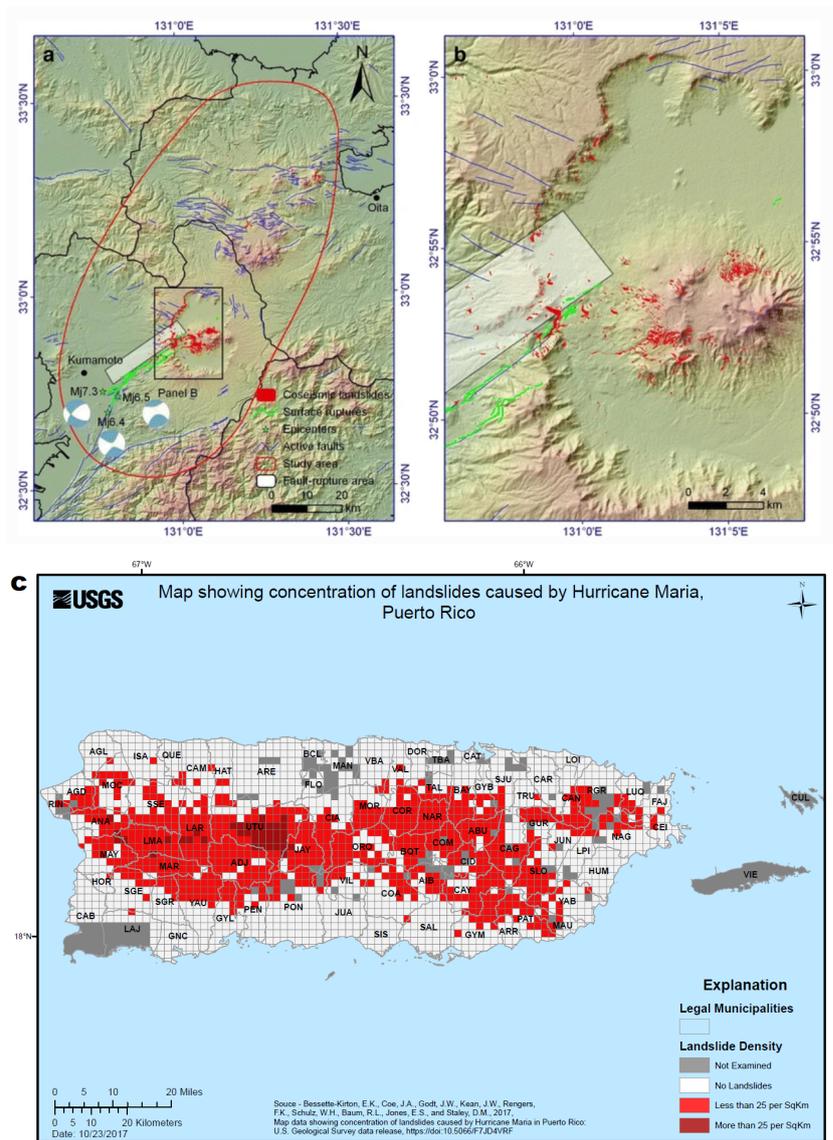
Figure 1.2: A comparison of landslide information types generated for two different purposes. (a,b) Polygon landslide inventory compiled for research following the 2016 Kumamoto earthquake (Reproduced with permission from: Springer, Nature, "Landslides triggered by the 2016 Mj 7.3 Kumamoto, Japan, earthquake", Chong Xu et al © Springer-Verlag 2017). (c) Gridded landslide information generated for emergency response in Puerto Rico following Hurricane Maria (reproduced from Bessette-Kirton et al., 2017, public domain)

Inter-Agency Standing Committee, 2015). Information on landslides generated in the first few days after an earthquake can be used to inform search and rescue efforts. It can also be used in conjunction with road maps to identify blocked routes (e.g. Robinson et al., 2018). This is important since damaged roads can limit access to hospitals for people injured in the earthquake, reducing their chance of survival (Fiedrich et al., 2000). Following this stage, landslide information can

be used to assess and mitigate against possible associated hazards. For example, it was expected that landslides triggered by the 2015 Gorkha, Nepal earthquake could reactivate during the monsoon season, which began around six weeks later, causing further damage (Datta et al., 2018). Information on landslides following this event was also used to guide flight routes for aerial investigation of potential landslide dams, which can lead to flash flooding (Collins and Jibson, 2015). On a longer timescale, landslide information is also used to guide rehabilitation both during the emergency response, for example in the case of repairs to critical road networks, and afterwards during the recovery phase of the response as decisions are made on where to rebuild infrastructure (Huang et al., 2012).

The range of uses of landslide information following an earthquake means that the information requirements thus evolve significantly throughout the emergency response. In the initial phases, the level of detail and precision of the landslide information is less important than the speed at which it can be generated. Currently landslide information during this period takes the form either of points (e.g. Kargel et al., 2016), as polylines (e.g. Williams et al., 2018) or as landslide density (e.g. Bessette-Kirton et al., 2019, Fig. 1.2c) or probability (e.g. Nowicki Jessee et al., 2018). Simplicity is also important at these early stages, as it is likely that non-experts will need to interpret the data quickly. In the later stages of earthquake response, when landslide information is used to guide rehabilitation, more precise information is needed on exactly where landslides occurred and their runout areas.

1.2 Methods of generating landslide information

When landslides are triggered across a wide area, it is not practical to carry out field investigations across the entire region. What is needed instead are methods for generating landslide information at a much larger scale. For this large-scale generation of landslide information, three main approaches exist. The most widely used is manual mapping with optical satellite imagery, which is done for both emergency response and research purposes. The second method is to use empirical models of landslide likelihood, which can generate information on the predicted spatial distribution of landslides within hours of a trigger event for emergency response purposes. Finally, the use of satellite radar data in landslide detection has emerged recently as a third alternative. In this thesis, I focus on satellite radar methods of landslide detection, but will also consider the advantages and disadvantages of optical mapping and empirical models.

1.2.1   Generation of landslide information with optical satellite imagery

The majority of landslide inventories are compiled using optical or multispectral satellite imagery (e.g. Bessette-Kirton et al., 2019; Ferrario, 2019; Kargel et al., 2016; Roback et al., 2018; Xu et al., 2018; Zhang et al., 2019). One advantage of using these data is their high spatial resolution, which allows identification of small landslides, precise information on landslide area and distinction between adjacent landslides. For example Ferrario (2019) uses Sentinel-2 (10 m resolution) and Planetscope (3 m resolution) satellite imagery to map landslides as small as 200 m^2. These data also allow landslides to be mapped with a high level of accuracy in comparison to empirical modelling. A third advantage of optical satellite data is that the process of manually identifying landslides in this kind of imagery is relatively easy to learn, allowing teams of mappers to work together following an earthquake, (e.g. Kargel et al., 2016; Williams et al., 2018). Despite this, manual mapping using optical satellite imagery is a time consuming and therefore expensive process. For landslide mapping in vegetated regions, automated methods based on the Normalised Difference Vegetation Index (NDVI) can be used to detect areas where landslides have removed vegetation, which can speed up the mapping process, although there is a tendency to incorrectly identify other objects, such as roads, as landslides (e.g. Behling et al., 2014; Borghuis et al., 2007; Deijns et al., 2020). However, there is another problem with using optical satellite imagery, which is insurmountable for landslide mapping: cloud cover.

Cloud cover can render optical satellite imagery unusable for landslide mapping by obscuring the Earth's surface. When generating landslide inventories for research purposes, this is not always a problem as it may be acceptable to wait several weeks following an earthquake before starting to map the landslides. However if multiple triggering events occur in succession, which is fairly common, it becomes difficult to assign landslides to one event or another if no cloud-free imagery is acquired between the events. For example, the inventory of 24,915 landslides manually compiled by Roback et al. (2018) following the 2015 M_w 7.8 Gorkha, Nepal earthquake contains 3,349 that were mapped using imagery acquired after the M_w 7.2 aftershock, which occurred 17 days following the mainshock, and 1,752 mapped from imagery that was not acquired until after the monsoon around five months later. Mapping the same event, Martha et al. (2017) attributed 213 of their 15,551 mapped landslides to the M_w 7.2 aftershock rather than to the mainshock. In the inventory of Ferrario (2019) of landslides triggered by the 2018 Lombok, Indonesia earthquake sequence, no usable optical imagery was acquired between the first two $M_w > 6.0$ earthquakes in the sequence. This lack of precise timing information is
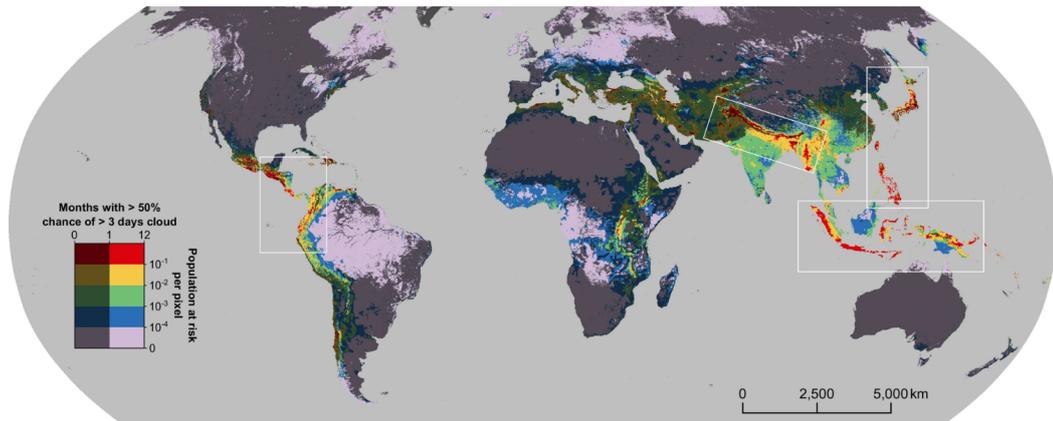
Figure 1.3: Population likely to be impacted by earthquakes (colour). Areas where satellite imagery is likely to obscured by cloud cover for at least 3 consecutive days for < 1 month in a year overlain in grey and areas > 1 month left bright. (Reproduced from from Robinson et al., 2019, under creative commons licence © 2019, Springer Nature)

a significant problem for rainfall triggered landslides. For example it is generally not possible to map landslides triggered by the monsoon in Nepal, which lasts for several months, until the end of the monsoon (Dahlquist and West, 2019; Marc et al., 2019).

For emergency response, cloud cover can significantly disrupt the process of generating landslide information, resulting in incomplete information being available during the early decision-making stages of the emergency response (The British Geological Survey, 2016; Williams et al., 2018). The M_w 7.8 2015 Gorkha, Nepal earthquake illustrated this problem. The earthquake triggered around 25,000 landslides across an area of hundreds of kilometres (Roback et al., 2018), and, although it occurred during Nepal's dry season, the disruption due to cloud cover was significant, with no landslide information available during the first 72 hours due to heavy cloud cover for the first seven days following the earthquake, and significant areas not imaged within two weeks. Robinson et al. (2019) demonstrated that this lack of cloud-free optical imagery would have been even more acute for an earthquake occurring in Nepal during the monsoon season, with some of the most mountainous areas of the country unlikely to be successfully imaged once between June and September. Figure 1.3 shows the coincidence of areas likely to be obscured by cloud and areas likely to be impacted by earthquakes, demonstrating that this is a severe problem across large areas of South-east Asia, northern South America and Central America, areas that are also disproportionately affected by landslides triggered by factors other than earthquakes (Petley, 2012). Therefore optical imagery is not a reliable source of landslide information for emergency response, as it is too dependent on weather conditions.
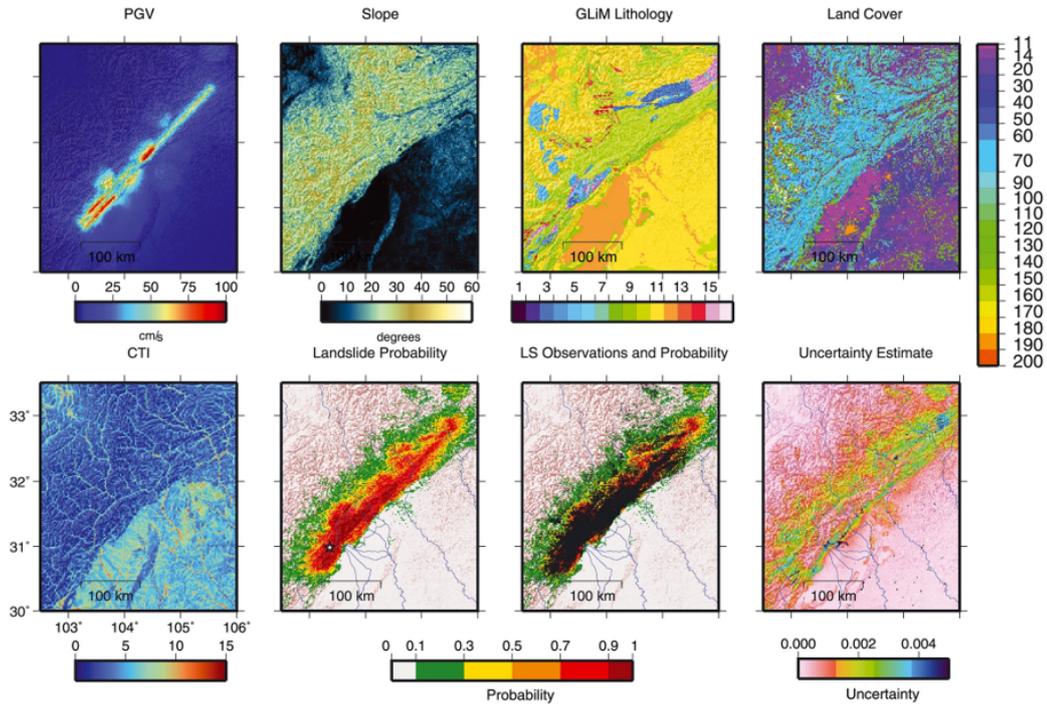
Figure 1.4: A global empirical model of the 2008 M$_\text{w}$ 7.9 Wenchuan Earthquake based on peak ground velocity (PGV), slope, lithology, land cover and compound topographic index (CTI) (reproduced from Nowicki Jessee et al., 2018, © 2018 American Geophysical Union)

1.2.2   Generation of landslide information with empirical models

In the absence of optical satellite imagery, empirical models can be used to estimate areas where landslides are likely to have occurred based on predisposing factors such as slope and lithology, and some measurement or estimate of the triggering mechanism, such as earthquake shaking data (e.g. Kritikos et al., 2015; Nowicki Jessee et al., 2018; Robinson et al., 2017) or rainfall data (e.g. Kirschbaum and Stanley, 2018). An example of such a model and the input datasets used to produce it is shown in Figure 1.4.

Predictions from these models can be made available within hours of an earthquake or rainfall event anywhere on Earth, which is a major advantage in emergency response. Generally they are generated at a relatively low resolution (e.g. 1 km^2 in the case of Kirschbaum and Stanley (2018) and Nowicki Jessee et al. (2018)) and can be combined with maps of road networks and rivers, to identify where these are likely to have been blocked (Robinson et al., 2018).

These models are thus an invaluable tool in emergency response. However, in some situations, they do not perform well. For example in the case of the 2018 Hokkaido earthquake, the extent of the triggered landslides is thought to be the result both
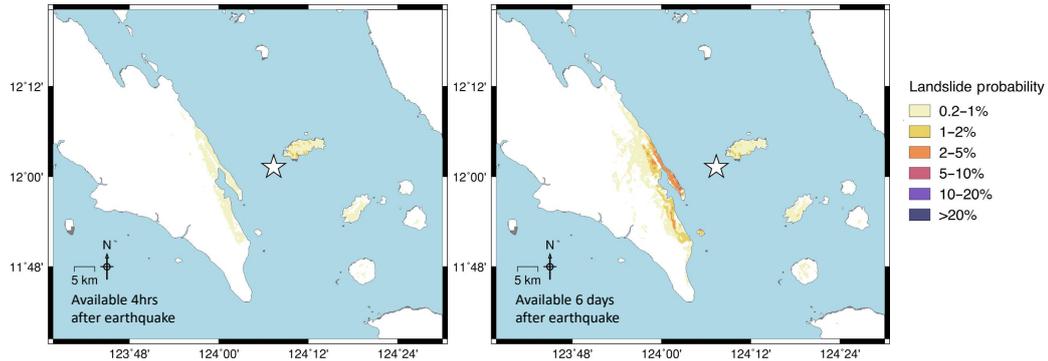
Figure 1.5: Two versions of the USGS ground failure product for an M_w 6.6 earthquake that occurred on 18 August 2020 in the Phillippines downloaded 4 hours and 6 days after the earthquake (Nowicki Jessee et al., 2018, downloaded from `https://earthquake.usgs.gov/earthquakes`). White star shows earthquake epicentre.

of the earthquake, and heavy rainfall in the month before the earthquake (Zhang et al., 2019), and none of these models incorporate both rainfall and earthquake data. For landslides triggered by the 2018 $M_w > 6.0$ 2018 earthquake sequence in Lombok, Indonesia, it was noted that the extent of the landslides triggered late in the sequence was underestimated by the United States Geological Survey (USGS) ground failure model of Nowicki Jessee et al. (2018), which may indicate that these models do not perform well for complex sequences of earthquakes (Ferrario, 2019).

Another problem that has been observed when applying these models to earthquake-triggered landslides, is that the USGS ShakeMap estimates for an earthquake evolve following the earthquake as more more data, for example ground deformation measurements from satellite radar, become available and the earthquake source model is updated accordingly. The version of the shaking data used can have a significant effect on the quality of the landslide prediction, with models available immediately following the earthquake performing worse than those generated using later versions of the ShakeMap input (Allstadt et al., 2018; Thompson et al., 2020). As an example of this, Figure 1.5 shows two versions of the USGS ground failure product available 4 hours and 6 days after a recent M_w 6.6 earthquake that occurred on 18 August 2020 in the Phillippines. In the case of rainfall-triggered landslide models such as that of Kirschbaum and Stanley (2018), the performance of the model is strongly dependent on the rainfall dataset used, as well as the landslide type and rainfall intensity (Jia et al., 2020; Kirschbaum and Stanley, 2018).

The fundamental limitation to using empirical models of landslide susceptibility is that no data are supplied to the model containing direct observations of the landslides. This hampers model performance for complicated events, and limits

them to producing a single prediction of a landslide event that may in reality evolve through time, or be influenced by previous earthquakes or rainfall.

1.2.3 Generation of landslide information from SAR data

For landslide detection, synthetic aperture radar (SAR) imagery has a significant advantage over optical satellite imagery, as data can be acquired through cloud, and so are more reliably available following an earthquake. Recently, the number of satellites collecting SAR data has greatly increased. The European Space Agency (ESA) Sentinel-1 constellation acquires SAR imagery continually and globally on two tracks with a 12-day repeat time (6 in Europe), providing open access SAR data regularly across the world. The planned NiSAR constellation, a joint project from NASA and the Indian Space Research Organisation (ISRO) due to launch in 2022, will have a similar acquisition strategy (Sharma, 2019). Between the Sentinel-1 satellite constellation, and other constellations whose acquisitions are targeted at earthquake disaster response such as the Japanese Space Agency (JAXA)'s Advanced Land Observing Satellite 2 (ALOS-2) constellation, SAR imagery is now available within days of an earthquake anywhere on Earth.

Techniques such as differential Interferometric SAR (InSAR), in which ground deformation measurements are obtained from pairs of SAR images (See Chapter 2 for more detail) or persistant scatterer InSAR, in which the movement of stable reflectors is tracked through a time series of SAR images, have been widely applied to slow-moving landslides (Bekaert et al., 2020; Bonì et al., 2018; Hu et al., 2019; Mulas et al., 2016; Rosi et al., 2018; Shi et al., 2020; Solari et al., 2020). InSAR has been used to identify locations where the ground is moving in landslide-prone regions (e.g. Shi et al., 2020), to update inventories of slow-moving landslides and assess whether they are active (e.g. Bonì et al., 2018; Rosi et al., 2018) and to monitor individual, large, slow-moving landslides (e.g. Hu et al., 2019; Mulas et al., 2016). Such studies are invaluable in assessing the risk associated with slow-moving landslides. However, they cannot be applied in the case of a landslide that moves more than a few cm between SAR acquisitions and so are unsuitable for use in rapid landslide detection.

Recently, work has begun to develop methods of applying SAR data to the automatic detection of earthquake-triggered landslides. These methods could allow generation of landslide information within days of an earthquake. Landslides alter the scattering properties of the Earth's surface, resulting in a change in the amplitude and coherence (signal-to-noise ratio) of SAR imagery. In the aftermath the 2015 Gorkha earthquake, using an SAR-coherence-based algorithm designed

to detect building damage associated with an earthquake, Yun et al. (2015) also found they were able to detect the Langtang Valley landslide, an exceptionally large landslide triggered during the earthquake. Since then, various landslide-detection methods have been proposed based on SAR amplitude (e.g. Mondini et al., 2019; Konishi and Suga, 2018, 2019), coherence (Olen and Bookhagen, 2018; Yun et al., 2015), or on a combination of these (e.g. Aimaiti et al., 2019; Ge et al., 2019; Jung and Yun, 2019).

SAR data are routinely used in other rapid response situations, for example in flood mapping or in the production of interferograms to map ground deformation after an earthquake or during an episode of volcanic unrest (Funning et al., 2005; Martinis et al., 2015; Meyer et al., 2015; NASA, 2018). NASA's ARIA project uses SAR to produce damage proxy maps in urban areas following earthquakes, cyclones or wildfires. These applications demonstrate that SAR products can be generated and used for emergency response. SAR methods show considerable promise in landslide detection for emergency response, however as work on their reliability is still being carried out, SAR is not yet widely used to generate information on rapid landslides.

1.3 Thesis Overview

In this thesis, I will focus on developing SAR coherence methods for earthquake-triggered landslide detection, focussing on emergency response applications. Although some work has been carried out in this area, there are several unanswered questions, which I will attempt to answer in this work.

First, the majority of studies that use SAR coherence for landslide detection rely on the decrease in coherence through time caused by a landslide (e.g. Aimaiti et al., 2019; Jung and Yun, 2019; Yun et al., 2015). This method was originally developed for use in building damage detection (Fielding et al., 2005; Yun et al., 2015), raising the question of whether this could be improved on in the case of landslides. I address this in Chapter 3, where I present a method specifically designed for landslide detection and demonstrate that this outperforms existing methods when using Sentinel-1 SAR data of the M_w 7.8 2015 Gorkha earthquake. In Chapter 4, I also present some simpler methods which use additional post-event SAR imagery and can also offer an improvement in landslide detection.

Second, although several studies have been published using SAR methods for landslide detection, all of them use only data from a single SAR sensor to predict a single trigger event. Therefore, there is currently little understanding of how easily

methods can be transferred between events, and whether there is an advantage to using different methods when different SAR data are available. In Chapter 4, I test the performance of five different SAR coherence methods using imagery from two SAR systems of four case study events.

Finally, both the empirical models described in Section 1.2.2 and SAR methods of landslide detection represent an alternative to optical satellite imagery that allow information on landslides to be generated rapidly following an earthquake. Therefore, it would be useful to know which of these options is better, or whether it is better to combine these products by using SAR data acquired after an earthquake as an additional input alongside static predictors of landslide likelihood such as topographic slope and lithology. In Chapter 5, I use Random Forest regression to model landslide areal density, and demonstrate that using SAR data as an additional input offers improved landslide detection ability over the original empirical model and SAR methods individually.

The thesis is therefore structured as follows. In Chapter 2, I provide an introduction to SAR and particularly SAR coherence. I also give details on the data and processing steps used to generate the results presented in the chapters that follow. In Chapter 3, I present a new method of landslide detection using SAR coherence using the M_w 7.8 2015 Gorkha, Nepal earthquake as a case study. In Chapter 4, I present the results of a systematic investigation into the application of SAR coherence methods to four case study event using different SAR datasets. In Chapter 5, I integrate SAR coherence methods with empirical predictors of landslide likelihood such as slope steepness and ground shaking using Random Forests. The locations of the case studies used in Chapters 3, 4 and 5 are shown in Figure 1.6. Finally in Chapter 6, I discuss the results of the thesis in a wider context, considering planned SAR satellite constellations and suggesting possible further applications of the results presented in this thesis.
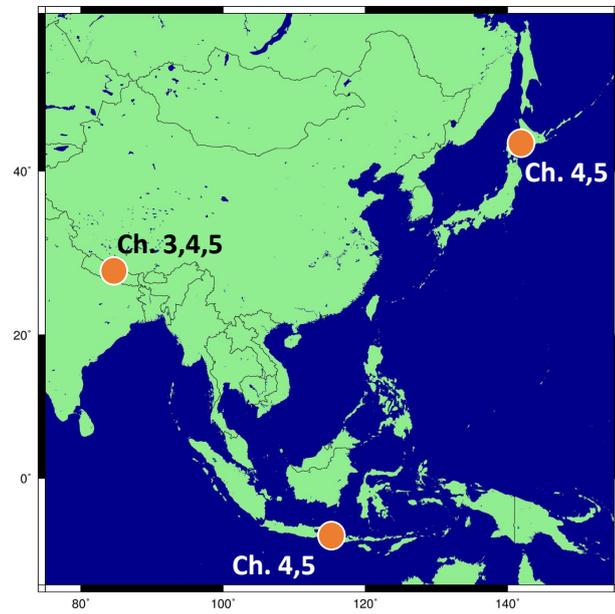
Figure 1.6: Case study locations (orange circles) labelled with the chapters (Ch) of this thesis that they feature in.

Methods

While the acquisition of SAR imagery through cloud gives it an advantage over optical satellite imagery, it is also considerably more complicated to process and interpret than optical satellite imagery. In this chapter, I provide a brief overview of the theory behind SAR, and the data and processing steps I used to obtain the results shown in Chapters 3, 4 and 5. For a more detailed description of SAR theory see Hanssen (2001). I conclude this chapter with details on how SAR coherence can be interpreted, particularly with respect to landslides, followed by a short review of applications of SAR methods to rapid landslide detection.

2.1   Theory

A SAR satellite system actively illuminates the Earth's surface with a pulse of microwave radiation and records the backscattered coherent signal as complex data describing its amplitude and phase ϕ (Figure 2.1; Hanssen, 2001). The 'synthetic aperture' refers to the artificial increasing of the aperture window size, which allows the azimuthal resolution of the acquired data to be increased without the satellite having to carry a larger sensor (described in Chen et al., 2000).

Any changes to the range R_0 between the ground and satellite will result in a change in ϕ. Thus the phase change between two SAR images $\Delta\phi$ can be used to measure the change in range ΔR. In the case where the microwave pulse is emitted and recorded by the same sensor, this relationship is described by Equation 2.1, where λ is the microwave wavelength (Chen et al., 2000).

$$\Delta\phi = \frac{4\pi\Delta R}{\lambda} \tag{2.1}$$
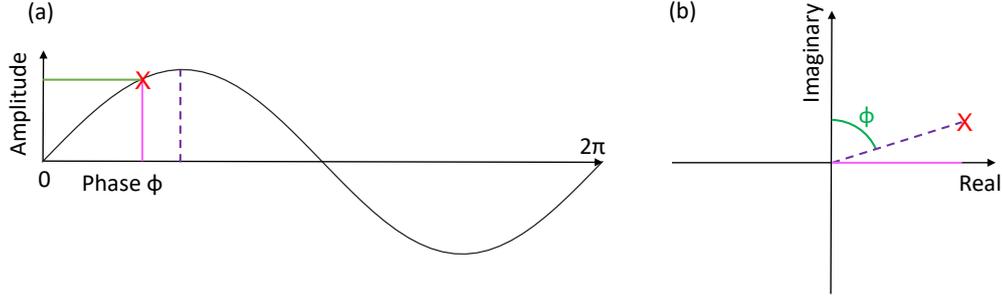
Figure 2.1: Visualising the amplitude and phase of a wave in (a) phase, amplitude space and (b) real, imaginary space. In (a) and (b), an example signal is shown in red, its amplitude in purple and phase in green, with the real component of the wave shown in pink.

The measured $\Delta\phi$ is obtained from the complex multiplication of two SAR images, one of which has been resampled onto the geometry of the other. The complex representations of two SAR images A and B are given by equations 2.2 and 2.3 (Hanssen, 2001), where $j = \sqrt{-1}$, and $|A|$ is the absolute value of A.

$$A = |A|e^{j\phi_A} \tag{2.2}$$

$$B = |B|e^{j\phi_B} \tag{2.3}$$

An interferogram C can then be formed from the complex multiplication of A and B according to Equation 2.4, where the overline indicates the complex conjugate (Hanssen, 2001).

$$C = A\overline{B} = |A||B|e^{j(\phi_A - \phi_B)} \tag{2.4}$$

From this, $\Delta\phi = \phi_A - \phi_B$ can be extracted and used to obtain ΔR.

$\Delta\phi$ can be influenced by several factors, and so can be broken down into different components (Equation 2.5; Hoen and Zebker, 2000).

$$\Delta\phi = \Delta\phi_{topography} + \Delta\phi_{deformation} + \Delta\phi_{orbit} + \Delta\phi_{atmospheric} + \Delta\phi_{noise} \tag{2.5}$$

The first three of these are a direct result of ΔR according to Equation 2.1. ΔR can be the result of either ground deformation (Figure 2.2a), orbital difference or due to topographic effects in the case when the perpendicular baseline (the distance between the acquisition locations of the two satellites defined perpendicular
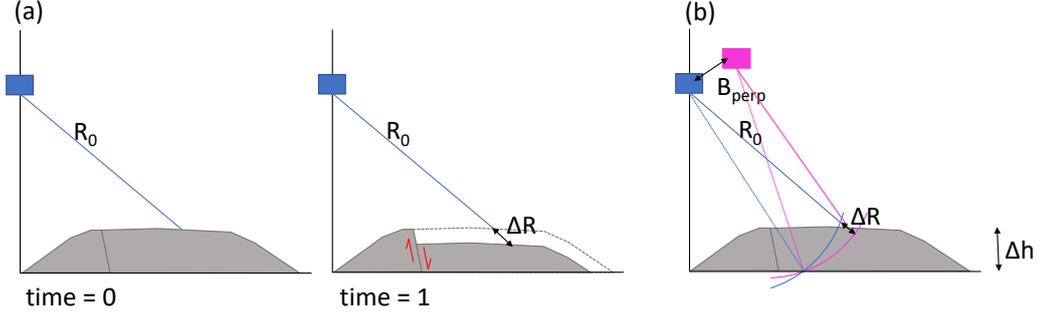
Figure 2.2: (a) Differential Interferometric SAR. Difference in Range ΔR arising from ground surface deformation due to an earthquake. (b) Across-track SAR (based on Moreira et al., 2013). The difference in ΔR arising from a height change Δh across a landscape when a pixel is imaged twice from different locations separated by a perpendicular baseline B_{perp}.

to orbit direction) is non-zero (Figure 2.2b). $\Delta\phi_{atmospheric}$ arises from changes in atmospheric conditions in the troposphere and ionosphere between image acquisitions. Since these disturbances tend to occur on spatial scales much larger than the scale at which coherence is estimated, they are of little concern here, but are important when InSAR is used in ground deformation studies. Sources of $\Delta\phi_{noise}$ are covered in detail in Section 2.4, as this contribution to phase change can arise from, among many other things, landslides and so is the focus of this study.

If two SAR images are acquired with the same geometry at different times, then $\Delta\phi_{topography} = \Delta\phi_{orbital} = 0$, and after correcting for $\Delta\phi_{atmospheric}$, $\Delta\phi_{deformation}$ can be used to map ground surface movements in the line of sight direction (Rosen et al., 2000; Hanssen, 2001). This technique is known as differential InSAR, and the SAR data and processing methods I use in this thesis were intended for this InSAR technique. In reality, this identical acquisition geometry cannot be achieved and so it is necessary to correct for $\Delta\phi_{topography}$ and $\Delta\phi_{orbital}$. Alternatively, two SAR images acquired at different geometries at the same time can be used to generate a digital elevation model (DEM) in a process known as across-track interferometry (e.g. Farr et al., 2007; Zink et al., 2008). As the two images are acquired simultaneously, $\Delta\phi_{deformation} = 0$ and any phase delay due to atmospheric effects is approximately the same for both images, so that $\Delta\phi_{atmosphere} \sim 0$. The sensitivity of $\Delta\phi_{topography}$ to height Δh is determined by the range R_0, local incidence angle θ_i, and the perpendicular baseline B_{perp} (Equation 2.6; Moreira et al., 2013).

$$\Delta\phi = \frac{4\pi B_{perp}}{\lambda R_0 sin\theta_i}\Delta h \tag{2.6}$$

2.1.1 Pixel resolution and spacing

The spatial resolution of SAR data defines the smallest object that can be identified in the imagery. This is directly relevant to the applicability of SAR data to landslide detection as it determines the lower limit on the detectable landslide size. It is important to note that the resolution of the SAR data (the area in Range × azimuth space contributing to each pixel) and the pixel spacing, are not the same. For example, Sentinel-1 Single-look complex (SLC) data acquired in interferometric wide swath mode have a resolution (Range × Azimuth coordinates) of 2.7-3.5 × 22 m and a pixel spacing of 2.3 × 14.1 m. The resolution of the final product may be different again due to multi-looking and reprojection to geographic coordinates.
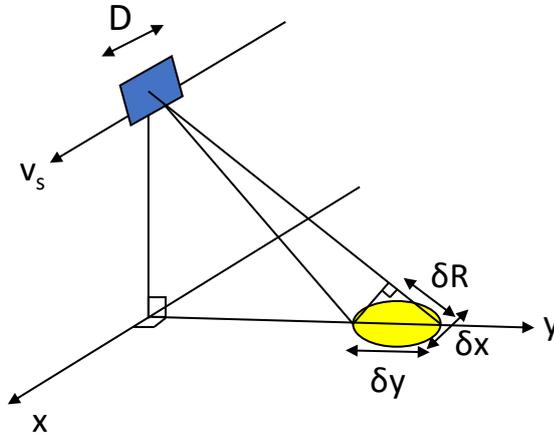
Figure 2.3: Resolution of a target pixel imaged by a satellite radar sensor in x (azimuth), y (ground range), and R (slant range) directions.

In a real aperture radar system, the resolution in the azimuthal direction δx is dependent on the aperture length D, the slant range R_0 and the microwave wavelength λ according to Equation 2.7 (Figure 2.3).

$$\delta x = \frac{R_0 \lambda}{D} \tag{2.7}$$

According to Equation 2.7, the aperture size D places a limitation on δx. D is in turn limited by the maximum sensor size that can feasibly be carried by a satellite. The azimuthal resolution of a real aperture radar image is thus extremely coarse. To overcome this, the synthetic aperture technique was developed, in which a larger aperture is simulated through the movement of the satellite. The azimuthal resolution becomes dependent on the Doppler bandwidth $B_{Doppler}$ and the relative

velocity of the satellite v_s (Hanssen, 2001).

$$\delta x = \frac{v_s}{B_{Doppler}} \tag{2.8}$$

The resolution in the range direction δR is dependent on the pulse duration T_p according to Equation 2.9, where c is the speed of light.

$$\delta R = \frac{cT_p}{2} \tag{2.9}$$

This limits δR, since enough energy must be transmitted in each pulse to obtain a usable returned signal, placing a lower limit on T_p. In order to reduce T_p beyond what would be physically possible, the microwave energy used to generate the SAR image is emitted as a chirp of bandwidth B_{ch}. After processing, the effective pulse duration is equal to $1/B_{ch}$, thus, δR is defined according to Equation 2.10 (Hanssen, 2001).

$$\delta R = \frac{c}{2B_{ch}} \tag{2.10}$$

The amplitude and phase of every pixel is recorded as a single complex value. However, the resolution cell of each pixel may include multiple scatterers, which together contribute to the overall recorded amplitude and phase of the pixel (Figure 2.4; Moreira et al., 2013). The recorded signal of each cell (represented by the red
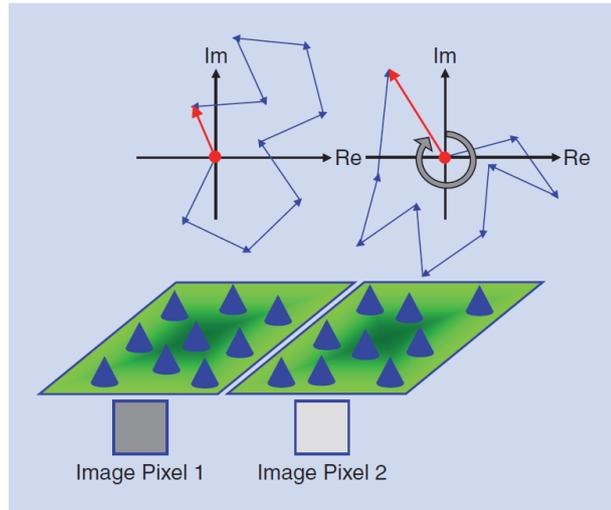
Figure 2.4: The distribution of scatterers within two neighbouring pixels, and their contribution to the signal of each pixel as a whole (reproduced from Moreira et al., 2013, © 2013 IEEE).

arrows in Figure 2.4) is equal to the coherent sum of the scattering signals from every scatterer within the resolution cell (represented by the blue arrows). This includes a depth component not visible in Figures 2.3 and 2.4: the microwave energy may penetrate beyond the upper surface and interact with scatterers at different depths. For example, in a forest, the recorded signal may include components from leaves, branches, tree trunks and the ground beneath (Freeman and Durden, 1998). In dry soil, microwaves may penetrate to depths of up to around 50 cm, although this depth decays rapidly as soil moisture content increases and SAR wavelength decreases (Nolan and Fatland, 2003). Neighbouring pixels can have different signals due to the distribution of scatterers within them (Figure 2.4), resulting in a form of radar image noise known as 'speckle', which can only be removed by a spatial averaging step in SAR data processing known as 'multi-looking' at a cost to the resolution of the final product. A single scatterer with a high amplitude signal can dominate the overall signal of the resolution cell, even if it does not make up the dominant material within the cell. Both of these phenomena must be borne in mind when interpreting SAR data.

2.1.2 Acquisition Geometry

SAR data are acquired obliquely along approximately polar orbits. Data are acquired on 'ascending' tracks, in which the satellite moves from south to north and 'descending', in which the satellite moves from north to south (Figure 2.5). The satellite 'look direction', i.e. the direction in which it transmits and records microwave energy, is perpendicular to the satellite trajectory (Figure 2.3). This side-looking geometry removes a critical ambiguity when converting range measurements to geographic locations (Hanssen, 2001). In most systems, the ascending and descending tracks image the ground surface from different directions (e.g. if both are 'right looking', ascending imagery is acquired looking east and descending, west), which is useful for several reasons. The phase change between two images is sensitive to ground deformation in the line of sight direction (Figure 2.2). By using interferograms acquired from two different directions, the 3D ground deformation can be estimated (Wright et al., 2004), which is extremely useful for measuring ground subsidence and motion along faults (e.g. Chaussard et al., 2013; Hussain et al., 2016) and in inferring earthquake source parameters (e.g. Funning et al., 2005; Shan et al., 2004).

A second reason that the acquisition of SAR data from two look directions is useful, is that in mountainous areas, certain slopes are not always well imaged by a single track. The slant range resolution δR (Equation 2.10) can be projected into a ground
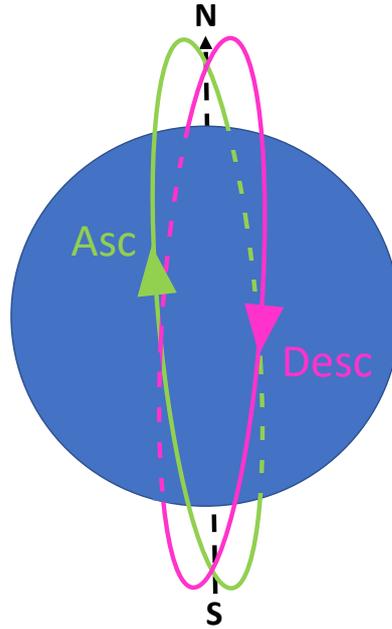
Figure 2.5: Diagram of ascending and descending SAR orbit directions

range resolution δy, which is dependent on the local incidence angle θ_i according to Equation 2.11 (Chen et al., 2000).

$$\delta y = \frac{\delta R}{sin\theta_i} = \frac{c}{2B_{ch}sin\theta_i} \tag{2.11}$$

This dependence of Δy on θ_i results in distortion in the range direction for sloping surfaces, where areas of ground are compressed (foreshortened) on slopes facing towards the sensor and stretched on slopes facing away from the sensor. In severe cases, this can lead to effects such as layover, where two geographic locations correspond to a single location in radar geometry, or shadow, in which no microwave energy reaches part of a slope facing away from the sensor (Rosen et al., 2000; Hanssen, 2001). In most cases, slopes that are poorly oriented on the descending track are more favourably oriented on the ascending track and vice versa, so that with both tracks together, coverage over mountainous areas is improved. This is particularly advantageous to the application of SAR to landslide detection, as landslides are likely to occur in areas of steep topography, where the problems associated with poorly oriented slopes are most acute.

2.1.3 Polarisation

The polarisation of the SAR data affects the interaction between the radar wave and the ground surface. The polarisation of SAR data is described as the polarisation

of the transmitted and received wave, for example 'HV' data are transmitted with horizontal polarisation and recorded in the vertical. Some SAR sensors, for example ALOS-2, acquire "quad-pol" SAR data in which data are both transmitted and received in horizontal (H) and vertical (V) polarisations, resulting in HH, HV, VH, and VV. This allows a full scattering matrix to be constructed, which can more completely describe the scattering properties of the Earth's surface and so contains more information on the physical properties of the ground surface (Cloude and Pottier, 1996; Freeman and Durden, 1998; Yamaguchi et al., 2005).

Quad-pol SAR data are therefore extremely useful in land classification (Cloude and Pottier, 1997) and several studies have demonstrated that quad-pol data can be used to map landslides (e.g. Czuchlewski et al., 2003; Masato et al., 2020; Park and Lee, 2019; Yamaguchi et al., 2019). For example, Yamaguchi et al. (2019) used quad-pol ALOS-2 data to detect landslides following the 2018 Hokkaido, Japan earthquake. Quad-pol SAR can be decomposed into surface scattering, volume scattering, double-bounce scattering and helix scattering (Yamaguchi et al., 2005). Volume scattering is associated with vegetation, thus the removal of vegetation by a landslide decreases the power of this component when the signal is decomposed and this change is used by Yamaguchi et al. (2019) to identify landslides. Polarimetric methods such as this work well, but not all satellites acquire quad-pol data and those that do, often do not acquire these data following an earthquake, as they are not required for InSAR measurements of ground deformation. These data are therefore not likely to be available during the initial phases of the emergency response for most earthquakes. Therefore in this thesis, I used only "single-pol" SAR data (HH or VV). This results in a less comprehensive record of the scattering properties, but it ensures that the results are widely applicable for future events, and reduces the volume of data which needs to be downloaded, stored and processed.

2.2 SAR Constellations and Datasets

Figure 2.6 shows satellite systems collecting SAR data between 1992 and 2023 (including planned constellations), which are operated by a large number of national and international space agencies. Here, I use data from the ESA constellation Sentinel-1a and 1b, and from the Phased-Array L-band Synthetic Aperture Radar 2 (PALSAR-2) sensor aboard the JAXA ALOS-2 satellite constellation. Throughout the thesis, SAR tracks will be named according to their sensor, track number and orbit direction. For example in Chapter 3, I use data acquired by Sentinel-1 on track number 19 in a descending orbit, referred to as track S019d.
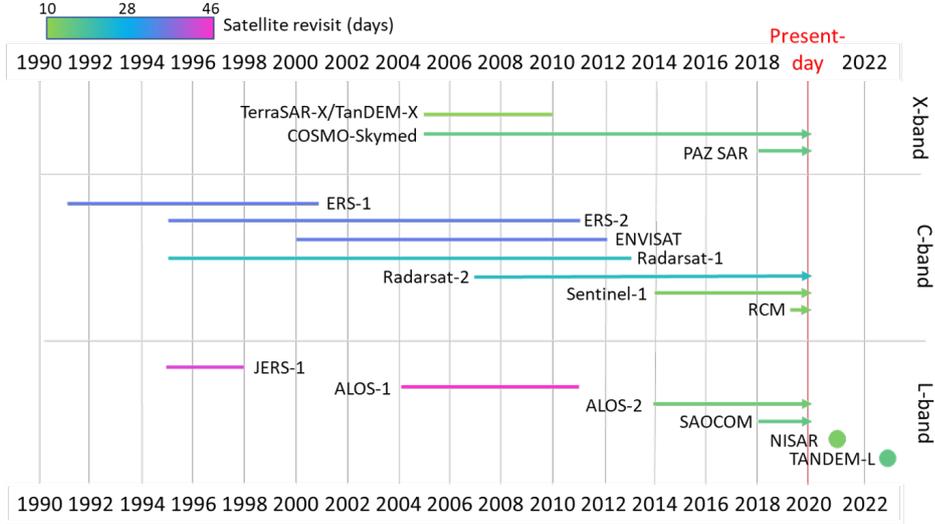
Figure 2.6: SAR missions in operation between 1990 and 2023. Horizontal lines show the lifetimes of past satellites, arrows show currently satellites currently in operation and circles mark the planned launch dates of future missions. Symbols are coloured according to satellite revisit time. (based on UNAVCO (2019) with additional information from Meyer (2019))

The satellite constellations in Figure 2.6 are organised according to their wavelength λ. SAR data may be acquired at Ka ($\lambda = 0.75 - 1.2$ cm), Ku ($\lambda = 1.7 - 2.5$ cm), X ($\lambda = 2.5 - 4$ cm), C ($\lambda = 4 - 8$ cm), S ($\lambda = 8 - 15$ cm), L ($\lambda = 15 - 30$ cm) and P ($\lambda = 60 - 120$ cm) bands (Moreira et al., 2013). The wavelength affects the interaction between the radar energy and the ground, and there are advantages and disadvantages to each which make them suitable for different applications. From Equation 2.1, a sensor operating at a shorter wavelength requires a lesser ΔR to obtain the same $\Delta\phi$. Shorter wavelengths are therefore more sensitive to small deformations to the ground surface. The same is true for across-track SAR, where a smaller Δh is required to obtain the same $\Delta\phi$ at shorter wavelengths (Equation 2.6). Short wavelength SAR data are therefore extremely beneficial for high resolution studies (e.g. Reale et al., 2011; Zink et al., 2008). Unfortunately, the high resolution of short-wavelength SAR systems often comes at a cost to coherence, primarily due to increased sensitivity to smaller random movements of scatterers (Section 2.4). This is particularly problematic in heavily vegetated regions, and so in such locations, longer wavelength SAR is usually necessary to obtain usable ground deformation measurements (e.g. Fujiwara et al., 2019). The bands shown on Figure 2.6 are the most common for satellite SAR systems: C-band, X-band and L-band. In this study, I use C-band Sentinel-1 ($\lambda \sim 5.5$ cm) and L-band ALOS-2 ($\lambda \sim 24$ cm) data, as X-band is less suitable for coherence studies vegetated regions and therefore is unlikely to work for the case studies I use in this thesis.

As well as the wavelength, there are several other acquisition parameters that vary between SAR datasets that impact their applicability to landslide studies. One obvious parameter is the spatial resolution of the acquired data, which determines the smallest landslide that is likely to be detectable in the data. Another is the Swath width, which describes the coverage in the range direction. Adjacent scenes in the azimuth direction can be merged, but as scenes adjacent in the range direction are acquired at different times and with differing viewing geometries, they have to be processed as separate tracks. To map landslides triggered over a large area, a wide swath width is advantageous as it allows all the landslide information to be extracted from data acquired at the same time and under the same conditions. Often satellite systems are capable of acquiring data in different modes, with a trade-off between swath width and spatial resolution. For example, the ALOS-2 satellite can acquire SAR data at a spatial resolution of 3 × 1 m with a swath width of 25 km up to a resolution of 60 m with a swath width of 490 km (JAXA, 2020). Smaller landslides could be detected at the first extreme, but a much larger area could be covered with the second. In this study, I use Sentinel-1 data with a spatial resolution of 2.7-3.5 × 22 m and a swath width of 250 km, and ALOS-2 data acquired at a spatial resolution of 3-10 m and swath width 30-70 km.

2.3   SAR Data Processing

SAR data requires more complex processing than optical satellite imagery before they can be used in landslide detection. I used the GAMMA SAR processing software package to process the the SAR data used in this study. For Sentinel-1, I used the LiCSAR processing software, which uses GAMMA tools to process SAR data (Lazeckỳ et al., 2020). Processing SAR data also requires a DEM, for which I used the 1-arc-second Shuttle Radar Topography Mission (SRTM) DEM of Farr et al. (2007).

The Sentinel-1 data I used in this study was acquired in 'Interferometric Wide' mode, and so every track is made up of three subswaths, which are in turn made up of a series of "bursts". Each burst can be considered as a separate SLC image. As the bursts overlap, and are acquired within a very short timeframe (within 10s of seconds), the bursts which cover the desired area can be stitched together into a complete SLC image. LiCSAR does this automatically (Lazeckỳ et al., 2020). For the ALOS-2 data used here, this processing step was not necessary, and from here on, unless otherwise stated, the processing steps are the same for both ALOS-2 and Sentinel-1 data.

The SAR methods I use in this thesis require a time series of SAR images spanning the earthquake. One of these is selected as the 'primary' image, against which all other images are referenced. The first step in processing is to multi-look this image. Multi-looking is a spatial averaging step which increases the signal strength at the expense of the spatial resolution. In particular, the aim of multi-looking is to reduce noise due to 'speckle', an effect of many scatterers of varying characteristics within a resolution cell being recorded as a single pixel (Figure 2.4; Moreira et al., 2013). As my purpose in this study was to detect landslides, the extent of the multi-looking was fairly limited in order to preserve the spatial resolution. For Sentinel-1, I multi-looked the Sentinel-1 data used in this study by five in range and one in azimuth, and the ALOS-2 data by 5 in both range and azimuth. The geometry of this primary Multi-looked Intensity (MLI) raster is then used as the reference geometry throughout the processing.

The next step is to generate a look-up table, which describes how the 2D image in the radar coordinate system reprojects to the geographic coordinate system. This is a two step process. An initial lookup table is calculated from the primary MLI and the DEM. This is then used to simulate an MLI, and the offset between this and the real MLI are used to refine the lookup table and improve its accuracy. This look-up table can then be used to convert any data in radar coordinates, for example, an interferogram, coherence map or MLI amplitude map, into geographic coordinates, or vice versa e.g. to generate a DEM in the radar coordinate system, which is necessary for SAR processing.

The next step is geometric coregistration. All SAR images used in any joint analysis must have the same geometry as the primary MLI. Therefore the remaining 'secondary' SLCs are resampled onto the geometry of the primary SLC. For every secondary SLC, initial offset estimates between the primary and secondary SLC are calculated based on orbit information and the DEM and are used to generate an initial co-registered secondary SLC. The offsets are then re-estimated based on cross correlation between the primary SLC and the initial co-registered secondary SLC, and a final co-registered secondary SLC is generated based on these estimates (Lazeckỳ et al., 2020). In the case of Sentinel-1 data, a further coregistration refinement step is carried out based on spectral diversity (Wegnüller et al., 2016). The co-registered secondary SLCs are then multi-looked in the same way as the primary SLC.

From any pair of these multi-looked SLCs, which now all have the same geometry, an interferogram can then be calculated as the difference in phase between the two images. However, there are other effects which need to be accounted for before this can be used to map ground deformation. From Equation 2.5, $\Delta\phi$ is dependent on

both ground deformation and, in the case of non-zero perpendicular baseline, on topography (Equation 2.1). Although ideally every image pair would be acquired at different times from exactly the same position resulting in $\Delta\phi_{topography} = 0$ and $\Delta\phi_{orbit} = 0$, in reality this is impossible to achieve. To correct for this, $\Delta\phi_{topography}$ is estimated based on the DEM and B_{perp} and removed. The flat Earth phase trend is also calculated from the perpendicular and parallel baselines and removed from the interferogram. This leaves $\Delta\phi_{deformation}$, $\Delta\phi_{noise}$, and $\Delta\phi_{atmospheric}$ from Equation 2.5.

For the purpose of ground deformation studies, the next steps would be to identify noisy areas of the interferogram by estimating the coherence, then to estimate and remove $\Delta\phi_{atmospheric}$, and finally to 'unwrap' the phase, producing ground deformation measurements from the cyclic measurement of $\Delta\phi$. However, as the aim of this thesis was not to map ground deformation, but to detect landslides, which appear as noise in the interferogram, there was no need to progress beyond the generation of the coherence map.

2.4   SAR Coherence

For the interferogram C (formed in Section 2.1 from two SAR images A and B) to be usable in mapping ground deformation, the complex signals recorded for each cell in images A and B must be coherent. The true complex coherence γ_{true} is described by Equation 2.12 (Hanssen, 2001)

$$\gamma_{true} = \frac{E\{A\overline{B}\}}{\sqrt{E\{|A|^2\}E\{|B|^2\}}} \tag{2.12}$$

The Expectation value $E\{\}$ of every pixel can only be calculated from multiple data at each pixel, and the SAR system records only one complex value at each pixel. Therefore, in practise, it is not possible to calculate γ_{true}. Instead, Equation 2.13 is used to estimate the magnitude of the coherence of every pixel, based on a small ensemble of n pixels (Hanssen, 2001).

$$|\gamma| = \frac{\frac{1}{n}\sum_{i=1}^{n} A_i\overline{B_i}}{\sqrt{\frac{1}{n}(\sum_{i=1}^{n}|A_i|^2\sum_{i=1}^{n}|B_i|^2)}} \tag{2.13}$$

The factor of $\frac{1}{n}$ is not included in all representations of this equation in the literature, but is useful in the case where pixel ensembles of different sizes are used in coherence estimation, for example in the method of Spaans and Hooper (2016), which I use in Chapter 3. The result of both Equations 2.12 and 2.13 is a value

for every pixel in the interferogram between 0 and 1, where 0 represents complete decorrelation of a pixel between images *A* and *B*, and where 1 represents perfect correlation. If the pixels within the ensemble used in Equation 2.13 are similar in terms of amplitude and phase change, they will have a high coherence. The ensemble of pixels is chosen from a sufficiently small area that $\Delta\phi_{deformation}$ and $\Delta\phi_{atmospheric}$ are not expected to vary between pixels, and any loss of $|\gamma|$ is a result of $\Delta\phi_{noise}$.

In Chapter 3, I present a new method of landslide detection based on different coherence estimates, and so different methods of selecting the ensemble of pixels used in Equation 2.13 are discussed in detail in that chapter. In general, pixels are used that are expected to exhibit similar behaviour, either because they are spatially adjacent, in the case of the commonly used 'boxcar' coherence method (used by e.g. Hanssen, 2001; Hoen and Zebker, 2000; Lazeckỳ et al., 2020), or because they exhibit similar behaviour (e.g. Deledalle et al., 2014; Spaans and Hooper, 2016). Many factors can affect coherence and, to aid understanding, it is often decomposed into three multiplicative components: the temporal coherence $\gamma_{temporal}$, the spatial coherence $\gamma_{spatial}$ (sometimes designated 'geometric coherence') and the thermal coherence $\gamma_{thermal}$ (Equation 2.14; Zebker and Villasenor, 1992).

$$\gamma_{total} = \gamma_{temporal} \cdot \gamma_{spatial} \cdot \gamma_{thermal} \qquad (2.14)$$

$\gamma_{spatial}$ is the result of changes in imaging geometry between the acquisition of the first and second SAR image used to generate the interferogram. As described by Equation 2.6, measurable changes in phase can result from differences in topography when B_{perp} is non-zero. However, when B_{perp} is sufficiently large, the baskscatter recorded from two pixels will become entirely decorrelated.

Zebker and Villasenor (1992) originally derived Equation 2.15 to describe $\gamma_{spatial}$, from which we see that decorrelation of $\gamma_{spatial}$ is insignificant when B_{perp} is small, but its dependence on θ_i means it will also be exacerbated by steep slopes, and therefore may be relevant when considering the application of $|\gamma|$ to landslide detection.

$$\gamma_{spatial} = 1 - \frac{2B_{perp}\delta R cos^2\theta_i}{\lambda R_0} \qquad (2.15)$$

Equation 2.15 describes $\gamma_{spatial}$ for microwave energy scattered from a planar surface. However, as described in Section 2.1.1, each resolution cell also has a volume component, whose importance depends on the extent of penetration of the microwave energy into the cell. Hoen and Zebker (2000) show that Equation 2.15

describes only the horizontal component of $\gamma_{spatial}$, and that further decorrelation may result from the vertical component within a cell that exhibits significant volume scattering. For this reason, a fourth coherence component, γ_{volume}, is sometimes either included in Equation 2.14 (e.g. Hanssen, 2001), or considered as a sub-component of $\gamma_{spatial}$ (e.g. Hoen and Zebker, 2000).

Decorrelation of $\gamma_{thermal}$ is a result of noise within the receiving antenna on the satellite. $\gamma_{thermal}$ can be defined in terms of the signal to noise ratio (SNR) of the receiving antenna (Equation 2.16; Zebker and Villasenor, 1992).

$$\gamma_{thermal} = \frac{1}{1 + SNR^{-1}} \qquad (2.16)$$

Temporal coherence is generally the cause of the largest changes in coherence over time. It is the result of the physical properties of the ground surface changing between the acquisition of the two SAR images. It is therefore strongly affected by the time between the acquisition of the two images used to form the interferogram, because the longer this delay, the more likely it is that scatterers will change in some way during this time. In this thesis, $\gamma_{temporal}$ is of the most interest, as landslides alter the ground surface and so can both decrease and increase $\gamma_{temporal}$ over different timescales. However, there are many other factors that also affect $\gamma_{temporal}$ and so are worth considering first.

Essentially, any change to the dielectric or physical properties of the ground surface between the acquisition of two SAR images that results in a change to the phase or amplitude can result in loss of $\gamma_{temporal}$. As described in Section 2.1, a pixel's signal may be made up of many independent scatterers, and so loss of coherence can arise from alterations to any of these, particularly alterations to bright scatterers within a pixel. Therefore, although without quad-pol SAR, we are not able to resolve the scattering mechanism, the coherence of single-pol SAR is still sensitive to changes to the scattering properties of the ground. For example, a pixel that is vegetated in one SAR image, but bare soil or rock in the other is likely to be severely decorrelated in the interferogram. Thus growth or removal of crops, deforestation, landslides and forest fires are all likely to result in a decrease of $\gamma_{temporal}$ (e.g. Antikidis et al., 1998; Blaes and Defourny, 2003; Takeuchi and Yamada, 2002; Yun et al., 2015). Changes to the orientation or location of scatterers, for example when trees are blown down in a storm (e.g. Fransson et al., 2010) or buildings collapse during an earthquake (e.g. Fielding et al., 2005; Yonezawa and Takeuchi, 2001; Yun et al., 2015), can also change the scattering mechanism and result in a decrease of $\gamma_{temporal}$. Snowfall and flooding can also dramatically alter the scattering properties of the ground and so lead to low coherence.

The dielectric properties of the ground control its permittivity, and in particular the penetration depth of the SAR. This is strongly affected by moisture content, as water has a very different permittivity to dry soil. SAR penetrates further into dry soil than wet, interacting more with deeper scatterers within the target pixel up to a depth of around 50 cm (Nolan and Fatland, 2003; Scott et al., 2017). Changes in soil moisture content therefore affect the relative amplitudes of different scatterers, altering their coherent sum and resulting in decreased coherence. The same is true for melting snow, as wet and dry snow have different dielectric properties (Guneriussen et al., 2001; Koskinen et al., 1997).

For certain landcover types, wind can cause significant decorrelation of $\gamma_{temporal}$. First, in vegetated regions, everything from the movement of leaves and twigs to a whole tree being blown down will result in some alteration to the scatterers making up the resolution cell, and so can result in decorrelation (Tanase et al., 2010). This is why in most cases, vegetated areas have a lower coherence than bare rock or soil. Second in areas covered by snow, wind can cause snow to drift, altering the morphology of the ground surface, and resulting in changes to ϕ. Wind also results in disturbance to the surface of water, making it rough and turbulent, which means that coherence of bodies of open water is generally low or close to 0 for images acquired at different times (Lu and Kwoun, 2008). Changes in the roughness of other materials, for example the ploughing of a field, can also result in decorrelation of $\gamma_{temporal}$ (Blaes and Defourny, 2003).

SAR wavelength can significantly affect the sensitivity of $\gamma_{temporal}$, particularly for vegetated areas. The sensitivity of shorter wavelength SAR to smaller movements and smaller scatterers makes it more susceptible to decorrelation in vegetated regions. Zebker and Villasenor (1992) demonstrated that complete decorrelation of the SAR signal due to the movement of scatterers within pixels occurs with around 10 cm of movement for an L-band SAR system but with only 2-3 cm of movement for a C-band system. The wavelength of the microwave also affects the penetration depth, with longer wavelength energy penetrating further. This is particularly important when imaging volume scatterers, as it can alter the material that the SAR energy interacts with. For example in forested areas, L-band penetrates further into the canopy than C-band SAR and so interacts with branches rather than the leaves and twigs at the top of the forest. Clearly it is more likely for leaves to move by 2-3 cm than it is for branches to move by 10 cm between image acquisitions. Therefore in forested areas, L-band experiences less temporal decorrelation than C-band SAR, and the coherence difference between forested and unforested areas is more significant for C-band than L-band.

Therefore, while coherence is most commonly used to assess the signal quality of

an interferogram, it also represents a useful source of information in its own right. Previous studies have used SAR coherence to map building damage (Fielding et al., 2005; Yun et al., 2015), earthquake surface ruptures (Fielding et al., 2005), flooding (Chini et al., 2019), storm damage to trees (Fransson et al., 2010), to retrieve soil moisture information (Scott et al., 2017), and most recently for landslide detection. Figure 2.7 shows the expected signal of landslides in a time series of coherence maps. This expected behaviour forms the basis of the methods used by Aimaiti et al. (2019); Ge et al. (2019); Jung and Yun (2019); Olen and Bookhagen (2018) and Yun et al. (2015) and of the methods I apply here in Chapters 3, 4 and 5.
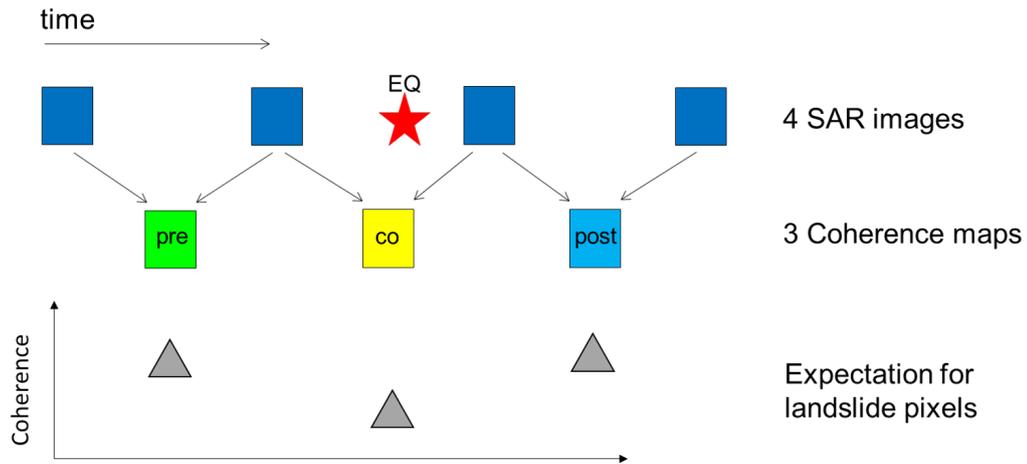
Figure 2.7: The expected signal of triggered landslides in a time series of pre-seismic, co-seismic and post-seismic coherence maps (labelled coloured squares) formed from SAR images (blue squares) acquired before an after an earthquake (red star).

2.5   Previous applications of SAR data to rapid landslide detection

With increased volumes of SAR data available following the launch of satellite systems such as Sentinel-1a and ALOS-2 in 2014, the advantages that SAR data could bring to rapid landslide mapping have become increasingly evident in recent years. Interest in the topic is increasing, and a number of studies have been published on the applicability of SAR data to landslide detection, particularly since 2018. These studies can be broadly divided into those which identify landslides through the decrease they cause in a co-event interferogram (as in Figure 2.7), and those which use the change caused by landslides to the intensity of the backscattered SAR signal.

In 2015, Yun et al. (2015) demonstrated that the difference between the co-event

and pre-event coherence, corrected for bulk changes in coherence, could be used to identify landsliding in the Langtang Valley triggered by the 2015 Gorkha, Nepal earthquake using data acquired by the ALOS-2 SAR sensor. Following this, a number of methods based on co-event coherence loss have been developed. The method of Olen and Bookhagen (2018) takes advantage of the high acqusition frequency of Sentinel-1 and uses a full year of data to characterise the pre-event coherence behaviour of every pixel. This provides a more robust measure of pre-event coherence and allows pixels whose coherence varies significantly to be flagged as unreliable. Jung et al. (2016) also developed a method based on co-event coherence loss, in which decorrelation of $\gamma_{temporal}$ (Equation 2.14) is modelled, allowing events which strongly alter coherence, in their case, ash deposited following a volcanic eruption, to be identified.

In this thesis, I focus on SAR coherence for rapid landslide detection, but the amplitude of the SAR signal is also emerging as an option. There is significant overlap between factors resulting in coherence loss (Section 2.4), and factors that alter the amplitude of the backscattered signal. Changes to the scattering mechanism, or dielectric properties of the ground surface will both decrease coherence and alter the amplitude. Amplitude is strongly sensitive to the orientation of a slope in relation to the SAR sensor but is less sensitive than coherence to changes to the orientation or exact locations of the scatterers, and is not likely to change due to e.g. windthrown trees (Fransson et al., 2010) or the movement of snow, which can cause false positives in coherence-based methods. The other side to this is that in the case where scatterers have moved due to a landslide but the scattering properties of the ground have not changed significantly, for example in the cases where a landslide has deposited rock over rock or has rotated scatterers rather than covering or removing them, amplitude methods are likely to be less sensitive than coherence methods to the change. Landslides can both increase or decrease SAR amplitude depending on the scattering mechanisms, dielectric properties and slope orientation relative to the sensor of the surface they disrupt before and after they occur.

Although some studies have concluded that SAR amplitude is not suitable for landslide detection (Czuchlewski et al., 2003; Masato et al., 2020), it has been demonstrated elsewhere that a number of SAR amplitude methods show some capability and so are worth discussing here. The simplest method, the difference in amplitude before and after an earthquake, has been employed by Konishi and Suga (2018) using Cosmo-Skymed imagery of rainfall-triggered landslides in the Kii Peninsula, Japan and by Ge et al. (2019), who applied the method to landslides triggered by the 2018 Hokkaido, Japan earthquake using ALOS-2 SAR imagery.

Similarly, Mondini et al. (2019) used the natural logarithm of the ratio of post-event to pre-event Sentinel-1 SAR amplitude, using a global set of 32 landslides for validation. Konishi and Suga (2019) further developed the method used by Konishi and Suga (2018) by applying a convolutional neural network to the backscattered amplitude difference, using ALOS-2 imagery of the 2018 Hokkaido, Japan earthquake. Konishi and Suga (2018) and Ge et al. (2019) also tested the correlation between the pre-event and post-event amplitudes for pixels within a moving window as a method for landslide detection, and Ge et al. (2019) also tested the difference in correlation for a pre-event and post-event pair of amplitude images and a pair of pre-event amplitude images. In all of these cases, the SAR amplitude methods applied showed some skill in landslide detection.

A number of studies have also used a combined coherence and amplitude approach to landslide detection, harnessing the advantages of both approaches. In mapping landslides triggered by the 2018 Hokkaido earthquake using ALOS-2 data, Jung and Yun (2019) apply the modelled $\gamma_{temporal}$ method of Jung et al. (2016) in areas where coherence is sufficiently high, but employ an amplitude-based method in incoherent areas. Aimaiti et al. (2019) used a decision tree methodology to combine pre-event to post-event amplitude difference, pre-event to co-event coherence decrease and slope for detection of landslides triggered by the 2018 Hokkaido earthquake, but found that an amplitude-only approach worked better.

These studies provide evidence that SAR data has potential in landslide detection, but comparison between the studies is difficult since they use different performance metrics and are assessed using different landslide inventories and at different spatial scales using data from a range of SAR satellites. It is therefore difficult to determine which method would be best to apply for a new earthquake, taking into consideration the SAR data available. It is also difficult to carry out any comparison between these methods and the results from empirical models of landslide likelihood, which are already employed following an earthquake to inform emergency response (e.g. Nowicki Jessee et al., 2018). The testing of SAR methods has also been relatively limited. Of the nine aforementioned studies, six were tested in Japan (Aimaiti et al., 2019; Ge et al., 2019; Jung et al., 2016; Jung and Yun, 2019; Konishi and Suga, 2018, 2019). The acqustion strategy and open-access data policy of the Sentinel-1 constellation mean these data are currently more likely to be available after an earthquake or rainfall event than data from other sensors, but only two out of the nine studies have tested their methods using Sentinel-1 SAR data (Mondini et al., 2019; Olen and Bookhagen, 2018). Therefore, while we have evidence that landslide detection using SAR is possible, further work remains before SAR methods can be applied routinely after an earthquake.

A New Method for Landslide Classification with SAR Coherence

Chapter Overview

In this chapter, I present a novel method of exploiting SAR coherence for rapid landslide detection. The work presented in this chapter was published in the journal Remote Sensing in January 2019 (Burrows et al., 2019). For the most part, text and figures from this publication are reproduced here verbatim under a creative commons licence. I have made some small changes made to the text in order to allow it to fit better within the thesis.

When I carried out the research presented in this chapter, there were very few methods of SAR-based rapid landslide detection (Konishi and Suga, 2018; Olen and Bookhagen, 2018; Yun et al., 2015), all of which employed methods originally developed for urban damage detection and had only been tested on a single catchment. The aim of this chapter was therefore to develop a method tailored towards landslide detection, and to test it at a much larger spatial scale. I therefore present a method which uses the difference between two different SAR coherence estimates to detect landslides, and test it using Sentinel-1 SAR data acquired over landslides triggered by the 2015 Gorkha, Nepal earthquake.

3.1 Introduction

The majority of continental earthquakes occur in mountainous regions, where they can trigger thousands of landslides over areas of tens of thousands of km^2 (Xu et al., 2016; Roback et al., 2018). These landslides are responsible for more deaths

globally that any other secondary hazard (Marano et al., 2010) and can significantly disrupt emergency response efforts (Datta et al., 2018; Global Logistics Cluster, 2015). Information on where landslides have occurred is therefore essential for emergency response coordination and for directing site-specific investigations on the ground (e.g. Collins and Jibson, 2015; Datta et al., 2018). This information must be rapidly generated and communicated in order to limit delays to resource allocation and therefore be of practical value (Fiedrich et al., 2000; Williams et al., 2018). As described in Chapter 1, manual mapping with optical satellite imagery, which is the most common method of generating these landslide data, is often too slow to be useful, particularly when the satellite imagery is obscured by cloud cover.

SAR presents an alternative source of landslide information to optical satellite imagery. Radar imagery can be acquired through cloud and is available within days of an earthquake anywhere on Earth. SAR data are routinely used to generate other data required for rapid response (e.g. Martinis et al., 2015; Meyer et al., 2015; NASA, 2018; Yun et al., 2015), and have been widely applied in monitoring the movements of slow moving landslides (e.g Confuorto et al., 2017; Mulas et al., 2016; Shi et al., 2014; Strozzi et al., 2005). However, when I began this PhD in 2016, the potential use of SAR in rapid production of landslide maps for emergency response had only been demonstrated on individual landslides or catchments, and with limited success (Yun et al., 2015; Konishi and Suga, 2018).

A clear example of the limitations of landslide mapping using optical imagery, and the potential that SAR has to overcome these limitations was the Gorkha earthquake on 25 April 2015, which triggered over 25,000 landslides in the surrounding mountains (Figure 3.1; Roback et al., 2018). Figure 3.2 shows a timeline of mapping efforts carried out by an international team of researchers using optical satellite imagery and intended for use by emergency response coordinators (Williams et al., 2018). Although the earthquake occurred during Nepal's dry season, cloud cover caused severe delays to landslide mapping, with almost no cloud-free imagery available in the first week following the earthquake and some areas remaining unmapped up until the onset of the monsoon on 9 June 2015, roughly six weeks later. The emergency response process evolves quickly in comparison. For example, the United Nations response framework following a disaster mandates an initial assessment after 72 hours and a second after 2 weeks (Williams et al., 2018; Inter-Agency Standing Committee, 2015). In the case of the 2015 Gorkha earthquake, the impending monsoon season applied additional time pressure, because the arrival of the monsoon would make cloud-free optical image acquisition unlikely and because it was anticipated that the earthquake would increase the severity of rainfall triggered landsliding (Datta et al., 2018; Robinson et al., 2019). The acquisition
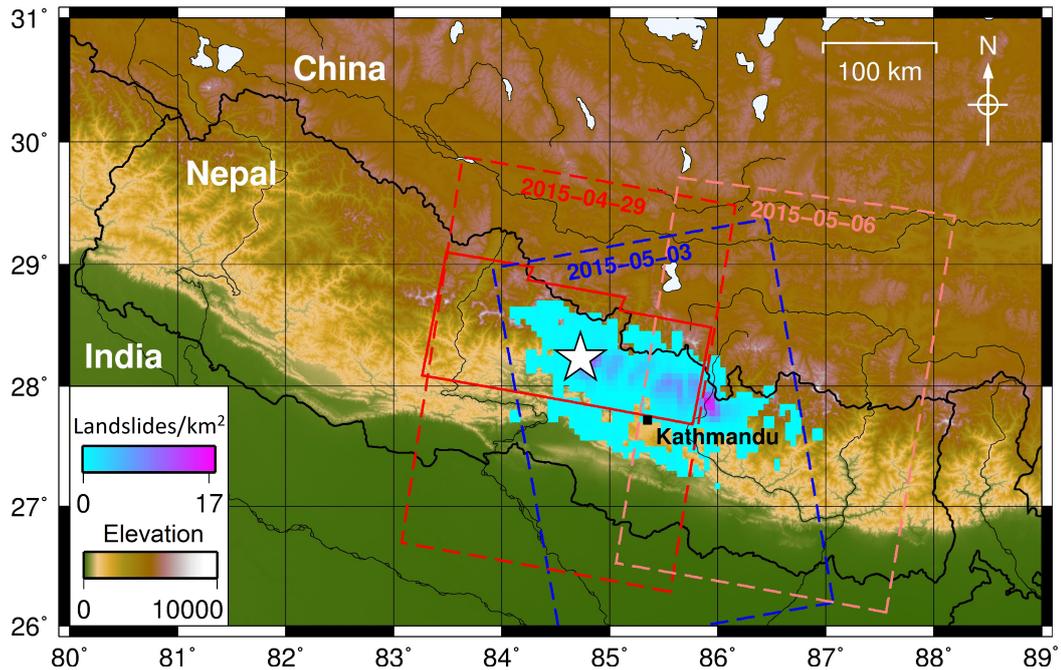
Figure 3.1: Location map of the 2015 Gorkha earthquake. A white star marks the epicentre of the mainshock on 25 April 2015. The density of the earthquake-triggered landsliding was calculated based on the inventory of Roback et al. (2018). The first post-event Sentinel-1a SAR acquisitions are shown with dashed lines: ascending track 85 (blue); descending track 19 (red) and descending track 121 (orange). The area of SAR imagery used in this study is from track 19 and is outlined in solid red.

of useable SAR imagery and generation of associated products occurred comparatively quickly (Figure 3.2). Five days following the earthquake, NASA's ARIA team released an initial damage proxy map for building damage in Kathmandu based on SAR data acquired by the Italian Space Agency's COSMO-SkyMed satellite system (Yun et al., 2015). The first post-event imagery acquired on each satellite acquisition track by ESA's Sentinel-1a satellite is shown on Figure 3.1, with the first of these being acquired 4 days after the Gorkha mainshock. Sentinel-1 coverage has since improved with the launch of a second satellite, Sentinel-1b, in 2016. Had it been possible to use SAR products in mapping landslides following the Gorkha earthquake, critical information on landslide distribution could have been delivered to first responders and government agencies with greater areal coverage and better timeliness than was possible from optical satellite data.

In this chapter, I investigate automatic methods to detect landslides using SAR and present a new method based on SAR coherence. I tested this method on the landslides triggered by the Gorkha earthquake, using a comprehensive independent inventory of triggered landslides produced from manual analysis of optical satellite imagery (Roback et al., 2018). Additionally, multiple reports have been published
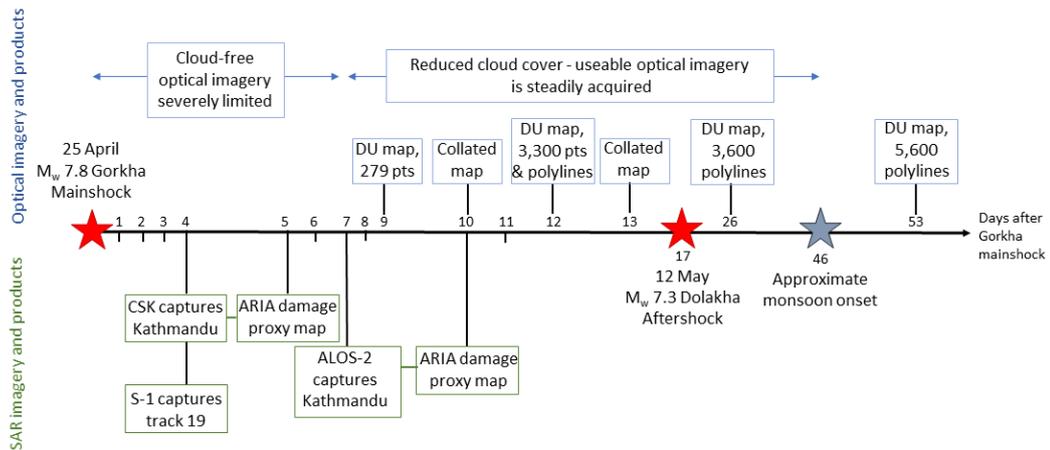
Figure 3.2: Timeline showing satellite image acquisition and product release following the 2015 Gorkha earthquake for optical satellite imagery and for SAR. Modified from Williams et al. (2018). Timeline of NASA ARIA products is taken from Yun et al. (2015). Optical imagery and products are in blue with maps produced by DU and collated maps coordinated with international partners (ICIMOD, MDA, NGA by the British Geological Survey. SAR imagery and products are in green and include the Sentinel-1 (S-1) imagery used in this study and the CSK and ALOS-2 imagery of Kathmandu used by the ARIA project.

discussing the emergency response effort following the earthquake, allowing identification of how SAR landslide products could have been used if they had been available (Global Logistics Cluster, 2015; Collins and Jibson, 2015; Datta et al., 2018).

3.2 Methods and Materials

3.2.1 Theory: landslide detection and SAR

3.2.1.1 Synthetic Aperture Radar: Interferometry and Coherence

As described in Chapter 2, two SAR images acquired by the same satellite system and covering the same area at different times may be combined to form an interferogram (e.g. Figure 3.3a). To acquire each image, microwave radiation is emitted by the satellite's antenna, back-scattered from the Earth's surface, and recorded again by the satellite as two components: amplitude and phase. An interferogram is a map of the difference in phase, $\Delta\phi$, between the two images; the repeated bands of colour can be considered as contours of the change in distance between the satellite and the imaged surface. Figure 3.3 shows an example pre-event interferogram before the 2015 Nepal earthquake, i.e., an interferogram made from two pre-event SAR images.
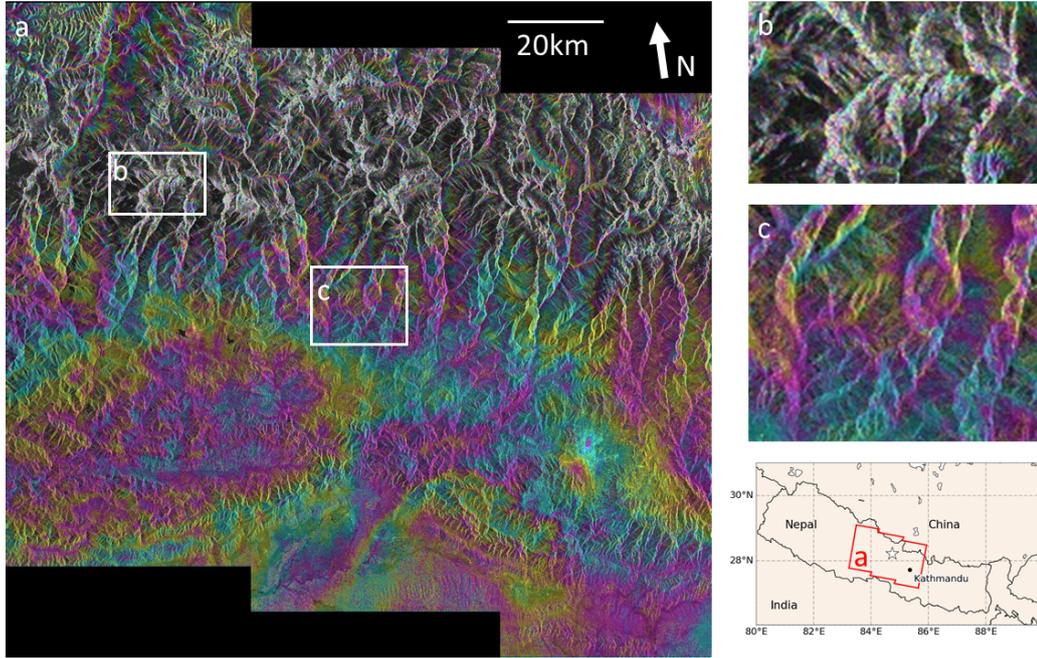
Figure 3.3: (a) Sentinel-1 interferogram produced using LiCSAR (Lazeckỳ et al., 2020) for a pre-event SAR image pair acquired on 24 March and 17 April 2015. Each band of colour shows a phase change between image acquisition equal to 2.8 cm. Background intensity show the amplitude of the image acquired on 17 April. (b) An example of an area where many pixels are incoherent. In this case, neighbouring pixels do not have a similar phase change and so do not sum constructively, resulting in a low boxcar estimation of coherence. (c) An example of an area of high coherence. Neighbouring pixels have similar phase change so sum constructively, resulting in a high estimation of coherence.

The coherence of a pixel can be thought of as a measure of the signal to noise ratio at a point in this interferogram. A map of estimated coherence is generated from the two SAR images used to form the interferogram to assess the spatial coherence in $\Delta\phi$ that is shown in the interferogram. SAR coherence, γ, is estimated as the correlation between $\Delta\phi$ of closely-grouped pixels and can be calculated pixel-by-pixel for a pair of images (denoted A and B) from an ensemble of n pixels using the following equation (reproduced from Equation 2.13).

$$|\gamma| = \frac{\frac{1}{n}\sum_{i=1}^{n} A_i \overline{B_i}}{\sqrt{\frac{1}{n}\left(\sum_{i=1}^{n}|A_i|^2 \sum_{i=1}^{n}|B_i|^2\right)}}$$

Here, i is an individual pixel and A_i and B_i are complex representations of phase and amplitude for images A and B respectively. The overline indicates the complex conjugate. The factor of $1/n$ is included here as a scaling factor in order to account for variations between pixels in the size of the ensemble, required for Section 3.2.1.4. In the widely used 'boxcar' coherence estimation, the ensemble is defined as a square box of pixels centred on the pixel in question. Pixels within the box will

sum constructively if they have similar $\Delta\phi$ and destructively if not. Examples of areas with low and high estimated coherence are shown in Figure 3.3b and 3.3c respectively.

As described in Section 2.4, the overall coherence of a pixel is determined by a number of factors, often illustrated by its decomposition into $\gamma_{spatial}$,$\gamma_{thermal}$ and $\gamma_{temporal}$ (Equation 2.14; Zebker and Villasenor, 1992). Here, we are concerned with $\gamma_{temporal}$, which is dependent on physical changes to the ground surface between the acquisition of two SAR images. Events which effect such changes, for example fire, flooding, building collapse or construction, earthquake surface rupture or landslides, alter the scattering properties of each pixel, leading to low temporal coherence and so a low observed coherence. Previous studies have demonstrated that SAR coherence can be used to map changes of this nature (NASA, 2018; Yun et al., 2015; Fielding et al., 2005; Nico et al., 2000; Vajedian et al., 2018; Yonezawa and Takeuchi, 2001); and that these products can be rapidly generated and released for emergency response purposes (NASA, 2018; Yun et al., 2015). Here I present a method based on SAR coherence exploitation designed specifically for landslide detection and test it alongside two existing methods.

3.2.1.2 Absolute Coherence Method

For two SAR images whose acquisitions span a landslide trigger event, landslide pixels are expected to have a low coherence. The occurrence of a landslide represents a significant modification of the ground surface and therefore its scattering properties. The simplest method of using coherence information to map landslides is to use this absolute coherence, assigning low-coherence pixels as 'landslide' and high-coherence pixels as 'not landslide'. For a few cases, landslides have been identified using this method, (e.g. Vajedian et al., 2018). However, as low coherence may be due to factors unrelated to the trigger event, such as the presence of dense vegetation or unfavourable imaging geometry, this method is likely to result in a classification surface with many false positives (low coherence regions that are classified as 'landslide' but are not landslides).

3.2.1.3 ARIA Method

It has been suggested that differencing a pre-event coherence map (calculated from two pre-event SAR images) and a co-event coherence map (calculated from two SAR images spanning the event) can differentiate between areas where coherence is always low and areas where it has decreased, e.g. due to building collapse or landsliding (Fielding et al., 2005; Yun et al., 2012, 2015). The method developed by
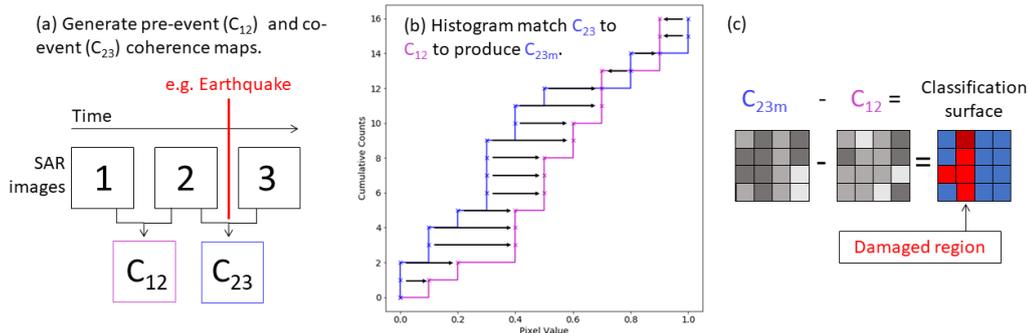
Figure 3.4: Workflow of the ARIA method (Yun et al., 2012, 2015) for identifying 'damaged' pixels, for example those which correspond to collapsed buildings or landslides given in 3 steps: (a) Generate coherence maps C_{12}, C_{23}. (b) Histogram match C_{23} to C_{12}. (c) Calculate the difference between the two coherence maps. Darker pixels in (c) have a lower coherence in C_{23m} and C_{12} and negative pixels in the classification surface are identified as 'damaged' i.e. those for which $C_{23m} < C_{12}$.

NASA's ARIA project for rapid generation of urban damage proxy maps is based on this approach (Yun et al., 2012, 2015).

Figure 3.4 shows the steps which go into producing ARIA damage proxy maps, described by Yun et al. (2012, 2015) Two pre-event SAR images and one post-event image are taken and used to calculate pre-event and co-event coherence maps. The histogram of the coherence values in the co-event coherence map is then 'matched' to the histogram of the pre-event coherence map in order to mitigate any bulk changes in coherence between the two images, for example due to variability in weather conditions. This histogram matching process is shown for the simple case of 16 pixels in Figure 3.4, in which the co-event cumulative histogram is mapped onto the pre-event histogram. For this step, pre-event and co-event pixels are sorted by value. In order to obtain a strict ordering, co-event pixels are sorted first by their value and then by the values of the eight pixels around them as in Coltuc et al. (2006). The ordered co-event pixels are set equal to the values of the ordered pre-event pixels, and then placed in their original spatial positions, resulting in a co-event coherence map whose coherence frequency distribution is identical to that of the pre-event map. The histogram-matched co-event map and the pre-event map are then differenced to produce a classification surface. For their purposes, the ARIA team then classify pixels whose co-event coherence is lower than their pre-event coherence as 'damaged', with increasing confidence in more negative pixels (Figure 3.4c).

The ARIA method was originally developed for urban damage mapping. However, when applying the method following the 2015 Gorkha earthquake, Yun et al. (2015) noted that it showed some promise in landslide detection. Yun et al. (2015)
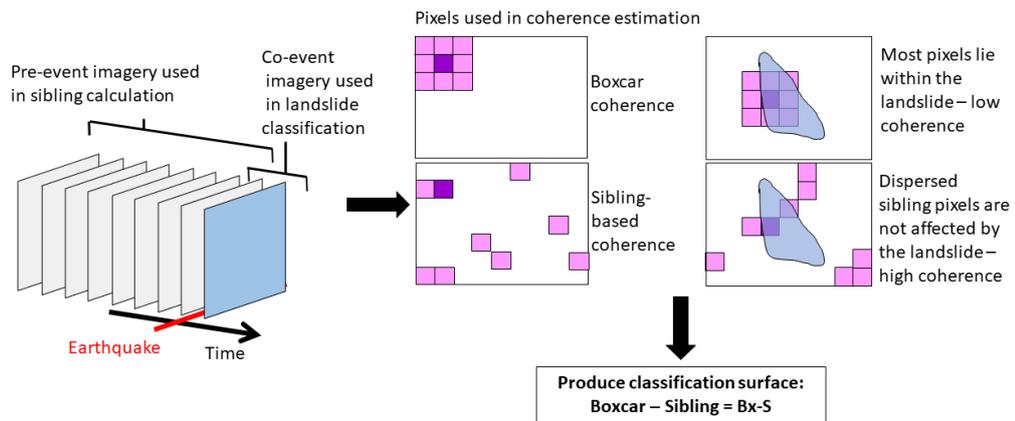
Figure 3.5: Workflow for the Bx-S method, in which the difference between sibling-based and boxcar coherence estimates is used in landslide classification

identified an area of decreased coherence spatially correlated with the Langtang Valley landslide, an exceptionally large and destructive landslide triggered by the earthquake Kargel et al. (2016). However, Yun et al. (2015) judged that overall, coherence was not sufficiently stable through time in vegetated regions, resulting in many false positives: pixels incorrectly identified as damaged due to coherence changes unrelated to the earthquake.

3.2.1.4 Sibling-based coherence method

The new method I have developed is outlined in Figure 3.5. As with the ARIA method, the aim is to produce an expected landslide-free coherence surface, which is subtracted from the co-event coherence map. However, where Yun et al. (2012, 2015) subtract a pre-event coherence map, I subtract a co-event coherence map that is calculated in such a way as to be less sensitive to localised decreases in coherence such as landslides. Unlike the ARIA method, the new method is not based on the change in coherence through time and so is expected to have fewer false positives caused by variations in temporal coherence unrelated to landsliding.

As an alternative to the boxcar coherence described in Section 3.2.1 and used in the absolute and ARIA methods, SAR coherence can be calculated based on ensembles of 'sibling' pixels, which exhibit similar behaviour to the target pixel (Deledalle et al., 2014; Ferretti et al., 2011; Spaans and Hooper, 2016, e.g.). Here, I use the RapidSAR algorithm of Spaans and Hooper (2016) for this process. For every pixel, a search is performed within a window of a given size, centred on that pixel, for pixels behaving similarly in terms of amplitude and amplitude variability throughout a time series of pre-event imagery. These pixels are designated as

'siblings'. The sibling ensemble of each pixel is then used in place of the boxcar of adjacent pixels in the summations in Equation 2.13.

When using a boxcar ensemble in estimating the coherence of a pixel that lies within a landslide, the pixels used in the summation are adjacent and so are likely to also lie within the landslide when the landslide in question is similar in size or larger than the boxcar. Since a landslide modifies the scattering properties of the Earth's surface, giving pixels within the landslide random $\Delta\phi$, the ensemble is expected to sum destructively, resulting in a low coherence estimate. Additionally, any coherent pixels within the landslide will still be estimated as low coherence due to the random $\Delta\phi$ of their neighbours. However, the sibling-based coherence estimate calculated using RapidSAR uses an ensemble of pixels dispersed throughout a window much larger than the size of a boxcar and specified to be larger than the expected size of individual landslides. Compared to the boxcar ensemble, it is expected that proportionally fewer siblings of a landslide pixel will lie within the landslide. Pixels lying outside the landslide will not experience the random $\Delta\phi$ associated with it and so may sum constructively. The landslide pixel is thus given an estimated coherence value that is more dependent upon its siblings, which lie outside the landslide.

The sibling-based coherence calculated by RapidSAR is relatively insensitive to small spatial scale changes in the ground surface such as landslides. This map can therefore be thought of as the co-event coherence map we would expect if there were no landslides. The method I propose is to subtract this sibling-based coherence map from the co-event boxcar map, producing a classification surface, which will be referred to subsequently as boxcar - sibling (Bx-S). Landslide pixels should have a lower boxcar coherence than sibling-based coherence and so be negative in the Bx-S surface. Since the same pair of images is used in the coherence calculation with both methods, the histogram matching step carried out in the ARIA method (Yun et al., 2012, 2015) becomes unnecessary and the potential for other sources of temporal decorrelation is decreased.

3.2.2 Case Study: The 2015 Gorkha Earthquake

3.2.2.1 Validation Data

I analysed the classification ability of the three methods presented in Section 3.2.1 — absolute coherence, ARIA and Bx-S — using the inventory of landslides triggered by the 2015 Gorkha earthquake that was compiled by Roback et al. (2018). The inventory consists of 24,915 landslides mapped as polygons that include both scar

and runout. The majority of landslides were mapped using pre- and post-event imagery from DigitalGlobe Worldview-2 and -3 with some landslides mapped using Pleiades and Google Earth imagery. Due to restrictions on the SAR imagery available for the event, I use a subsection of this area containing 16,539 landslides, the extent of which is shown on Figure 3.1 (solid red line).

3.2.2.2   SAR Data and Processing

C-band Sentinel-1a SAR imagery acquired on descending track S019d (dashed red line, Figure 3.1) was used in this study. Acquisition dates are shown in Figure 3.6. This includes a long time-series of pre-event imagery, which is required for sibling calculation in the new method presented in Section 3.2.1.4. The occurrence of the Gorkha earthquake early in the lifetime of Sentinel-1a and prior to the launch of Sentinel-1b meant that data acquisitions on ascending track S085a, and on the descending track east of Kathmandu, S121d (Figure 3.1), were less regular before the earthquake than on S019d and so I did not use these data in this chapter.

Interferograms and coherence maps were produced for consecutive date pairs using the LiCSAR software package (Lazeckỳ et al., 2020), which uses GAMMA software to process Sentinel-1 single look complex data. A 1-arcsecond DEM digital derived from SRTM data (Farr et al., 2007) was used in this processing. The raw SAR data had a pixel size in the radar coordinate system of 2.3 m $\times$ 14.0 m (range $\times$ azimuth). Images were multi-looked by a factor of five in range and one in azimuth, giving a pixel size of 12 m $\times$ 14 m. Boxcar coherence was calculated using pixels within a 3×3 pixel window. To calculate the sibling-based coherence, I used the RapidSAR algorithm of Spaans and Hooper (2016). For every pixel, a window of 41×41 pixels was searched and between 15 and 100 pixels were identified which behaved similarly in terms of amplitude and amplitude variability throughout 11 pre-event images acquired up until 5 April 2015 (see Figure 3.6 for acquisition dates).

Once the three classification surfaces had been calculated according to the methods outlined in Section 3.2.1, these were converted to a geographic coordinate system, with a pixel size of 20 m $\times$ 22 m, which reflects the multi-looked resolution of the data. I carried out the analyses presented in Section 3.3 in this coordinate system. Each classifier surface was then rescaled to produce a surface with values between 0 and 1, where 1 was most likely to be a landslide.
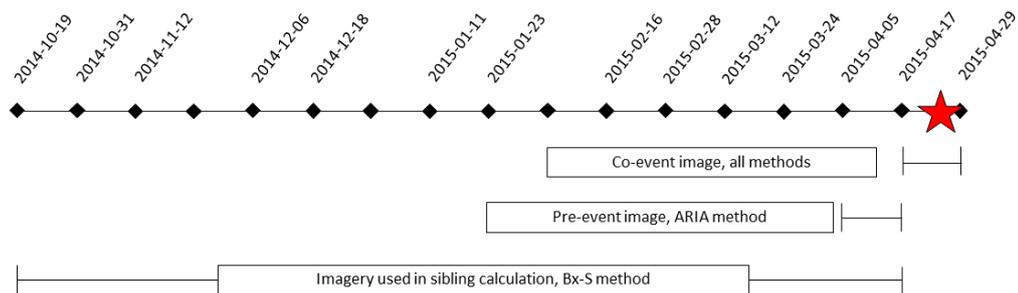
Figure 3.6: Timeline of Sentinel-1a image acquisition for the study area (see Figure 3.1) over the months preceding the Gorkha earthquake (red star), showing the imagery used in each method. Black diamonds show satellite overpasses at intervals of 12 days. Those where imagery was acquired are labelled with dates.

3.2.2.3 ROC Analysis

A common problem in classification is the choice of threshold at which to assign classes given a continuous classifier. This choice of threshold is strongly dependent on the user requirements and their relative tolerance for false positives and false negatives and so it is preferable to test the performance of a classifier before setting this threshold. I therefore used receiver operating characteristic (ROC) analysis to test the landslide detection ability of each of the three classification surfaces described in Section 3.2.1. ROC curves are commonly used to measure the ability of a continuous classifier to correctly identify a binary array (Beguería, 2006), in this case, a map of landslides and non-landslide pixels. For a range of classifier threshold values, the true positive rate (the fraction of mapped landslide pixels that are correctly classified as 'landslide') is plotted against the false positive rate (the fraction of mapped non-landslide pixels that are incorrectly classified as 'landslide'). As the threshold is relaxed from a value where all pixels are classified as 'non-landslide' to one where all are classified as 'landslide', a good classifier will identify true positives at a faster rate than it accepts false positives. The ROC curve plots the true positive rate against the false positive rate, with better classifiers resulting in a curve that lies closer to the upper left-hand corner of the plot. The overall performance of a classifier can therefore be quantified by the area under the curve (AUC). For a random classification surface where any pixel has a 50% chance of being classified as landslide or non-landslide, the ROC plots as a straight line between (0,0) and (1,1) with AUC = 0.5. A classifier AUC is expected to lie between 0.5 and the perfect case, for which AUC = 1.0.

ROC analysis has been widely used to assess the performance of models and automated landslide detection methods (Hong et al., 2015; Robinson et al., 2017; Tanyas et al., 2019, e.g.). The choice of ROC AUC as a metric for classifier performance in

this chapter and in Chapters 4 and 5 is therefore not unusual. It allows a classifier to be assessed before a threshold is set, and places value on both true positives and true negatives, both of which are directly relevant to resource allocation in an emergency response situation. However it is necessary to examine the effects of this choice on the results presented in the thesis. First, ROC analysis is dependent on the spatial scale at which it is carried out, and on the format and area of the validation data used, thus ROC AUC values from this thesis should not be compared directly with those from other studies. Second, while ROC AUC values indicate the success of a model in predicting a dataset, two models with the same ROC AUC can have different predictive abilities if the curves have a different shape (Vakhshoori and Zare, 2018). Finally, ROC AUC values can be influenced by imbalance in the validation data (Saito and Rehmsmeier, 2015). In the case of landslides, imbalance is inevitable since there are many more non-landslide than landslide pixels. Therefore comparison of two methods using ROC analysis must be done on the same event, since different events may have different ratios of landslide and non-landslide pixels.

3.2.2.4 Masks

In order to test the classification ability of each surface, it was necessary to mask pixels which were either not mapped in the landslide inventory or which were not well imaged by the SAR system. Based on the data of Roback et al. (2018), I applied masks to remove pixels that were either outside the mapped area or obscured by cloud in the optical satellite imagery (Figure 3.7).

I also masked areas where the SAR system was not likely to capture useable data based on viewing angle of the satellite and topography. The SAR system images the Earth's surface at an oblique angle, locating pixels according to their two-way travel time and Doppler shift, and projecting them onto a two-dimensional image. Steep topography can distort this image, leading to phenomena known as shadowing, foreshortening and layover (detailed in Chapter 2). In order to assess this effect, I used the σ_0 radar backscatter normalisation area calculated using the pixel area integration method described in Frey et al. (2012). This method divides the DEM surface covering the SAR image into small patches. The patches of the DEM surface that correspond spatially to each radar pixel are then integrated in order to approximate the area on the ground that contributes to each pixel. I used this σ_0 normalisation area to identify distorted pixels. A mask was applied to remove all pixels for which this contributing area is 0 and those for which the contributing area was >1000 m^2 (around 6 times larger than the pixel spacing
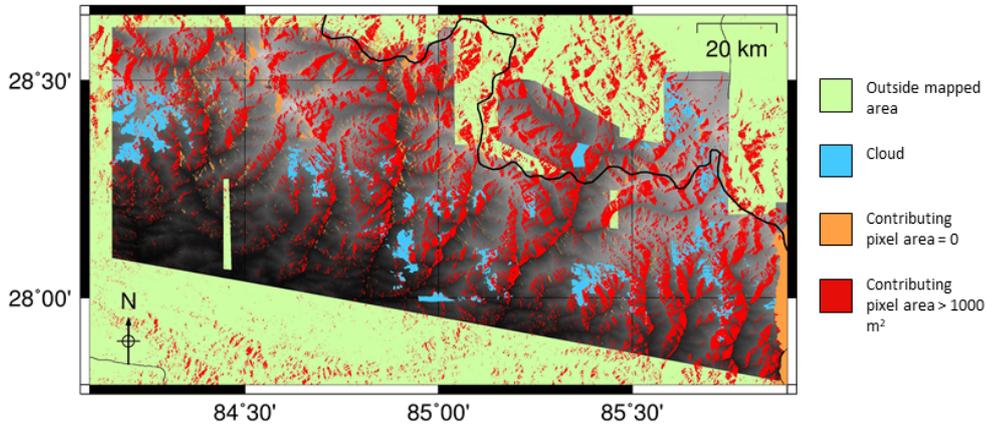
Figure 3.7: Regions that were masked before analysis was carried out, either due to being unmapped by Roback et al. (2018) (green, blue), or because of poor SAR image quality, identified using the contributing pixel area (orange,red). Underlying surface shows topography.

in radar coordinates) since these were expected to contain little information on landsliding. The selection of this threshold of 1000 m^2 is justified in appendix A.

3.3 Results

Both maps of individual landslides and of landslide density are useful in the emergency response process (Williams et al., 2018). I therefore assessed each classification surface in terms of their ability to: (1) identify individual landslides at a pixel-by-pixel scale; and (2) identify areas that had experienced extensive landsliding at a series of increasingly coarse spatial scales. To do this I produced aggregate classification surfaces, for which the original surface was divided into N × N pixel squares and the mean pixel value within each square was taken as the aggregate classifier value. These were then normalised as before to produce a surface of values between 0 and 1 for each classifier. A landslide density surface was calculated as the percentage mapped landslide area of each aggregate pixel. For the purpose of ROC analysis, which requires a binary validation dataset, I assigned aggregate pixels with over 50% landslide density as 'landslide' and those with under 50% 'non-landslide', although I also test the sensitivity of all methods to this choice.

Figure 3.8 shows a map of landslides from (Roback et al., 2018) and each normalised coherence-based classification surface. Two areas are shown, selected to contain different sizes of landslides. The first is around the Village Development Committee (an administrative region) of Jharlang, located in the Himalayan foothills within Dhading District. The second area covers the Langtang Valley in Rasuwa District,
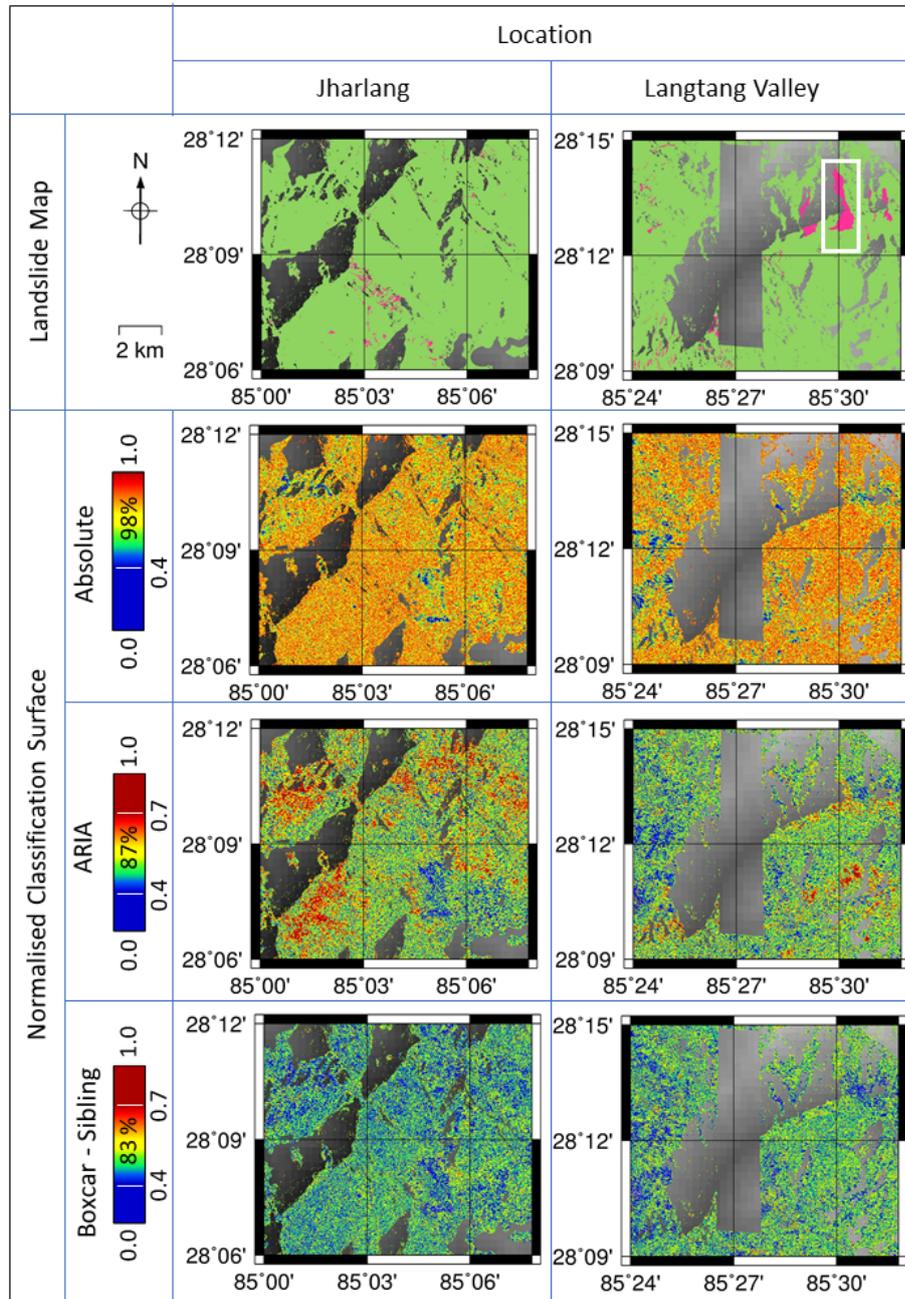
Figure 3.8: Classification of individual landslides for two example locations. Each column shows mapped landslide polygons (pink) (Roback et al., 2018) and the normalised classification surface calculated from each method for the Jharlang (left) and Langtang Valley (right) regions. Colour bars are non-linear but linear between the white lines and labelled with the percentage of pixels across the two areas that lie in this linear range. The main body of the Langtang Valley landslide is indicated in white.
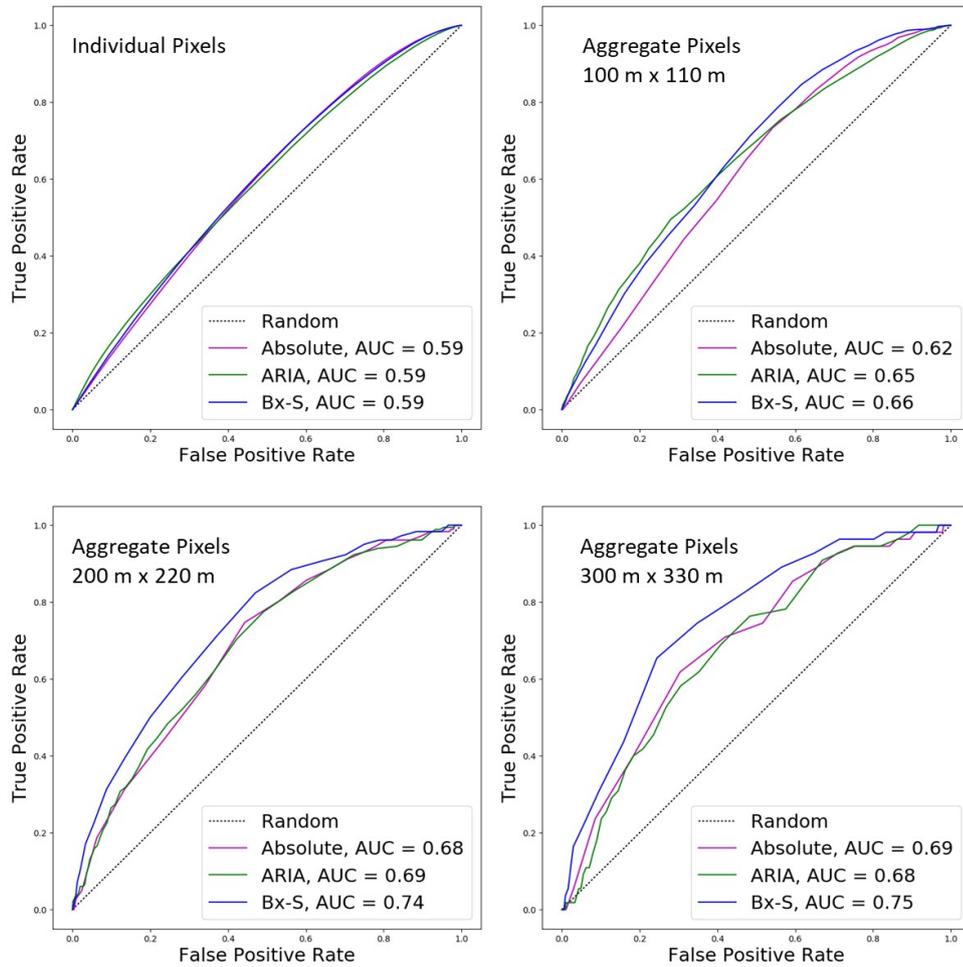
Figure 3.9: ROC curves for three different SAR coherence-based classifiers, plotted at a range of resolutions from individual 20 m x 22 m pixels up to 300 m x 330 m aggregate pixels. The dotted lines show the performance of a random classifier (AUC=0.5). Masks shown in Figure 3.7 were applied to the data before calculation. The Bx-S method outperforms the other classifiers for aggregated pixels.

where an exceptionally large landslide with an area of 1.7 km^2 led to hundreds of fatalities (Collins and Jibson, 2015; Kargel et al., 2016). As was found by Yun et al. (2015), the large landslide in the Langtang Valley is visible in the ARIA classification surface. However, in the Jharlang area, where landslides were smaller, the ARIA method was less successful, and the surface is noisy. The new method, Bx-S struggles to differentiate between landslide and non-landslide pixels in both locations, as does absolute coherence, which suffers from false positives.

ROC analysis confirms that all three methods perform poorly as landslide classifiers on a pixel-by-pixel scale, with AUC < 0.6 (Figure 3.9). However, Bx-S and
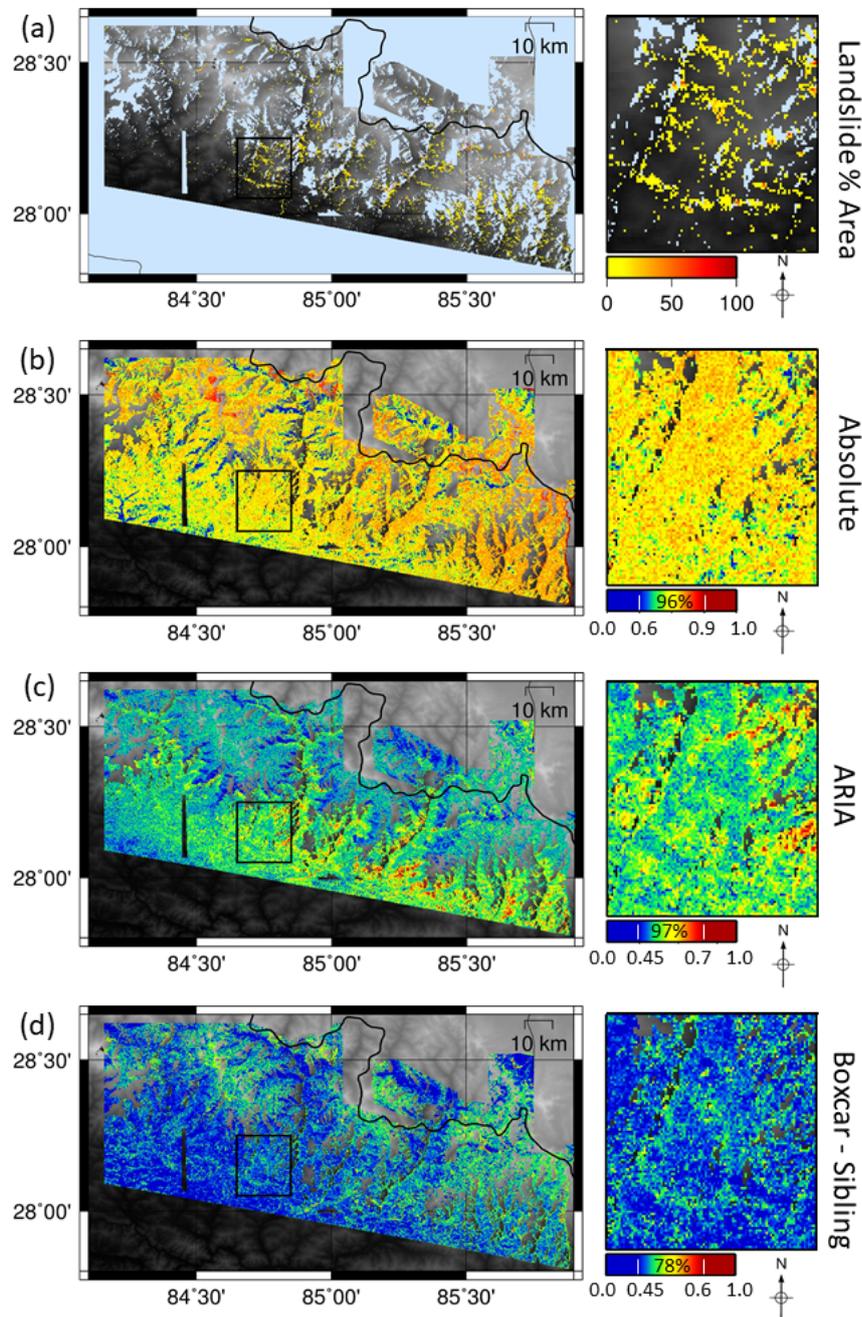
Figure 3.10: Classifier surfaces for 200 m × 220 m aggregate pixels (a) the percentage of each aggregate pixel made up of landslide pixels. (b-d) the mean value of the classification surface for each method within each aggregate pixel. These surfaces are normalised to a range between 0 and 1 with 1 being most likely to be a landslide. Colour bars are non-linear, but linear within the white lines and labelled with the percentage of pixels across the whole area that lie in this linear range.

to a lesser extent ARIA and absolute coherence are more successful at identifying areas of intense landsliding. ROC analysis shows that increasing pixel size through aggregation results in improved performance for all methods. In particular, Bx-S outperforms the two existing methods at all aggregations and does better with increasing aggregation. For Bx-S, the AUC value increases from 0.56 to 0.77 when aggregated from 20 m $\times$ 22 m pixels to 300 m $\times$ 330 m. For the same aggregation, absolute coherence AUC increases from 0.55 to 0.72 and the ARIA method AUC increases from 0.57 to 0.68. Figure 3.10 shows classification surfaces for the whole area at an aggregated pixel size of 200 m $\times$ 220 m (10 $\times$ 10 pixels), along with a smaller region within Gorkha district. In this smaller region, Bx-S appears relatively successful in recreating the spatial pattern of landslide density, while ARIA and absolute coherence have many false positives, making it difficult to identify the correlation with landslide density. To allow direct comparison, the inset region in Figure 3.10 is shown in Figure A.2 (Appendix B) prior to aggregation.

Several factors exerted a relatively strong influence on classification ability for the different classifiers: one related to spatial scales, a second to the time window of SAR acquisition, and a third to the definition of 'landslide' pixels. First, increasing the size of the boxcar window worsens performance for all three classifiers. I have presented all results in this chapter using a 3 $\times$ 3-pixel window but I also tested 5 $\times$ 5 and 20 $\times$ 20 windows. In most cases increasing the size of the boxcar window reduced AUC, although not for the Bx-S classification surface (Table 3.1). I carried out the comparison on aggregates of 10 $\times$ 10 individual pixels. This was in order to lessen the effect of coarsening resolution on classification ability discussed above.

Table 3.1: ROC AUC values for each method for Boxcar window sizes 3 $\times$ 3, 5 $\times$ 5 and 20 $\times$ 20. ROC AUC are shown for 200 m $\times$ 220 m aggregate classifier surfaces

	3 $\times$ 3	5 $\times$ 5	20 $\times$ 20
Absolute	0.68	0.68	0.66
ARIA	0.69	0.69	0.64
Bx-S	0.74	0.73	0.73

Second, for all three classifiers, classification ability worsened when the time window between SAR image acquisition was increased. This was expected as a longer time window will have increased temporal decorrelation unrelated to landsliding, particularly in vegetated areas. Third, results were affected by how aggregate 'landslide' pixels were defined. For the purposes of ROC analysis, an aggregate landslide pixel was defined as one comprising at least 50% individual landslide pixels. In varying this threshold, I found that ROC AUC was higher when landslide pixels were more strictly defined by a higher threshold (Table 3.2). The classifiers are therefore better able to identify a region that has experienced more severe

Table 3.2: The effect on ROC AUC of varying the % landslide area threshold required for an aggregate pixel to be defined as 'landslide'

	10%	20%	30%	40%	50%	60%
Absolute	0.65	0.67	0.68	0.69	0.68	0.69
ARIA	0.65	0.65	0.67	0.68	0.69	0.69
Bx-S	0.67	0.70	0.72	0.73	0.74	0.75

landsliding, which may affect how they can be applied. I also tested the effect of altering the size of the RapidSAR search window from 41×41, which is used throughout this study, to 21×21, 61×61 and 81×81. This had little effect on AUC on both individual and aggregated pixel surfaces (no more than 0.01 difference) but computation time was noticeably different. The time taken for an 81×81 window was around double that of the 21×21 window.

3.4 Discussion

3.4.1 Pixel Aggregation

I found SAR coherence methods to be more successful in landslide detection at lower spatial resolutions. There are several potential reasons for this. First, any disagreement in landslide shape or location between the SAR classifier and the validation map will have a negative effect on the ROC analysis since non-overlapping 'landslide' pixels between the two maps result in both false positives and false negatives. Therefore, any problems in geo-referencing in either the coherence maps or the validation inventory will adversely affect classifier performance. This is particularly relevant in the case of Nepal, where Roback et al. (2018) note considerable difficulty in orthorectifying and georeferencing the imagery from which the landslides were mapped. Furthermore, any additional landslides or change in existing landslide shape through landslide reactivation between SAR and optical image acquisition would have the same effect. Reactivation is likely to occur due to unstable ground conditions, rainfall and aftershock activity. The SAR imagery used here was collected 4 days following the earthquake, whereas the optical imagery used by Roback et al. (2018) was acquired over a period of several months. It is also worth noting that as well as landslides, the Bx-S method may detect other forms of damage, such as collapsed buildings or damaged roads. Although this may be a useful application of the Bx-S method for future studies, here this may result in additional false positives, as these areas would not be included in the inventory of individual landslides.

Second, there are likely to be limitations on the size of an individual landslide that can be detected both by the individual collecting the optical landslide inventory and by the SAR classifier. Of the 24,915 landslides mapped by Roback et al. (2018), 6,028 ($<$25%) are under 400 m^2 in area, the size of one SAR pixel, while more than half are smaller than the 3×3 pixel boxcar window. (Figure 3.11). The calculation of the boxcar coherence as a spatial average means that sub-pixel landslides are unlikely to be visible and sharp boundaries in coherence are blurred. Using a 3×3 pixel window, 9 pixels will be used in the summation in equation 2.13. For two adjacent pixels, 6 of these will be the same. Sharp coherence changes are therefore spread across the boxcar window (Spaans and Hooper, 2016). The blurring between neighbouring pixels may mask the signal of small landslides, making pixel scale detection problematic. This affects all three methods, as all use a boxcar coherence estimate to detect landslides. However, this problem is reduced when using SAR coherence to estimate coarser resolution landslide density, since a mean is taken of neighbouring pixels in the aggregation process.

3.4.2 The Maximum Detectable Landslide Size

The size of the search window used by RapidSAR for sibling identification is likely to set an upper limit on the maximum size of a landslide that can be detected using the Bx-S method. The method relies on a sibling-based coherence estimate using
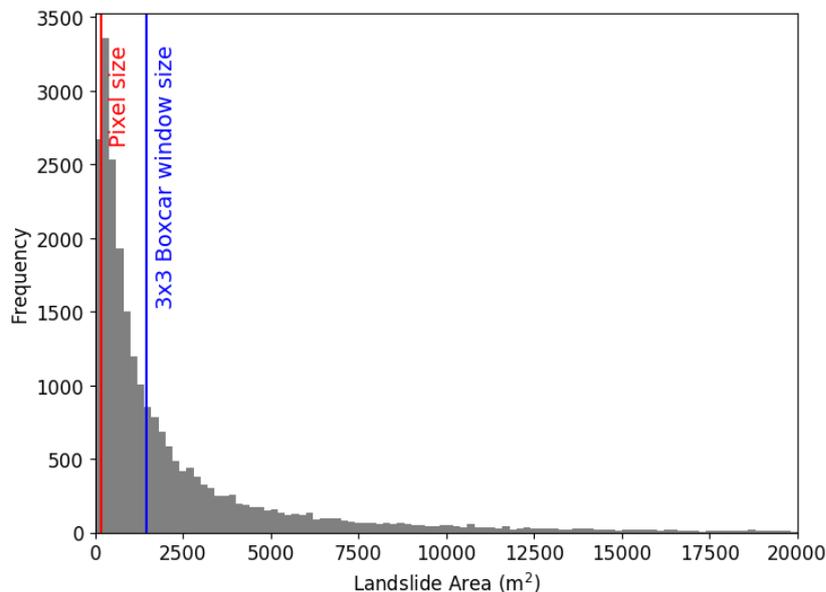
Figure 3.11: Histogram of landslide areas derived from the inventory of Roback et al. (2018). Landslides over 20,000 m^2 in area are omitted for clarity. The sizes of an individual pixel (red) and of the window used in calculation of the boxcar coherence (blue) are marked.

proportionally fewer landslide pixels in the summation than the boxcar estimation (Equation 2.13). I make the assumption that siblings of a given pixel will generally be distributed widely throughout the search window and will not be clustered around it as immediate neighbours. However, for a pixel located at the centre of a landslide that is larger than the RapidSAR window, both of the ensembles of pixels used by the boxcar and sibling-based coherence estimates will lie entirely within the landslide. Both estimates of coherence therefore yield a low value and the difference between them will be small, leading to a false negative. This effect will decrease towards the edges of the landslide.

The largest landslide included in the Roback et al. (2018) inventory is the Langtang Valley landslide (Figure 3.8), which has an area around 1.7 km^2. Here I used a 41 × 41-pixel window, equivalent to an area around 270,000 m^2. In radar coordinates, the Langtang Valley landslide is 221 pixels in length but has a mean width of just 30 pixels. At its widest point, it is 58 pixels wide. In the centre of the Langtang Valley landslide, I therefore expect to approach the point where both coherence estimates are very low. Therefore, although decreasing the size of the search window decreased computation time, I did not use a smaller 21 × 21 window in this study. In future studies, where the maximum landslide size is unknown, it will be necessary to increase the size of the RapidSAR search window in order to ensure that large landslides are not masked.

3.4.3 Ascending and Descending Track SAR

In Section 3.2.2.4, a mask was applied to remove areas of the classification surfaces that were not expected to contain useful information due to the topography and satellite image acquisition parameters. Application of this mask resulted in exclusion of 23% of the study area. However, exclusion is strongly biased towards those slopes facing away from the sensor and is thus often limited to one side of a valley. Therefore, if landsliding occurrence is assumed independent of slope aspect, it remains possible to obtain a relative estimation of regional landslide density. I do note, however, that care should be taken in areas where vegetation cover varies with slope aspect, as this could introduce aspect-related variations in landslide susceptibility.

It is also important to note that, since the locations of these masked regions are dependent on the viewing angle of the satellite, they are different for ascending and descending track SAR. I used descending track imagery, which is acquired from a west-facing sensor, so that steep, west-facing slopes were not well imaged and had to be masked. For ascending track imagery, the opposite would be true. Here,

ascending track SAR imagery was not used; however, it will be advantageous in future studies to combine both ascending and descending track SAR imagery in order to maximise the area that can be mapped using SAR.

3.4.4 Combining Classifiers

Predictive landslide models, (e.g. Gallen et al., 2017; Kritikos et al., 2015; Robinson et al., 2017), rely on a combination of predictors of landslide distribution that together provide a more accurate model than any one individual predictor. One possible way of improving the classification ability of SAR-based methods would be to combine them with one or more such empirical predictors. Various possible landslide predictors such as slope, lithology and distance to rivers and faults; and means of combining them have been tested and developed (Gallen et al., 2017; Kritikos et al., 2015; Robinson et al., 2017; Reichenbach et al., 2018). Using SAR data as an additional input for one of these models would allow incorporation of observed data into models that are traditionally static in time based on pre-earthquake conditions and prior knowledge of landslide likelihood. This is further explored in Chapter 5 of this thesis.

Alternatively, landslides mapped by SAR could be used to calibrate predictive models. Robinson et al. (2017) used small areas of mapped landslides as training data to predict landslide occurrence across Nepal following the Gorkha earthquake. They found that while the input of observed landslide data improved model performance, the improvement was considerably reduced if these observations were clustered. This clustering is common in optically-derived datasets if mapping is only possible through small gaps in cloud cover. SAR methods may provide a more uniformly distributed set of observations that could be used in the calibration of predictive models. Areas where the SAR coherence was likely to be most reliable could be identified for this purpose, either by masking areas with high normalised backscatter as I have done here, by identifying areas where coherence was consistent and non-zero in pre-event imagery (as in Jung and Yun, 2019), or by using a method such as that of Rees (2000) to predict areas where topographic effects (e.g. shadowing) might be problematic based on DEM data and satellite image acquisition parameters. For my case study, I was still able to make landslide observations across a wide area, lessening the clustering effect, even after masking unreliable SAR data.

SAR products other than coherence may also be used in landslide identification. For example, SAR amplitude has shown capacity for detection of individual large landslides (Mondini et al., 2019), but is not considered reliable enough to be used

alone in large-scale landslide identification (Czuchlewski et al., 2003). SAR amplitude is dependent on the proportion of microwave energy that is scattered at the Earth's surface. Vegetation tends to scatter a relatively high proportion of this energy when compared to exposed rock or bare ground so that the amplitude of the signal when it is returned to the satellite is lower for vegetation than for rock. Since landslides remove vegetation, they are expected to correspond to bright areas in an amplitude map and to increased amplitude in time. However, this is an oversimplification and a large number of factors can affect SAR amplitude. I tested SAR amplitude in an initial analysis but found it to be outperformed by coherence-based classifiers, so do not report it here. However, SAR amplitude methods are likely to perform better in highly vegetated regions, and therefore may be complementary to coherence-based methods, that are adversely affected by low background temporal coherence in these areas. Recently, Jung and Yun (2019) and Aimaiti et al. (2019) have successfully combined SAR coherence and amplitude methods for landslide detection.

3.4.5 SAR Frequency Band

Sentinel-1a C-band SAR was used in this study because it had good temporal coverage in the months prior to the 2015 Gorkha earthquake, the short 12-day revisit time improves temporal coherence, the data are easily and openly available, and frequent coverage means that this satellite constellation may be used in future emergency response. Many SAR-based landslide studies also use either X-band or L-band SAR (Bonì et al., 2018; Confuorto et al., 2017; Konishi and Suga, 2018; Mulas et al., 2016; Rosi et al., 2018; Shi et al., 2014; Strozzi et al., 2018; Yun et al., 2015). X-band SAR has a shorter wavelength than C- and L-band, which makes it able to detect smaller ground movements at higher spatial resolution. However, due to increased penetration of SAR microwaves through the canopy at longer wavelengths, L-band SAR retains higher temporal coherence than C-band in vegetated regions (Shi et al., 2014; Strozzi et al., 2005; Yun et al., 2015), whilst coherence of X-band SAR imagery for the same regions is very low (Konishi and Suga, 2018; Yun et al., 2015). Since all three methods discussed in this chapter rely on non-landslide pixels having a reasonable background coherence, I did not attempt to use X-band data for the Gorkha earthquake case study, due to the heavy vegetation cover in this region. Whilst the higher temporal coherence of L-band SAR may provide a significant advantage in vegetated regions, this may be negated if there is a long time between image acquisitions. When testing the ARIA method using L-band imagery collected by the ALOS-2 satellite system for the Gorkha earthquake, Yun et al. (2015) found L-band SAR to perform poorly in

rural, vegetated areas. In order to obtain the two pre-event and one co-event images required for their method, Yun et al. (2015) were required to use imagery spanning 7 months. Over this time, vegetated regions underwent considerable change, resulting in changes in coherence unrelated to landsliding or earthquake damage. Since the Gorkha earthquake occurred early in the lifespan of ALOS-2, the pre-event imagery acquired was not sufficient for the sibling identification required by the Bx-S method presented here, so it could not be tested with L-band SAR. However, for future events with more complete pre-event image acquisition, the increased coherence of L-band SAR in vegetated regions may increase the classification ability of SAR-coherence-based methods. Equally, these methods may perform even better with C-band SAR for regions that are less densely vegetated than Nepal. A comparison between L-band and C-band is presented in Chapter 4.

3.4.6 Alternative Methods of Coherence Estimation

The method I present here exploits the difference between a boxcar estimation of coherence and a sibling-based estimation. Here I used the RapidSAR algorithm to calculate this sibling-based estimate; however other methods of identifying sibling pixels have been put forward, e.g. SqueeSAR (Ferretti et al., 2011) and NL-InSAR (Deledalle et al., 2014). There may be advantages to other methods of sibling calculation that are worth exploring. For example, NL-InSAR calculates siblings from a single SAR image. This would remove the need for a long time-series of pre-seismic imagery, which may not always be available, and would decrease the number of SAR images to be processed and stored. However, RapidSAR has several attributes that make it particularly well suited to this study. First, it is fully automated and its intended purpose of volcano monitoring means that it was designed to process imagery rapidly, making it suitable for my purpose of emergency response. Second, it allows additional SAR scenes to be incorporated as they are acquired. Third, unlike SqueeSAR, RapidSAR does not require sibling pixels to be interconnected. This allows siblings to be more dispersed through the search window, so that siblings of a landslide pixel are less likely to lie within the landslide.

3.4.7 Application

The data required for the production of the classification surfaces described in this study are available globally, albeit with varying temporal coverage. Two datasets are required: the SAR imagery and the DEM used to process it. The SRTM 1-arcsecond DEM used here is a global product available between 60° North and

56° South and is openly distributed (Farr et al., 2007). SAR imagery is available from a variety of platforms but here I use Sentinel-1 imagery which is acquired at regular intervals globally and is also openly distributed. The classification surfaces produced in this study could therefore be produced in most locations across the world following a landslide trigger event.

It has been stressed in multiple studies that the speed at which information can be produced and disseminated is vital to its application (Fiedrich et al., 2000; Williams et al., 2018). The applicability of SAR-derived landslide products in emergency response is therefore largely determined by the time taken to produce them. The ARIA team have demonstrated that damage proxy maps can be generated within 1 day of post-event imagery being acquired. Although the new method I present here requires more SAR data to be processed, the majority of the processing steps can be performed while waiting for the initial post-event image to be acquired. Preparation of the DEM, downloading pre-event SAR imagery, processing this to obtain interferograms and calculating sibling locations can all be performed without the post-event image. Once this image has been acquired, the final steps could be carried out within 1 day: downloading and processing the post-event image, calculating boxcar and sibling-based co-event coherences and differencing these. Less time may be required for landslide events that affect a smaller region than the 2015 Gorkha earthquake.

Exactly when these classifiers could be produced is therefore dependent on the acquisition of SAR imagery. The post-event image used in this study was acquired on day 4 following the mainshock, meaning that a classification surface could have been produced by day 5. However, as is shown on Figure 3.1, imagery further east of Kathmandu was not acquired until day 10, meaning that it would have taken 11 days to form a complete classification surface for the affected area. Ascending data on track S085a were acquired 7 days following the mainshock and cover the entire affected area so that classification surfaces from these data could have been produced within 8 days. The frequency at which areas are imaged in SAR varies depending on location globally. The launch of Sentinel-1b in 2016 means that Sentinel imagery is now acquired with a 6- rather than 12-day revisit time across Europe (ESA, 2019). These data are freely accessible soon after acquisition. Other satellite constellations, such as ALOS-2 or Cosmo-Skymed may also provide imagery of affected areas.

Possible uses for a SAR based map of relative landslide density can be illustrated using the case of the Nepal earthquake. Williams et al. (2018) divide the emergency response into several phases each with different information requirements. In the first 3 days the 'situational analysis' phase aimed to identify, at a broad scale,

the spatial extent and severity of the damage. It is conceivable for SAR products to be produced within this time window, although this would depend on the wait time for post-event imagery. After this 3-day period, the requirements of disaster managers begin to transition to more detailed information on specific areas of concern (Williams et al., 2018). Based on my findings here, SAR-coherence methods alone would not be capable of mapping individual landslides but could still direct managers toward the areas that were most badly affected – especially if aggregated landslide density maps could be combined with pre-existing population data.

The Gorkha earthquake occurred at the end of April, meaning that the onset of the monsoon was expected around 2 months later. Since earthquake-triggered landsliding correlates spatially with areas of ground weakened by shaking and since existing landslide deposits may be remobilised as debris flows, causing more damage, earthquake-triggered landslide maps were used as input for predictive monsoon-triggered landslide hazard maps (Datta et al., 2018). A landscape-scale landslide density map could have been used in this process and would have the advantage of being homogeneous, the whole area having been imaged by a single satellite.

Finally, landslide density could be used in directing field investigations such as those carried out by Collins and Jibson (2015), who targeted sites of potential landslide dams. Since landslide mapping was incomplete when they began their investigation, it was necessary to add target sites while the investigations were ongoing. The initial list of target sites was determined at the start of their field investigation, 32 days after the Gorkha mainshock, meaning that SAR products could easily have been made available during this time.

Although here I have focussed on earthquake-triggered landslides, SAR-based approaches have as much or more potential in identifying monsoon- or typhoon-triggered landslides. Since rainfall events are generally accompanied by cloudy weather conditions which obstruct optical mapping, a SAR-based classifier could be particularly advantageous. The ARIA team have released damage proxy maps for urban damage following typhoons in the USA, Tonga and Puerto Rico (NASA, 2018). There are various factors, however, which could complicate the use of SAR products in mapping rainfall-triggered landslides. In the case of typhoons, one such complication would be the damage to vegetation caused by the typhoon, which would be likely to decrease coherence, possibly leading to false positives. SAR coherence methods may prove unable to distinguish between landslides and damaged vegetation, although combination with SAR amplitude or other predictors might ameliorate this. Monsoon-triggered landslides represent a different problem: since the trigger extends over several months, pairs of SAR images would contain both old and new landslides as well as reactivated or partially reactivated old landslides.

The signals associated with each of these would be different, which might cause confusion, particularly if aggregating pixels containing several landslides triggered at different times. Landslides which pre-date a SAR image pair and are stable would be expected to have a higher coherence than new landslides and possibly higher than the surrounding vegetation.

3.5 Conclusions

In this Chapter, I have tested three potential SAR-coherence-based landslide classification methods at a range of resolutions against a manually mapped landslide inventory for events triggered by the 2015 Gorkha, Nepal earthquake (Roback et al., 2018). I have tested two classifiers that have previously been suggested to contain landslide information: absolute coherence and the ARIA method for urban damage proxy mapping. I have also presented a new method for landslide classification, in which the difference between boxcar and sibling-based coherence (Bx-S) is used as a classifier. Using ROC analysis, I showed that none of the methods tested here were able to identify landslides at a pixel-by-pixel (20 m × 22 m) scale. However, all three classifiers were more successful when the resolution was coarsened by aggregating pixels, which corresponds to the real-world application of classifying larger regions of high landslide density. The Bx-S method presented in this chapter is more successful than existing SAR coherence methods, with an AUC value of 0.77 for 300 m × 330 m aggregate pixels. This suggests that the Bx-S method may be able to provide useful and timely information on the large-scale distribution of landslides following future triggering events, such as earthquakes, even under heavy cloud conditions that limit the applicability of optical satellites for this purpose.

A Systematic Study of SAR Coherence Landslide Detection Methods Across Event and Sensor Type

Chapter Overview

In Chapter 3, I presented a new method of landslide detection using SAR and demonstrated its performance using Sentinel-1 data of the 2015 Gorkha earthquake. This use of a single SAR dataset and case study event is commonplace (e.g. Aimaiti et al., 2019; Jung and Yun, 2019; Konishi and Suga, 2018, 2019; Yun et al., 2015, and Chapter), but it does not allow for comparison between methods for different SAR datasets and events. If SAR coherence methods are to be applied in future events, we need to know whether they work equally well across different event and sensor type, and if not, which method should be applied in the case where different SAR data is available. To address this lack of systematic testing, I test five SAR-coherence-based methods using data from Sentinel-1 and ALOS-2 across landslides triggered by four earthquakes.

The work presented in this chapter is currently in review in the journal Natural Hazards and Earth System Science and is available online as a discussion paper (Burrows et al., 2020). For the most part, the discussion paper has been reproduced here verbatim, with some small changes made to the text in order to improve the coherence of the thesis as a whole. Text and figures used in this chapter are reproduced from the discussion paper under a creative commons licence.

4.1 Introduction

Information on the spatial distribution of earthquake- or rainfall-triggered landslides needs to be generated as quickly as possible in order to be useful for emergency response efforts, ideally with two weeks of an event (Inter-Agency Standing Committee, 2015; Williams et al., 2018). This information is commonly generated from analysis of optical satellite imagery (e.g., Bessette-Kirton et al., 2019; Kargel et al., 2016). However, relying solely on optical satellite imagery in landslide assessment is problematic, as the mapping process can be significantly delayed by cloud cover (Robinson et al., 2019). When optical imagery is not available, empirical models based on factors such as the topographic slope and measurements or predictions of earthquake-induced shaking or rainfall data are used to predict the likely location and intensity of triggered landsliding (e.g. Kirschbaum and Stanley, 2018; Kritikos et al., 2015; Nowicki Jessee et al., 2018). However, while these can be generated within hours of an earthquake or rainfall event, they do not always perform well (Allstadt et al., 2018; Ferrario, 2019), and can only give a static prediction of landsliding, which in reality may evolve through time.

SAR satellite imagery presents an alternative method of generating landslide information in all weather conditions as radar is able to penetrate cloud. For landslide studies, SAR is most commonly used to measure the downslope velocity of slow-moving landslides (e.g. Aslan et al., 2020; Bekaert et al., 2020; Bonì et al., 2018; Dai et al., 2016; Handwerger et al., 2019; Hu et al., 2019; Reyes-Carmona et al., 2020; Solari et al., 2020). However, SAR can also be used to detect modifications to the Earth's surface and it has been demonstrated that radar methods can be used to automatically detect wind damage to forests (Rüetschi et al., 2019), flooding (Martinis et al., 2015) and urban damage following earthquakes, typhoons and wildfires (NASA, 2018; Yun et al., 2015).

Recently, there have been several attempts to develop similar SAR-based change detection methods for rapid landslide mapping, based on SAR amplitude (Konishi and Suga, 2018, 2019; Mondini et al., 2019), coherence (Chapter 3 of this thesis; Olen and Bookhagen, 2018; Yun et al., 2015), or some combination of these (Aimaiti et al., 2019; Ge et al., 2019; Jung and Yun, 2019), or based on polarimetric SAR methods (e.g. Yamaguchi et al., 2019). However, with the exception of Mondini et al. (2019) who used a global selection of landslides, these studies are generally tested on a single landslide event and use a single radar sensor. For example, Aimaiti et al. (2019); Ge et al. (2019); Konishi and Suga (2019); Jung and Yun (2019); Yamaguchi et al. (2019) tested their methods using ALOS-2 imagery of the M_w 6.6 2018 Hokkaido earthquake. If such methods are to be applied in future

events, wider testing is needed. This would allow us to establish whether different methods work equally well for different events, and to determine the best method to use with data from a given SAR sensor and within a given time window.

To address this need, I present in this chapter a systematic statistical comparison of the performance of five radar-based methods of landslide detection, using imagery acquired by the Sentinel-1 and ALOS-2 PALSAR-2 sensors spanning four case study landslide-triggering earthquakes. I chose to test on earthquakes rather than rainfall events for two reasons. First, it can be assumed that the majority of landslides occurred concurrently with or very shortly after the shaking, and this information on landslide timing simplified the validation of the methods. Second, radar imagery is more likely to be acquired immediately after an earthquake as part of emergency tasking of satellite acquisitions, as these data are commonly used to measure earthquake-related ground deformation. I tested on four large ($M_w > 6.6$) events: the 2015 Gorkha, Nepal earthquake, the 2018 Hokkaido, Japan earthquake, and two earthquakes of the 2018 Lombok, Indonesia sequence (Figure. 4.1). All of these events triggered thousands of landslides, which have been mapped using optical satellite imagery (Ferrario, 2019; Roback et al., 2018; Zhang et al., 2019). I assessed the ability of each method and radar dataset to predict these validation data, and demonstrate the wide applicability of SAR coherence methods to landslide detection, making recommendations for which method is most suitable depending on the type of SAR data that is available and the timing of data acquisition.

The theory behind SAR interferometry and coherence is described in Chapter 2. A SAR system works by illuminating the Earth's surface with microwave radiation and measuring the amplitude and phase of the returned signal. In the InSAR technique, the difference in phase between two images acquired over the same area at different times can be used to map the change in distance between the ground and the satellite. SAR amplitude is the strength of the backscattered signal and is partially dependent on the material at the ground surface: its orientation relative to the satellite, its roughness, and its dielectric properties. SAR coherence γ is estimated as a measure of signal quality at each pixel from the similarity between two SAR images in amplitude and phase difference for a small ensemble of n according to Equation 2.13 (reproduced from Chapter 2).

$$|\gamma| = \frac{\frac{1}{n}\sum_{i=1}^{n} A_i \overline{B_i}}{\sqrt{\frac{1}{n}\left(\sum_{i=1}^{n}|A_i|^2 \sum_{i=1}^{n}|B_i|^2\right)}}$$

A_i and B_i are complex representations of the phase and amplitude of each pixel i within the ensemble, with the complex conjugate shown by the overline. The
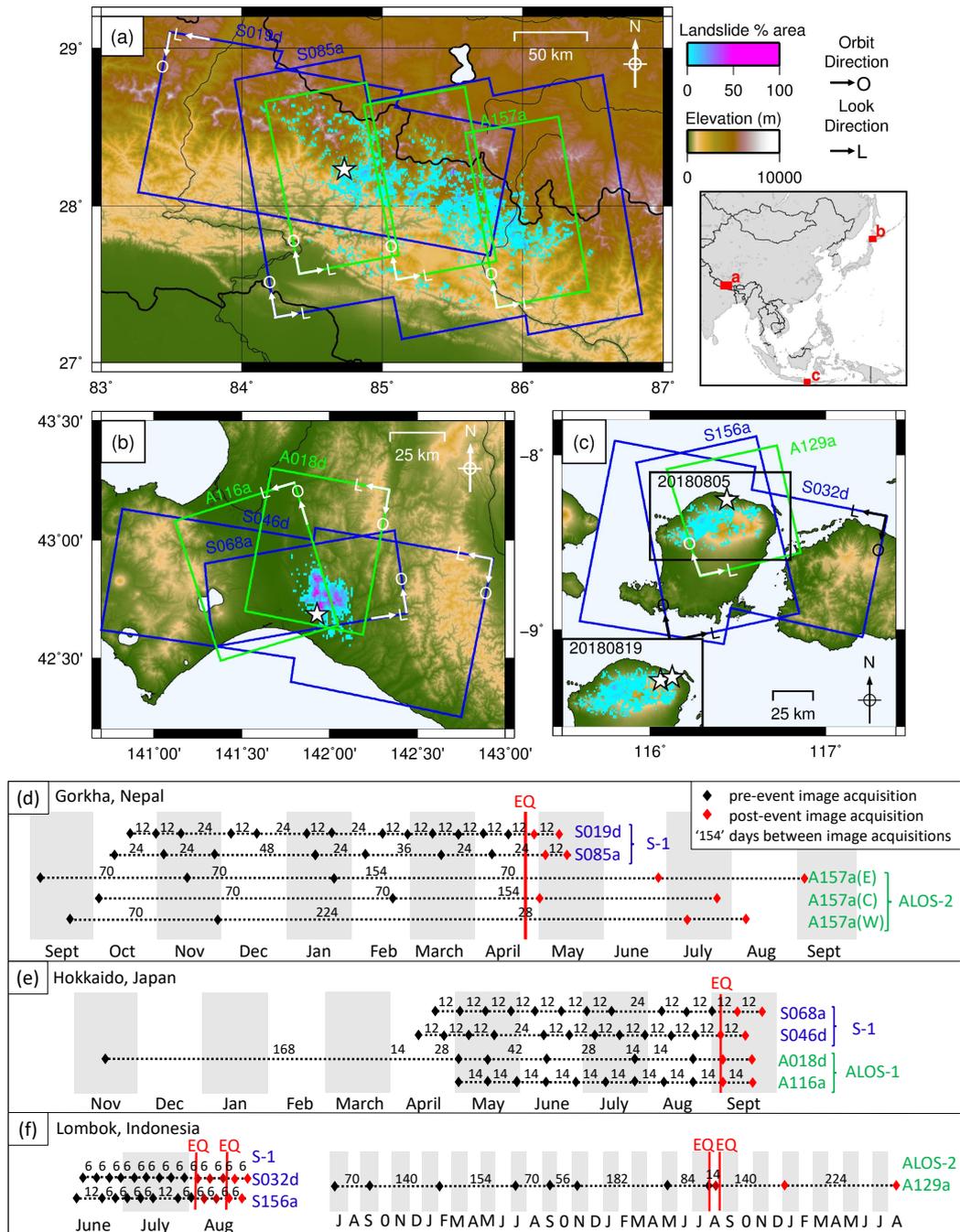
Figure 4.1: (a, b, c) Landslides triggered by the 2015 Gorkha, Nepal earthquake, the 2018 Hokkaido, Japan earthquake, and the 2018 Lombok, Indonesia earthquakes, respectively, plotted as the areal density of landsliding based on 1 km^2 cells (Roback et al., 2018; Zhang et al., 2019; Ferrario, 2019). ALOS-2 SAR acquisitions are shown in green and Sentinel-1 in blue. Landslides mapped at the end of the Lombok earthquake sequence (Lombok-2) are inset in (c) (Ferrario, 2019). (d, e, f) Acquisition dates and track numbers of SAR imagery used in this study. Earthquakes are shown as red vertical lines, black symbols show pre-event image acquisition dates, and red symbols show post-event dates.

conventional method of selecting the pixels used in this ensemble is a 'boxcar' method, in which a small rectangular ensemble of pixels immediately adjacent to and centred on the target pixel are used (e.g. Hanssen, 2001; Yun et al., 2015). Alternatively, a 'sibling' method (e.g. Spaans and Hooper, 2016) can be used where the ensemble of pixels is selected from within a wider window.

Coherence can be decomposed into 3 components, with the total coherence dependent on their product (Equation 2.14, Zebker and Villasenor, 1992):

$$\gamma_{total} = \gamma_{temporal} \cdot \gamma_{spatial} \cdot \gamma_{thermal}$$

Here we are interested in temporal coherence $\gamma_{temporal}$, as decorrelation of this component reflects changes in the physical properties of the Earth's surface between image acquisition. The spatial coherence, $\gamma_{spatial}$, is dependent on the geometric properties of the satellite acquiring the image and the ground surface. Decorrelation of the spatial component of coherence $\gamma_{spatial}$ is the result of small changes in satellite viewing geometry between acquisitions and can be stronger in areas of steep topography, as it is dependent on incidence angle. When the perpendicular baseline of the SAR image pair used to form an interferogram is sufficiently small, this spatial component will be small compared to any temporal decorrelation (Zebker and Villasenor, 1992). I removed distorted pixels, which were likely to be more strongly affected by decorrelation of $\gamma_{spatial}$, from my analysis in section 4.2.4. Decorrelation of the thermal coherence $\gamma_{thermal}$ was assumed to be insignificant, following Zebker and Villasenor (1992).

4.2 Data and methods

4.2.1 SAR data

In this study, radar imagery was used from two satellite systems. Sentinel-1 uses C-band radar (wavelength ~ 5.6 cm), whilst ALOS-2 PALSAR-2 uses lower frequency L-band radar (wavelength ~ 24 cm). The difference in wavelength between the two systems means that, in forested areas, L-band radar penetrates further into the canopy than C-band. The shorter wavelength of C-band radar means it is sensitive to surface modifications on a smaller spatial scale. For example, in a forest, C-band radar data may detect change in the location or orientation of leaves, while L-band is sensitive instead to changes in the location and orientation of branches. L-band InSAR is often more useful in vegetated areas, as its deeper penetration allows it to retain higher coherence in the absence of major vegetation changes.

Radar systems acquire data at an oblique angle to the vertical on near-polar ascending and descending orbital tracks (referred to here as a and d), which are acquired on different dates. The satellite look direction is perpendicular to the orbit direction. The data used in this study were acquired at an angle of between 31.4° and 43.8° to vertical. This oblique acquisition angle means that on a given track, some hillsides will be more favourably oriented to the sensor than others, and thus information from ascending and descending tracks together can give complete coverage of an event. As it is impossible to directly combine data from both tracks, and in some cases imagery will only be acquired on one track within two weeks of an event, here I considered each track separately.

4.2.2 Case studies

I used four case study events: the 2015 M_w 7.8 Gorkha, Nepal earthquake (Figure 4.1a, d); the M_w 6.6 2018 Hokkaido, Japan earthquake (Figure 4.1b, e); and two M_w 6.8 and 6.9 earthquakes from the 2018 Lombok, Indonesia sequence (Figure 4.1c, f). These four events have several traits in common which made them suitable for this study. First, they were all large earthquakes, triggering thousands of landslides, making them of interest from an emergency response perspective. This also meant that the earthquakes and associated landslides had previously been investigated, and inventories of triggered landslides had been compiled from optical satellite imagery (Ferrario, 2019; Roback et al., 2018; Zhang et al., 2019), enabling direct testing of the radar methods against these independent datasets. Second, while the vegetation types differ between the three regions, the presence of dense vegetation across each region meant that landslide and non-landslide pixels could be expected to have a similar first-order signal in the radar data across the events. Third, ascending and descending track Sentinel-1 data and at least one track of high resolution ALOS-2 data were available for all case study areas.

The M_w 7.8 2015 Gorkha, Nepal earthquake (Figure 4.1a) occurred on 25 April 2015 and triggered around 25,000 landslides over an area hundreds of kilometres wide, as mapped by Roback et al. (2018). Sentinel-1 imagery was acquired on tracks S019d and S085a. ALOS-2 data on track A157a were divided into subtracks with acquisitions on different dates, shown as separate polygons on Figure 4.1a, which will be referred to as East (E), Central (C) and West (W).

The M_w 6.6 2018 Hokkaido, Japan earthquake (Figure 4.1b) occurred on 5 September 2018. Two inventories have been published for this event: one containing 7,837 landslides (Wang et al., 2019) and one containing 5,265 (Zhang et al., 2019). Neither provided information on the mapping extent so I assumed that this could

be approximated by the convex hull of the data locations. As the inventory of Zhang et al. (2019) has the largest convex hull, I used this inventory for validation of the radar methods. Both descending and ascending ALOS-2 data were available for this event, with a higher spatial and temporal frequency than for the other events. The earthquake occurred the day after Typhoon Jebi passed over Hokkaido, and so this case study was also an opportunity to test landslide detection methods following a rainfall event, with the advantage that because the typhoon and earthquake occurred one day apart, and aerial imagery of the triggered landslides was acquired immediately afterwards, we know more more precisely when they occurred (Yamagishi and Yamazaki, 2018). This is important if SAR methods are to be used in the future for mapping storm-triggered landslides because factors such as wind damage and the water content of the soil are known to affect SAR coherence and amplitude (Rüetschi et al., 2019; Scott et al., 2017).

The 2018 Lombok earthquake sequence comprised 4 earthquakes with $M_w > 6$: M_w 6.4 on 28 July; M_w 6.8 on 5 August; and M_w 6.3 and 6.9 on 19 August. Ferrario (2019) generated two landslide inventories for this sequence. Although cloud-free imagery was not available across the whole affected area following the earthquake on 28 July, no landslides were visible in the areas that could be mapped. Ferrario (2019) thus presented their first inventory of 4,823 landslides triggered following the 5 August earthquake, and a second inventory of 9,319 landslides that had been triggered by the end of the sequence. I refer to the 5 August inventory as Lombok-1 (Figure 4.1c) and the 19 August inventory as Lombok-2 (Figure 4.1c, inset).

There are several key ways in which the events differed. First, the triggered landslides had very different spatial patterns, with the Gorkha earthquake triggering landslides across an area spanning hundreds of km, while the Lombok and Hokkaido earthquakes triggered landslides across only a few km. It can be seen in Figure 4.1 that much denser landsliding was triggered by the Hokkaido earthquake than by the other events. Second, the sizes and shapes of the landslides were very different between events: the Lombok earthquakes triggered a large number of small landslides with a median landslide area of 460 m^2 for Lombok-1 and 580 m^2 for Lombok-2, compared to equivalent median areas of 4,350 m^2 for Hokkaido and 1,070 m^2 for Nepal (measured from the inventories of Ferrario, 2019; Roback et al., 2018; Zhang et al., 2019). Third, the events occurred under different weather conditions: the Hokkaido earthquake followed months of heavy rain and occurred one day after Typhoon Jebi, while the Gorkha and Lombok earthquakes occurred during the dry season. Finally, the topographic relief in the three case study areas varied significantly. In Nepal the majority of landslides occurred on slopes of over 40° (Roback et al., 2018). For the Hokkaido event, the proportion of slopes > 40°

was very low and so the majority of landslides occurred on much shallower slopes (Wang et al., 2019), with Lombok lying between these two extremes. This is highly relevant to the application of SAR coherence methods to landslide detection. Steep slopes can lead to distortion of the radar image, and coherence is also dependent on the geometry of the hillslope and radar sensor. Therefore, we might expect that, as hillslopes in Hokkaido and Lombok are shallower than in Nepal, landslide detection using SAR may be more successful in these areas. These differences between the four events made them ideal for testing the wider applicability of SAR-coherence-based landslide detection methods in vegetated areas. If a method is to be widely applied in the future, we need to be confident that its performance is consistent across differing events and settings.

4.2.3 Landslide detection methods

I test two existing methods: the ARIA method of Yun et al. (2015) and the boxcar-sibling method presented in Chapter 3. Each of these existing methods uses a single post-event SAR image. I also present and test three new methods that incorporate a second post-event image: the post-event coherence increase (PECI); the sum of the coherence increase and decrease (ΔC_sum); and the maximum of coherence increase or decrease (ΔC_max).

4.2.3.1 The ARIA method (ARIA)

This method was developed by the NASA ARIA project for use in urban damage mapping and identifies 'damaged' pixels as those where coherence has decreased in the co-event map relative to the pre-event map. Figure 3.4 in Chapter 3 describes the process behind this method. First the pre-event coherence map is adjusted so that it has the same coherence frequency distribution as the co-event coherence map using exact histogram matching (Coltuc et al., 2006). The pre-event surface is then subtracted from the co-event surface (Yun et al., 2015). Although this method was developed for detecting damage to buildings, Yun et al. (2015) tested it on the 2015 Gorkha earthquake and noted that landslides in the Langtang Valley corresponded spatially to areas of coherence decrease in the ARIA surface. Coherence decrease between pre-event and co-event interferograms has since been used as an input in the landslide detection methods of Aimaiti et al. (2019) and Jung and Yun (2019) applied to the 2018 Hokkaido earthquake.

4.2.3.2   The boxcar-sibling method (Bx-S)

Rather than relying on the coherence change through time, the Bx-S method, which I presented in Chapter 3, uses the difference between two alternative co-event spatial methods of coherence calculation as a landslide classification surface. The four other methods tested here all use a traditional 'boxcar' coherence, in which the coherence of a pixel is estimated from the similarity in phase change of the pixels immediately adjacent to it. When a sibling-based method such as that of Spaans and Hooper (2016) is used to estimate coherence, the coherence of a pixel becomes dependent on 'siblings' that are not immediately adjacent to it but that are expected to behave similarly. For a landslide pixel, this means that its coherence is calculated from a more dispersed ensemble of pixels than with a traditional boxcar coherence estimate and so proportionally less of the ensemble will also lie within the landslide (Figure 3.5). A sibling-based coherence surface is therefore relatively insensitive to landslides, and landslides can be identified as those whose co-event boxcar coherence is lower than their co-event sibling coherence.

4.2.3.3   Post-event coherence increase (PECI)

The coherence decrease caused in a co-event interferogram by a landslide is a temporary effect, assuming that the landslide stops moving following the earthquake. This behaviour has been observed for a large landslide triggered by the 2017 M_w 7.3 Iran earthquake (Goorabi, 2019). Therefore in a post-event interferogram (calculated from two post-event images) coherence should be higher for landslide pixels than in a co-event interferogram. As landslides expose bare rock or soil, which is likely to have higher coherence than vegetated areas, this co-event to post-event increase may actually be larger than the pre-event to co-event decrease used in the ARIA method to measure landslides, making the signal easier to detect. This is particularly the case when using C-band SAR, which experiences more decorrelation than L-band in vegetated regions. Applying the same histogram-matching step as in the ARIA method, I propose this co-event to post-event coherence increase as a new potential landslide detection method.

4.2.3.4   Sum of coherence increase and decrease (ΔC_sum)

As landslides are expected to exhibit both a decrease in co-event coherence and an increase in post-event coherence, I summed the absolute magnitudes of these changes to form a new landslide classification surface. As in the ARIA method, the pre-event and post-event coherence maps were histogram-matched to the co-event

coherence map, removing bulk changes in coherence between the three maps. This method is equivalent to ARIA + PECI.

4.2.3.5 Maximum of coherence increase or decrease (∆C_max)

For every pixel, I took whichever was largest of the pre-event to co-event decrease (ARIA) and the co-event to post-event increase (PECI). This method is similar to the ΔC_sum method but uses whichever has the strongest signal. The relative signal strength of the ARIA or PECI methods will vary by location, for example according to the vegetation type. This method takes whichever of the two methods has a stronger signal for any given location.

4.2.4 Data processing

SAR data were processed using GAMMA, with the LiCSAR processing software used for Sentinel-1 (Lazeckỳ et al., 2020). The data were multilooked by a factor of 5 in range and 1 in azimuth (Sentinel-1) and by 5 in both range and azimuth (ALOS-2) to improve the signal to noise ratio. See Table 4.1 for information on the data resolution and pixel size at various stages of the processing. For geometric coregistration, I used the 1-arcsecond SRTM DEM (Farr et al., 2007).

The boxcar coherence estimate used in all methods was calculated using a 3×3 pixel moving window (Table 4.1). The sibling-based coherence estimate used for the Bx-S method was calculated using the RapidSAR algorithm of Spaans and Hooper (2016). Siblings were calculated based on all pre-event images shown in Figure 4.1 (a minimum of 6 images). For every pixel, between 15 and 50 siblings were identified within an 81×81 pixel window based on their amplitude and amplitude variability (window sizes in Table 4.1). Unfortunately, insufficient pre-event ALOS-

Table 4.1: The resolution and pixel spacing of the data at different stages throughout the processing for Sentinel-1, ALOS-2 on tracks A018d and A116a (Hokkaido), track A157a (Nepal) and track A129a (Lombok). Resolutions are given in Range x Azimuth coordinate system

	Resolution (m)	Radar pixel spacing (m)	Multilooked radar pixel spacing (m)	Boxcar window size (m)	Sibling search window size (m)
All Sentinel-1	20×22	2.3×14.0	11.6×14.0	34.8×42.0	940×1134
ALOS-2 018d	3×3	1.4×2.1	7.2×10.6	21.6×31.8	583×859
ALOS-2 116a	3 x 3	1.4 x 1.9	7.2 x 9.3	21.6 27.9	583 x 753
ALOS-2 157a	10 x 10	4.3 x 3.8	21.5 x 19	64.5 57.0	1742 x 1539
ALOS-2 129a	10 x 10	4.3 x 3.3	21.5 x 16.3	64.5 x 48.9	1742 x 1320

2 data were available to carry out this calculation in the case of the 2015 Gorkha, earthquake and so the Bx-S method could not be tested for this case.

In most cases, I used the co-event, pre-event, and post-event coherences with the shortest temporal baseline; however for the inventory provided by Ferrario (2019) for the landslides triggered by the Lombok earthquake on 19 August, I used a co-event image that spans this earthquake and the 5 August earthquake, as the landslide inventory contains landslides triggered by both events. After calculating each landslide classification surface from the methods described in section 4.2.3, I used the GAMMA software to convert the surfaces to a geographic coordinate system. This process, involving reprojection and interpolation, results in uniform pixel size (20 m × 22 m). I then normalised the values of each surface by the theoretical maximum and minimum value that could be obtained from each method, resulting in a set of classification surfaces with values between 0 and 1, with 1 most likely to be a landslide.

Before statistical testing, I removed distorted pixels. The oblique angle at which SAR imagery is acquired meant that some pixels were distorted by topography and were badly imaged by the SAR system, experiencing shadow, foreshortening, or layover (Franceschetti et al., 1994) and decorrelation of $\gamma_{spatial}$ (Section 4.2.1). As in Section 3.2.2.4, I masked these according to the area in geographic coordinates that contributes to the pixel in radar geometry, removing pixels with an area of 0 and those where this area was over six times larger than their multilooked pixel spacing in radar coordinates (see Table 4.1).

I carried out statistical testing of the results at two resolutions: first, at the initial resolution of the processed radar data in geographical coordinates (20 m × 22 m), with the vector landslide inventories of Ferrario (2019); Roback et al. (2018); Zhang et al. (2019) rasterized at this resolution; and second, at an aggregated resolution of 200 m × 220 m, calculated by amalgamating 10 × 10 grids of the 20 m × 22 m pixels. As in Chapter 3, aggregated classifier pixels were given the mean value of the unmasked pixels in the 10 × 10 grid. If over 95% of an aggregate pixel is made up of masked pixels, the aggregate pixel was masked. I did not attempt to map SAR classification surface values directly to landslide areal density values, as this has not been attempted previously and may not be possible. Thus a binary ground truth was preferable, which I generated by assigning aggregate pixels as 'landslide' if they were composed of over 25% landslide by area according to the rasterized landslide inventories I used for verification. The aggregation process was done for several reasons. First, the boxcar coherence estimation has the effect of blurring neighbouring pixels, so that the minimum size of an object that could be resolved was dependent on the size of the 3 × 3 boxcar (see Table 4.1). In all cases

this was larger than the 20 m × 22 m pixel spacing in geographic coordinates. Second, I found in Chapter 3 that SAR coherence methods performed better at lower resolutions. Third, when comparing landslide inventories, for example those of Zhang et al. (2019) and Wang et al. (2019) for the Hokkaido earthquake, there is often some variation in the exact shape and location of individual polygons. This effect is decreased when inventories are downsampled. This aggregation process is the same as that described in Chapter 3, and the effect that the choice of grid size and landslide % area threshold were explored in that Chapter. Here, I chose a resolution that was larger than the boxcar window but that resulted in enough mapped landslide and non-landslide aggregate pixels for analysis. This is similar to the resolution of other landslide products generated for emergency response (e.g. Bessette-Kirton et al., 2019; Nowicki Jessee et al., 2018).

4.2.5   ROC analysis

I used ROC AUC values to evaluate and compare the classification ability of each surface. For each classification surface, a threshold was set for which no pixels were classified as landslides and then incrementally decreased until it reached a value where all pixels were classified as landslides. At each incremental threshold, the false positive rate (the ratio of false positives to real non-landslide pixels) was plotted against the true positive rate (the ratio of true positives to real landslide pixels) to form an ROC curve. The area under this curve is equal to the probability that if a landslide pixel and a non-landslide pixel were randomly selected from the dataset, the classifier would rank them correctly (Hanley and McNeil, 1982). For a randomly generated surface with no classification ability, the AUC = 0.5. For a perfect classifier, the AUC = 1.0. The implications of the use of ROC AUC in assessing classifier performance are discussed in Section 3.2.2.3.

4.3   Results

4.3.1   Results at 200 m × 220 m resolution

Figure 4.2 shows the ROC AUC values for each classification method described in section 4.2.3 and each track of radar data shown in Figure 4.1. The cells are coloured so that the best performing classification surfaces are shown in green and the weakest in red. A classifier that performs well for all events and both sensors should therefore appear as a green row. The eastern and western tracks of S157a and data for Lombok-2 on track A129a have been omitted, as the waiting times for

(a)	Event	Hokkaido				Nepal			Lombok-1			Lombok-2	
	Satellite	S-1		A-2		S-1		A-2	S-1		A-2	S-1	
	Track no.	068a	046d	116a	018d	085a	019d	157a	156a	32a	129a	156a	032d
1 post-event image	ARIA	0.52	0.57	0.70	0.89	0.59	0.69	0.81	0.64	0.56	0.88	0.49	0.45
	Bx-S	0.59	0.58	0.52	0.44	0.66	0.74	-	0.64	0.55	0.68	0.67	0.60
	Waiting time (days)	8	0	1	1	8	4	7	3	0	13	1	4
2 post-event images	PECI	0.79	0.78	0.66	0.80	0.66	0.68	0.81	0.64	0.69	0.93	0.68	0.68
	ΔC_sum	0.73	0.73	0.70	0.88	0.66	0.71	0.88	0.71	0.62	0.92	0.63	0.57
	ΔC_max	0.74	0.75	0.64	0.89	0.62	0.71	0.85	0.72	0.62	0.92	0.65	0.59
	Waiting time (days)	20	12	15	15	20	16	91	9	6	153	7	10

Figure 4.2: (a) AUC values for each classifier described in section 4.2.3 at a resolution of 200 m × 220 m. For Hokkaido, I used the inventory of Zhang et al. (2019). Insufficient pre-event data were available on A157a to calculate the Bx-S classification surface. Colours range from red (worst performing AUC < 0.55) to green (best performing, AUC >0.80). (b, c, d) Examples of ROC curves for (b) the ARIA method on track S156a, Hokkaido; (c) the Bx-S method on track S156a, Lombok-2; (d) ΔC_max on track A157a, Nepal.

the first post-event image were very long (77, 63 and 139 days respectively). This long time window resulted in widespread co-event coherence loss that adversely affected classifier performance. Such a long waiting time would make it extremely unlikely that these data could be used in emergency response and the poor performance is unlikely to be representative of classifier behaviour when using more timely imagery.

The methods are grouped by the number of post-event images that are required, and the waiting time in days for this imagery for each event and SAR track is also given. As the primary scientific use for post-seismic ALOS-2 imagery is to form a co-event interferogram, only one post-event image was acquired immediately following the Lombok-1 and Nepal earthquakes, with the waiting time for the second post-event image being considerably longer. I still include these results as the waiting time for L-band radar data is likely to decrease in the future with the
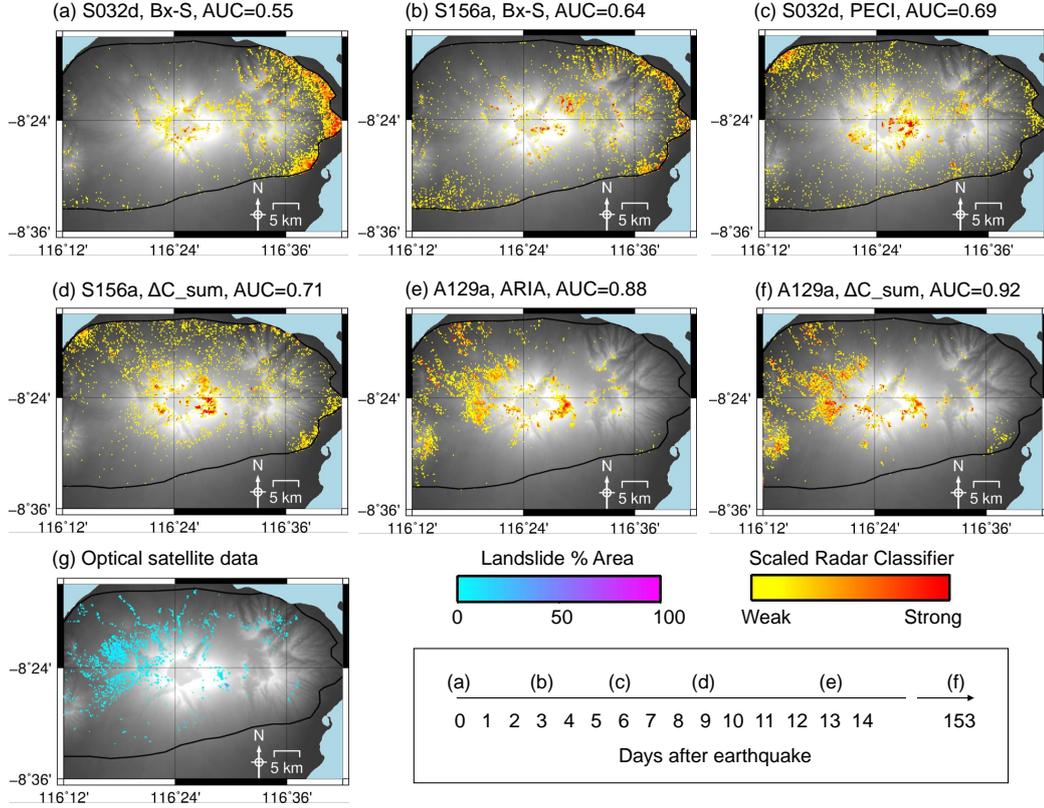
Figure 4.3: (a-f) Time series of classification surfaces in the order that SAR data were acquired on tracks S032d, S156a and A129a following the 5 August 2018 Lombok earthquake, using the methods I recommend in section 4.3.1.(g) Observed Landslide areal density for 200 m x 220 m pixels (calculated from Ferrario, 2019).

planned NASA/ISRO NiSAR satellite constellation, which is expected to launch in 2022, acquiring data globally with a 12 day repeat time (Sharma, 2019).

If only data acquired within the two week emergency response window is considered (Inter-Agency Standing Committee, 2015), the highest AUC in Hokkaido was initially 0.58 on day 0 using the Bx-S method on S046d, rising to 0.89 after 1 day with data from track A018d and the ARIA method. In Nepal, the first radar data were acquired on day 4 on track S019d, from which the highest AUC of 0.74 was obtained using the Bx-S method. On day 7, the first ALOS-2 image was acquired on A157a, and more accurate information could have been generated using the ARIA method (AUC 0.81), although this ALOS-2 scene covers a smaller area than the Sentinel-1 data (Figure 4.1). In Lombok, the 6-day Sentinel-1 acquisition window meant that a large volume of data was available within two weeks of these events. The best data and method for Lombok-1 evolved as follows: ARIA, S032d (day 0, AUC 0.56); ARIA or Bx-S, S156a (day 3, AUC 0.64); PECI, S032d (day 6, AUC 0.69); ΔC_max, S156a (day 9, AUC 0.72); ARIA, A129a (day 13, AUC 0.88). The

corresponding classification surfaces for this evolution are plotted in Fig. 4.3. For Lombok-2, the first Sentinel-1 image was acquired on day 1, track S156a, and had an AUC of 0.67 using the Bx-S method, which could be slightly improved upon using the second post-event image that was acquired on day 7, using PECI (AUC 0.68). No ALOS-2 data was available within 2 weeks of this earthquake. Therefore in most cases, initially only Sentinel-1 data are available and the best option is the Bx-S method. This can then be improved upon when the first ALOS-2 image becomes available using the ARIA method. For Lombok-1 and Lombok-2, where two post-seismic Sentinel-1 images became available before the first ALOS-2 image, incorporating these data also improved on the accuracy of the result.

With a single L-band post-event image, the ARIA method was the best-performing landslide classification surface in all cases. An improvement was seen when an additional post-event image was acquired and methods requiring this image were used for the case of Lombok and Nepal but not for Hokkaido. When a single C-band post-event image was used, the Bx-S method outperformed ARIA for Hokkaido, Gorkha and Lombok-2 and had a similar performance for Lombok-1. The addition of a second post-event image and adoption of methods that used this image showed an improvement in Hokkaido and Lombok-1, but not in Nepal. However, when considering Figure 4.2a as a whole, methods that used a second post-event image were both better performing and more consistent across event and sensor type. When looking across all three events, the best option in terms of AUC was to use the ΔC_sum method with L-band imagery. When grouped by event and radar look direction and ranked according to AUC, Δ C_sum using ALOS-2 was ranked 3rd out of 10 classification surfaces for descending imagery over Hokkaido, 1/9 for ascending imagery over Nepal and 2/10 for ascending imagery over Lombok-1. A comparison cannot be made for ascending track data in Hokkaido, as A116a and S085a had different look directions (westwards and eastwards respectively).

Figure 4.4 shows the landslide classification surfaces calculated using the ΔC_sum method and ALOS-2 data of each event, alongside the aggregated validation landslide data. In Figure 4.4b, d, f, cells made up of <1% landslide by area are masked. In order to recreate this in the radar surface, it was necessary to threshold and plot only pixels that were most likely to be landslides based on their classifier value. Here I applied a threshold such that the number of pixels plotted in panels (a, c, e) is the same as the number in panels (b, d, f), respectively. These threshold values were similar, but not identical, and I expect that more case study sites would be required to determine a more general threshold for application in future events. However, in each case, the spatial pattern of landsliding in (b, d, f) was recreated using the radar surfaces (a, c, e), which would allow the worst affected areas to be
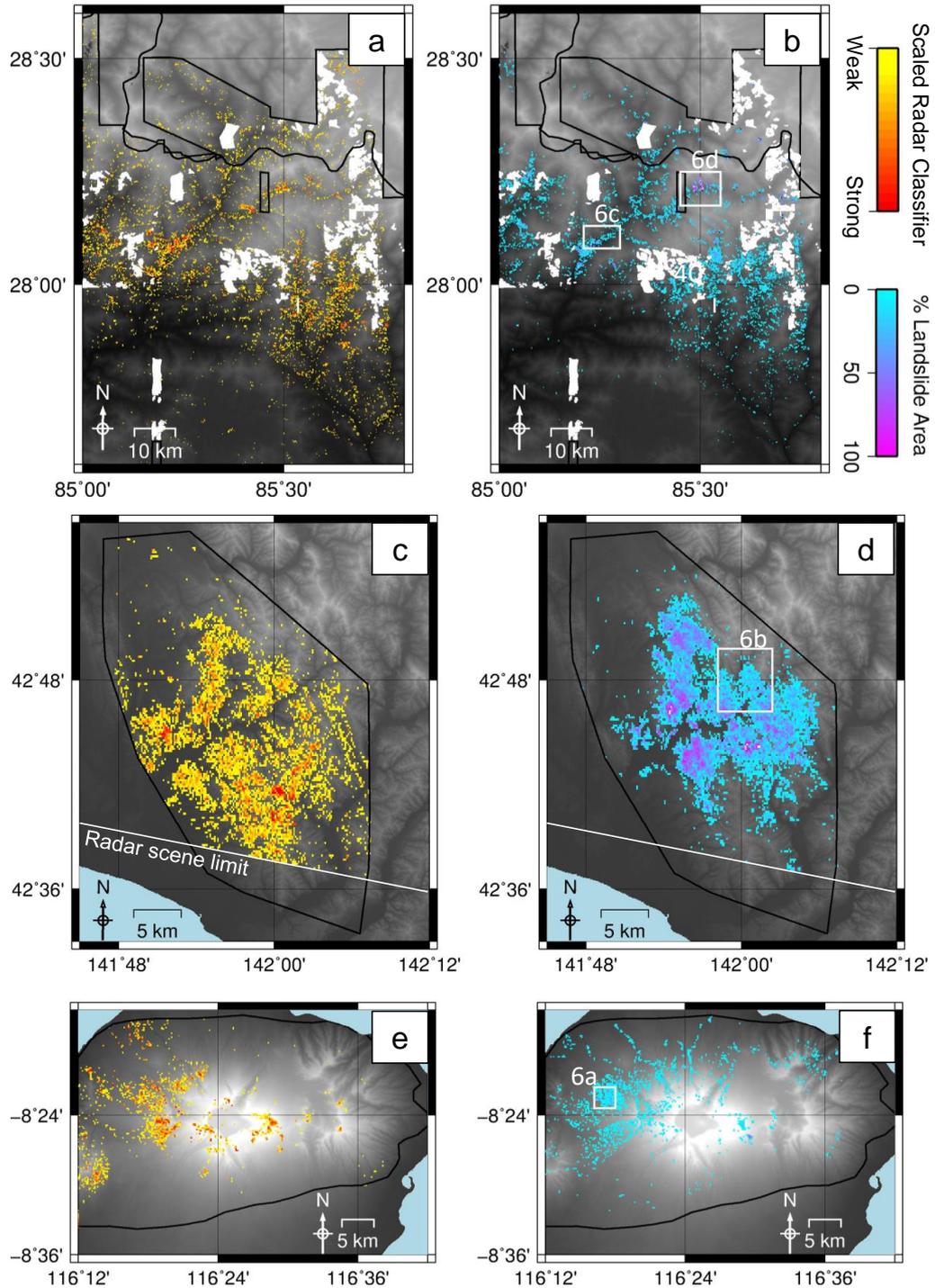
Figure 4.4: SAR-based landslide classification surfaces for the Gorkha (a), Hokkaido (c) and Lombok-1 (e) earthquakes calculated with ALOS-2 radar data using the ΔC_sum method at a 200 m × 220 m resolution. (b, d, f) Observed landslide density calculated as the percentage of each 200 m × 220 m cell covered by landsliding for each event according to the inventories of Ferrario (2019), Roback et al. (2018), Zhang et al. (2019) respectively. Cells where landslide density was 0 were masked. For the ΔC_sum surface, a threshold value of the classifier was selected such that the number of cells plotted in panels (a, c, e) for each event was the same as the number plotted in panels (b, d, f)

identified for emergency response even without strict definition of this threshold.

4.3.2   Variation across event and sensor type

The AUC values varied significantly across event and sensor type. L-band radar outperformed C-band in the majority of cases, but for some methods, I observed additional effects causing differences in performance.

For methods relying on a co-event vs. pre-event coherence decrease (i.e. ARIA, ΔC_sum, ΔC_max), landslides associated with Lombok-2 were more difficult to predict than Lombok-1 (Figure 4.2). This is likely to be due to the co-event acquisition time window, which was 6 days for the first inventory, but had to be increased to 18 days on track S156a and 24 days on S032d in order to span both earthquakes. This will have caused temporal decorrelation of vegetated non-landslide pixels, resulting in a smaller difference between landslide and non-landslide co-event coherence and making it more difficult for the classifier to distinguish between these. The same effect was seen in Nepal, where 12 day interferograms were used for S019d, but 24 day pre-event and co-event interferograms were used for S085a.

Generally, the Bx-S method was more consistent across sensor type than the ARIA method. The ARIA method performed better than the Bx-S method with ALOS-2 data, but worse with Sentinel-1. There are several possible reasons for this. First, the longer wavelength of L-band SAR meant that it was able to maintain a higher coherence in the pre-event interferogram, so that the coherence difference for a landslide pixel in a pre-event and co-event interferogram was larger, resulting in better performance from ARIA. Second, in the Bx-S method, siblings are identified using pre-event imagery. As Sentinel-1 imagery is acquired every 12 days, more images were available for this calculation and were acquired over a shorter time period (Figure 4.1). Therefore it may be that the siblings selected by RapidSAR were of a higher quality when using Sentinel-1 imagery than when using ALOS-2, giving a more reliable sibling coherence estimate.

4.3.3   Results at 20 m × 22 m resolution

While the main aim of this chapter was not to map individual landslides, I also show results at a 20 m x 22 m scale (the resolution of the classification surfaces in geographic coordinates), with pixels that are sufficiently small to resolve individual landslides (Figure 4.5). My results show that SAR methods were less successful at this resolution than when downsampled, with AUC on average 16 % lower using Sentinel-1 data and 11 % lower using ALOS-2 data. Using Sentinel-1 data, AUC

values were low, ranging from 0.49 (ARIA, Lombok-2) to 0.61 (PECI, Hokkaido). From this I conclude that mapping individual landslides with Sentinel-1 data was not possible using the methods tested here, which supports similar preliminary findings presented in Chapter 3.

Classification surfaces using ALOS-2 are more promising, with AUC up to 0.80 (ΔC_max, Lombok-1). As in Section 4.3.1, ΔC_sum performed best, having the highest AUC on tracks A116a and A157a, and an AUC of only 0.01 less than the best performing classification surface on tracks A018d and A129a. Figure 4.6 shows small regions of this surface overlain with landslide polygons for each event. While the landslides generally coincide spatially with high classifier values, it is clear that it would not have been possible in most cases to map the landslide polygons using the radar data. Some large landslides (Figure 4.6b, d) contain pixels with high classifier values. However, in (d), there are also areas of mapped landslide that do not have high classifier values, and in (a) and (c) the landslides are too small. Therefore I conclude that, while radar coherence methods show promise in individual landslide detection, it was not possible using the methods tested here, and there is likely to be a minimum detectable landslide size, which will depend on the spatial resolution of the SAR data.

	Event	Hokkaido				Nepal			Lombok			Lombok 2	
	Satellite	S-1		A-2		S-1		A-2	S-1		A-2	S-1	
	Track number	068a	046d	116a	018d	085a	019d	157a	156a	032d	129a	156a	032d
1 post-event image	ARIA	0.51	0.51	0.62	0.72	0.52	0.58	0.68	0.53	0.50	0.76	0.50	0.49
	Bx-S	0.52	0.52	0.52	0.51	0.56	0.59	-	0.54	0.52	0.69	0.53	0.52
	Waiting time (days)	8	0	1	1	8	4	7	3	0	13	1	4
2 post-event images	PECI	0.60	0.61	0.60	0.65	0.54	0.55	0.67	0.53	0.54	0.76	0.53	0.55
	ΔC_sum	0.57	0.58	0.63	0.71	0.54	0.57	0.72	0.54	0.52	0.79	0.52	0.52
	ΔC_max	0.58	0.59	0.60	0.72	0.53	0.57	0.70	0.54	0.53	0.80	0.52	0.54
	Waiting time (days)	20	12	15	15	20	16	91	9	6	153	7	10

Figure 4.5: AUC values for each classifier described in section 4.2.3 at a resolution of 20 m × 22 m. For Hokkaido, I use the inventory of Zhang et al. (2019). Insufficent pre-event data were available on A157a to calculate the Bx-S classification surface. Colours range from red (worst performing AUC < 0.55) to green (best performing, AUC >0.80).
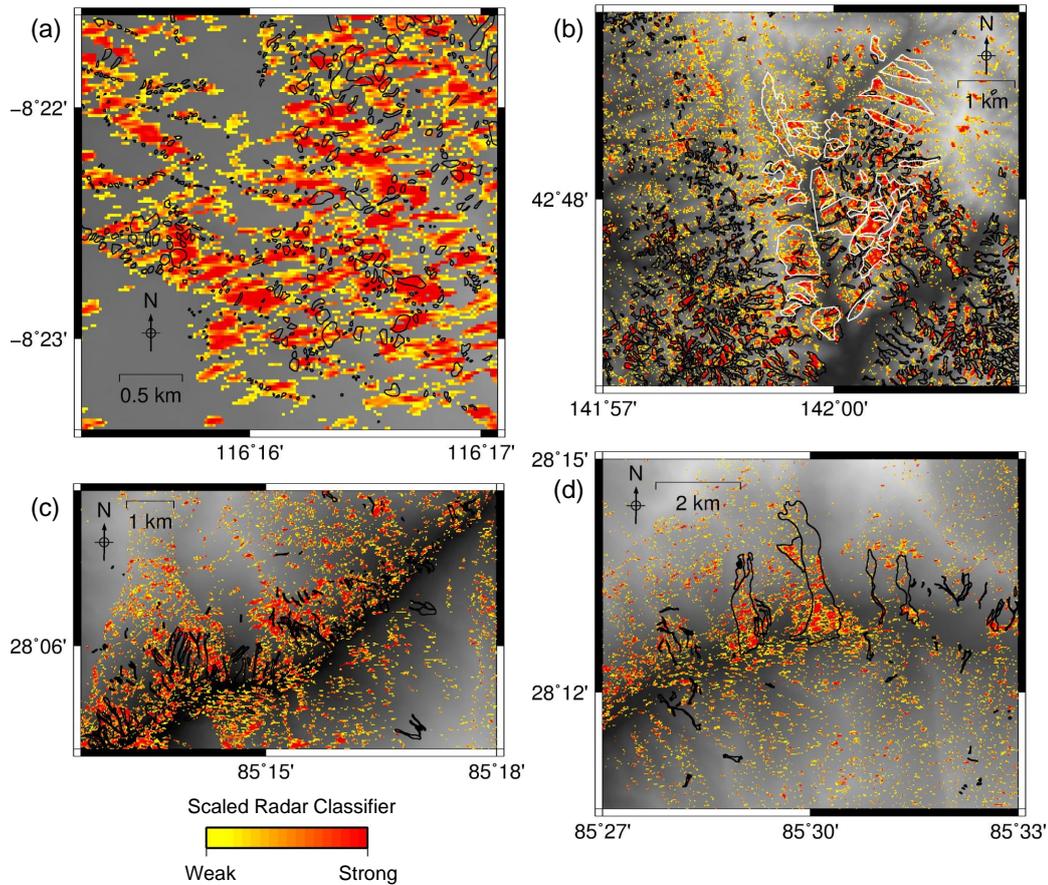
Figure 4.6: ΔC_sum classification surface calculated using ALOS-2 data displayed at 20 m x 22 m resolution with mapped landslide polygons in black. (a) Lombok: track A129a for the 5 August 2018 event (Ferrario, 2019). (b) Hokkaido: track A018d, landslide polygons from Zhang et al. (2019). White polygons show the locations of forested areas mapped using Sentinel-2 data. (c,d) Nepal: track A157a(C), landslide polygons from Roback et al. (2018).

4.4 Discussion

In this chapter, I have demonstrated that SAR data are widely applicable to landslide detection in vegetated areas within the timeframe of the emergency response effort. For example, within the two week limit suggested by Inter-Agency Standing Committee (2015); Williams et al. (2018), it would have been possible to generate triggered landslide density information using the ARIA method with ALOS-2 data with an ROC AUC of 0.81 in Nepal, 0.89 in Hokkaido and 0.88 in Lombok-1 (Figure 4.2). In this section, I first consider the applications of the SAR methods to future events, and then turn to potential sources of errors. Finally I discuss future work that would allow wider application of SAR methods to landslide detection.

4.4.1 Application

4.4.1.1 Landslide density estimation

I found that radar methods were better suited to identify areas severely impacted by landslides than to the identification of individual landslides. The aggregated resolution of 200 m x 220 m that I used here was not high enough to identify individual landslides. However it was higher than the resolution of most empirical landslide susceptibility models designed for rapid response (Allstadt et al., 2018; Nowicki Jessee et al., 2018) and landslide maps generated from optical satellite imagery for use in aid efforts by Bessette-Kirton et al. (2019) following Hurricane Maria, Puerto Rico in 2017, and by Williams et al. (2018) following the 2015 Gorkha earthquake. SAR data seem best suited to producing products at this spatial scale. For example, Bessette-Kirton et al. (2019) produced a grid of 2 x 2 km pixels and assigned them as 'high landslide density' (>25 landslides), 'low landslide density' (1-25 landslides) or 'no landslides' (Figure 1.2c). This was published a month after the hurricane using optical imagery acquired between 6 and 18 days after the event. As radar data are available within a few days of an earthquake, equivalent products could easily be generated from radar within this timescale.

Landslide density maps can be combined with data on population density in order to estimate exposure, as in Nowicki Jessee et al. (2018). They can be used alongside maps of roads to identify transport routes that are likely to be blocked, and maps of river networks in order to identify areas where a landslide may have temporarily dammed a river, posing a risk of flash flooding when the dam collapses (Robinson et al., 2018). Information of this kind may guide aerial assessments of landslides such as that by Collins and Jibson (2015), which was carried out 32-36 days after the 2015 Gorkha earthquake to identify possible landslide dams. Although here I did not directly extract landslide density values from the SAR coherence techniques, this may be possible in the future, and is attempted in Chapter 5. Furthermore, the areas of intense landsliding identified using the techniques tested in this chapter could be applied in a similar manner to landslide density information, by allowing identification of the worst hit areas in the initial phases of the emergency response.

4.4.1.2 Recommendations on data and methods

I showed in Section 4.3 that, in the majority of cases, landslide classification surfaces generated using L-band data outperformed those generated from C-band data. Currently, the main source of L-band data is the ALOS-2 satellite system. This system has a 14 day repeat time and one of its objectives is disaster response.

Therefore, in most cases, a post-seismic image will be made available within two weeks of an earthquake, with the main purpose of producing a co-seismic interferogram that can be used to measure ground displacement and infer fault geometry. However, as this interferogram requires only one post-seismic image, the waiting time for a second image may be several months, as was the case following the Nepal and Lombok earthquakes. Therefore in an emergency response situation, it is likely that only one L-band image will be available within the required timeline, and so the ARIA method would be the best available classification surface. L-band data are also less likely to be acquired following a rainfall event, even if this event triggers many landslides, as ground displacement maps and therefore interferograms are not needed. In the future, however, the availability of L-band SAR is likely to increase with the planned NiSAR and ROSE-L satellite constellations. The NASA-ISRO NiSAR mission, planned to launch in 2022, will acquire L-band data continuously with a 12-day repeat time over all landmasses globally (Sharma, 2019), while the ESA ROSE-L constellation, whose launch date is planned in 2026 will have 6-day global repeat coverage, and 3-day in Europe (Pierdicca et al., 2019).

While Sentinel-1 data yield generally lower AUC values (Figures 4.2a, 4.5), the system acquires data continuously over global tectonic belts with a 12 day repeat time, with all data made freely available. Image acquisitions on ascending and descending tracks are offset in time so that the waiting time for a single post-event track is always less than 6-12 days. Over Europe, Sentinel-1 data are acquired at twice this frequency, meaning that the first post-event image should be available within 3 days (ESA, 2019). As the data are regularly acquired, they will be available for rainfall events as well as earthquakes. In some cases, two post-event Sentinel-1 images may be acquired before the first ALOS-2 image becomes available. It is more difficult to make a definitive recommendation for the best method to use in this situation, as performance varies significantly between events. With one post-event image, the Bx-S method is the best performing classifier with Sentinel-1, and in Nepal remains the best classifier even after additional post-event Sentinel-1 images have been acquired. With two post-event images, the best performing classifier in 2 out of 8 cases is either ΔC_sum or ΔC_max. However in cases where the presence of vegetation means that pre-event coherence and non-landslide co-event coherence are very low, the best option is to use PECI (e.g., Lombok-1 S032d, Lombok-2, Hokkaido). Inspection of the pre-event coherence should therefore be carried out first to select which method to use.

4.4.2 Sources of incorrect classifications

4.4.2.1 Building damage

As the ARIA method was originally designed to detect urban damage, it is un-surprising that damaged buildings cause false positives in SAR coherence-based methods for landslide detection. Large scale signals, such as the town of Atsuma in Hokkaido, could be removed using a land cover map, but masking landslides in built-up areas is clearly disadvantageous as this is where they would do the most damage. Additionally, buildings located outside of large towns may not be included in such maps, but damage to these would still result in false positives. These false positives will occur using all the methods in this study. They are particularly likely to have negatively affected the AUC values for A116a in Hokkaido, as this track had a larger proportion of non-landslide pixels lying in built up areas.

4.4.2.2 Wind damage

In Hokkaido, I observed some large false-positive patches in ARIA, PECI, ΔC_sum and ΔC_max classification surfaces using ALOS-2 data and PECI, ΔC_sum and ΔC_max surfaces using Sentinel-1. These correspond spatially to areas of ever-green needleleaf forest in the Japanese Aerospace Exploration Agency (JAXA) high resolution land use and land cover map of Japan (JAXA, 2018). Areas with this forest cover, which I mapped using Sentinel-2 imagery, are outlined in white on Figure 4.6b.

I hypothesise that this type of vegetation may have been damaged by wind during Typhoon Jebi, which passed over the area the day before the earthquake, causing a coherence decrease that is similar to that caused by landsliding. This type of forest has a comparatively high coherence in both pre-event and post-event L-band interferograms, giving it a strong signal in ARIA, PECI, ΔC_sum and ΔC_max. This effect may also explain why the low coherence area extends beyond the area affected by landslides (an effect visible in my data, and also observed by Fujiwara et al. (2019)). Unfortunately, none of the SAR data in this study were acquired between the typhoon and the earthquake, which would have allowed separation of the two events. However, these forest patches have no signal in amplitude-based methods, which has been observed in the study of Fransson et al. (2010) of wind-damaged forest at this resolution. This lack of an amplitude signal may allow these false positives to be removed through a combination of amplitude and coherence-based classification surfaces. Additionally, I observed that these patches of forest

are generally much larger than the landslides and so could perhaps be removed if object- rather than pixel-based classification were used.

4.4.2.3 Snow

Snow is a potential source of error when using SAR in landslide detection. There is a strong difference in SAR backscattering properties between wet snow, dry snow and no snow (Koskinen et al., 1997). As such, decreased coherence can be caused by snow melt, drift or fall between image acquisitions. Examination of Sentinel-2 imagery shows there was no snow cover at the time of the Hokkaido earthquake, and snow is not likely in Lombok due to the high temperatures. I do not have exact snow cover data for Nepal at the time of the earthquake, but in April approximately 1/5 of the country's total area would have been covered in snow (ICIMOD, 2013). Therefore at high altitudes, it is reasonable to assume that some false positives may have been caused by snow, particularly on track A129a due to the long time interval between image acquisitions.

4.4.2.4 Rivers

The Bx-S method is effectively a spatial filter on co-event coherence, removing signals that cover a large area. Therefore small, low coherence objects will be identified as landslides. This includes rivers, as demonstrated by Spaans and Hooper (2016). As the low coherence caused by a river is not temporary, this should have less of an effect on the other coherence methods tested here. However, changes in position or water level are likely to result in false positives in all coherence-based classifiers.

4.4.2.5 Landslide density

When using the Bx-S method in Hokkaido, I found low AUC values with both L-band and C-band SAR. Visual comparison of the boxcar and sibling coherence surfaces shows that the area affected by landslides had a low coherence in both, rather than the expected case where the boxcar coherence is lower than the sibling coherence. I suggest this may be due to the intensity of the damage caused by this event, both in terms of the landslides, which had a much higher density than for Nepal or Lombok, and possibly also in terms of vegetation damage caused by Typhoon Jebi. Since the Bx-S method relies on siblings of a landslide pixel lying outside the landslide, it may not work well in the case where many landslides are close together. This is similar to the case found in Section 3.4.2, where the Bx-S

method was unable to identify large landslides if the sibling search window was not sufficiently large.

4.4.3 Future work

I have demonstrated that the classification ability of a method can vary significantly based on the data used, the nature of the triggering event, and the resolution of the analysis. For example, the Bx-S method performed significantly better in the case of Nepal than Hokkaido, and the ARIA method was up to 32% more successful when using ALOS-2 compared to Sentinel-1 data with the same event and look direction. Thus it is clear that any future SAR-based classification method must be widely tested on multiple events, and it cannot be assumed that a method performing well with one SAR dataset will be equally successful using data from a different sensor.

While I tested ascending and descending tracks separately, a more complete picture would be obtained through combining these two tracks, as hillslopes which are unfavourably oriented to the satellite in one track are likely to be more favourably oriented to the other track. A complete map would be easier to interpret for emergency responders than two maps, each of which is missing landslides on unfavourably oriented slopes. This is particularly important since landslides are most likely on steep slopes where these orientation effects are likely to be most severe.

Although I selected earthquakes to use as case studies, SAR methods could be equally useful in the case of rainfall-triggered landslides, where cloud cover may also cause delays to mapping using optical satellite imagery. I have shown that SAR methods performed well in Hokkaido, where the co-event coherence maps spanned both an earthquake and a typhoon. This demonstrates that the alterations in SAR coherence and amplitude that can result from changes in soil moisture content are not prohibitive to the application of SAR methods to rainfall-triggered landslides, although some false positives may have been caused by wind damage.

The Lombok case studies demonstrate the importance of knowing the timing of the landslides when applying current methods. When moving from Lombok-1, in which all landslides were assumed to have been triggered by a single earthquake, to Lombok-2, which contained landslides triggered by a series of earthquakes over a two-week period, it was necessary to increase the timespan of the Sentinel-1 co-event interferograms from 6 days to 24 days on track S032d and 18 days on track S156a, which significantly reduced the AUC of the classification methods. Therefore, if we wish to apply radar methods more widely to landslide triggering events that are dispersed through time, such as long rainfall events (e.g., those

associated with the monsoon) or earthquake sequences, more work will be required on the characterisation of the signals of landslides in radar imagery through time.

4.5 Conclusions

I have demonstrated that it is possible to generate landslide density information from SAR coherence within a typical two-week emergency response time-frame and at a useful spatial resolution. The best performing method is dependent on the wavelength of the available imagery and the number of post-seismic images available during the emergency response. The ARIA method is the best performing method when only one L-band image is available (ROC AUC = 0.7-0.89), and this method could be applied within two weeks for three out of my four case study events. However, Sentinel-1 data were available earlier than ALOS-2 for all of the events studied here, with the first image available within 4 days of each earthquake. Using the first post-event Sentinel-1 image acquired, the best method is the Bx-S method with AUC between 0.58-0.74. Methods that use a second post-event image improve overall accuracy by an average of 10 % and are more consistently reliable across event and sensor type. These approaches could be valuable for landslide mapping when latency is less important, but the additional waiting time for the second post-event image is a disadvantage in an emergency response situation.

Improved Rapid Landslide Detection from Integration of Empirical Models and Satellite Radar

Chapter Overview

In this chaper, I seek to integrate and compare empirical models of landslide susceptibility, which are commonly used to inform the emergency response when landslide information derived from optical satellite imagery is unavailable, and the SAR-coherence-based methods which I have presented in Chapters 3 and 4 of this thesis. I use random forest regression to combine these two methods, and demonstrate that an empirical model incorporating SAR coherence can outperform both the SAR coherence methods from Chapter 4 and an equivalent empirical model that does not use SAR data.

5.1   Introduction

Earthquake-triggered landslides are a major secondary hazard associated with large continental earthquakes and disrupt emergency response efforts. Information on their spatial distribution is required to inform this emergency response, but must be generated within two weeks of the earthquake in order to be useful (Inter-Agency Standing Committee, 2015; Williams et al., 2018). The most common method of generating landslide information is manual mapping using optical satellite imagery,

but this is a time-consuming process and can be further delayed by weeks or even months due to cloud cover (Robinson et al., 2019), leading to incomplete landslide information during the emergency response.

In the absence of optical satellite imagery, there are two options for generating information on the intensity and spatial extent of landslides in the immediate aftermath of a large earthquake. The first is to produce empirical susceptibility maps, using factors such as slope, lithology and estimations of ground shaking intensity to predict areas where landslides are likely to have occurred (e.g. Nowicki Jessee et al., 2018; Robinson et al., 2017; Tanyas et al., 2019). The second is to estimate landslide locations based on their signal in SAR data, which can be acquired through cloud cover and so can provide a more complete picture than optical satellite imagery (e.g. Chapters 3 and 4 of this thesis; Aimaiti et al., 2019; Jung and Yun, 2019)

To generate an empirical landslide susceptibility model, a training dataset of mapped landslides is analysed alongside maps of factors known to influence landslide likelihood such as slope, land cover and ground shaking estimates, and a model is produced that predicts landslide likelihood based on these inputs. A range of methods have been used to generate landslide susceptibility models, including Fuzzy Logic (Kirschbaum and Stanley, 2018; Kritikos et al., 2015; Robinson et al., 2017), Logistic Regression (Nowicki Jessee et al., 2018; Tanyas et al., 2019) and Random Forests (Catani et al., 2013; Chen et al., 2017). When generating a susceptibility map for emergency response, the training dataset can be either a global collection of earthquake-triggered landslides (e.g. Kritikos et al., 2015; Nowicki Jessee et al., 2018; Tanyas et al., 2019), or a small sample of the affected area mapped immediately following the earthquake (e.g. Robinson et al., 2017). Here, I will refer to these two model types as "global" and "same-event" models respectively. The global model of Nowicki Jessee et al. (2018) is routinely used to generate landslide predictions after large earthquakes, which are published on the USGS website `https://earthquake.usgs.gov/data/ground-failure/`. These models provide useful predictions of landslides for earthquakes within hours of the event (e.g. Thompson et al., 2020, Figure 1.5). However, the model has been shown to struggle in the case of complicated events, for example in 2018, when landslides were triggered by a series of earthquakes in Lombok, Indonesia, rather than a single large event (Ferrario, 2019).

Several SAR methods have been developed for use in earthquake-triggered landslide detection (e.g. Chapters 3 and 4 of this thesis; Jung and Yun, 2019; Mondini et al., 2019; Yun et al., 2015). SAR data can be acquired in all weather conditions, and with recent increases in the number of satellites in operation, data are likely to

be acquired within days of an earthquake anywhere on Earth. In vegetated areas, the removal of vegetation by a landslide alters the scattering properties of the ground surface, giving it a signal in SAR data. In Chapter 4, I demonstrated that such methods can be widely applied in vegetated areas, and can produce useable landslide information within two weeks of an earthquake. However, in some cases false positives can arise from building damage or factors such as snow or wind damage to forests (Section 4.4.2).

Recently, Masato et al. (2020) and Aimaiti et al. (2019) have demonstrated the possibility of combining SAR-based landslide indicators with topographic parameters in order to improve classification ability. Aimaiti et al. (2019) used a decision tree method to combine topographic slope with SAR intensity and coherence to detect landslides triggered by the 2018 Hokkaido earthquake, and Masato et al. (2020) used Random Forest classification to combine several landslide indicators based on polarimetric SAR and topography to detect landslides triggered by two events in Japan: the 2018 Hokkaido earthquake and heavy rains in Kyushu, 2017. While these studies established the promise of a combined approach to landslide detection, they did not assess the relative merits of empirical, SAR and combined methods. Furthermore, the two studies combined only SAR and topographic landslide indicators, omitting factors such as lithology, land cover and ground shaking data, which are also commonly used in empirical landslide modelling (Nowicki Jessee et al., 2018; Robinson et al., 2017).

In this chapter, I aim to establish which of these three options is best: Susceptibility maps, SAR-based landslide detection, or a combination of these. In order to do this, I began with a same-event empirical model of landslide susceptibility based on ground shaking, topography, lithology and land cover, all of which are available within hours of an earthquake. For the modelling, I used Random Forests, a machine learning technique that has been demonstrated to perform well in landslide detection (Chen et al., 2017). I chose to model landslide areal density rather than individual landslide locations as both empirical models and SAR-based methods perform best at relatively low spatial resolutions (within the range 0.01-1 km^2) (Chapters 3 and 4; Nowicki Jessee et al., 2018; Robinson et al., 2017). This output is different to the majority of empirical models, which usually produce a map of predicted landslide probability (e.g. Nowicki Jessee et al., 2018; Robinson et al., 2017), and SAR methods, which produce either a binary classification surface or a landslide intensity proxy map (e.g. Chapters 3 and 4; Yun et al., 2015).

I then progressively added SAR data to the inputs used in this initial empirical model in the order in which they became available following each case study earthquake. At each stage in this process, I assessed the ability of the model to recreate

the landslide areal density in the test area of the landslide dataset using ROC analysis and by calculation of the root mean squared error (RMSE). Using ROC analysis, the classification ability of all of these models can be compared with the results from individual SAR-based methods presented in Chapter 4. This allows conclusions to be drawn on the relative performance of empirical landslide susceptibility models, SAR-based landslide detection, and combined models. I focus primarily on the same-event model type, but also assessed the performance of a limited global model in which I trained on landslide data from two earthquakes and predicted the third, allowing speculation on the performance of a global model trained on a larger number of earthquakes.

5.2 Data and Methods

When generating an empirical model of, in this study, landslide areal density, the aim is to take a selection of input features (e.g. slope, elevation, land cover) that influence landslide likelihood and to carry out some form of regression on a training dataset of mapped landslides. The relationships established by this regression can then be used to predict landslide areal density in areas where there are no mapped landslide data available based on these input features. Here, I used Random Forests to carry out this regression.

5.2.1 Random Forest Theory

Random Forests are an extension of Decision Tree methodology, in which a large number of decision trees, each seeing different combinations of input data, are combined. This avoids overfitting the training data, a problem when using individual decision trees (Breiman, 2001). A very simple example of the Random Forest method using only two trees to estimate the value a sample should be assigned based on colour and shape is shown in Figure 5.1. First the training dataset is bootstrapped so that each tree sees only a subset of the original pixels (Figure 5.1a). Each tree carries out a series of 'splits', in which the data are divided in two based on some criteria, for example having a slope value of less than or more than 30° (Figure 5.1b). These splits are chosen based on the improvement they offer to the ability of each tree to correctly predict its training data. Every tree remembers how it split the training data, and then applies the same splits as it attempts to model the test data (Figure 5.1c). For Random Forest Regression, the mean value of all trees is taken as the model output for every sample (Breiman, 2001).
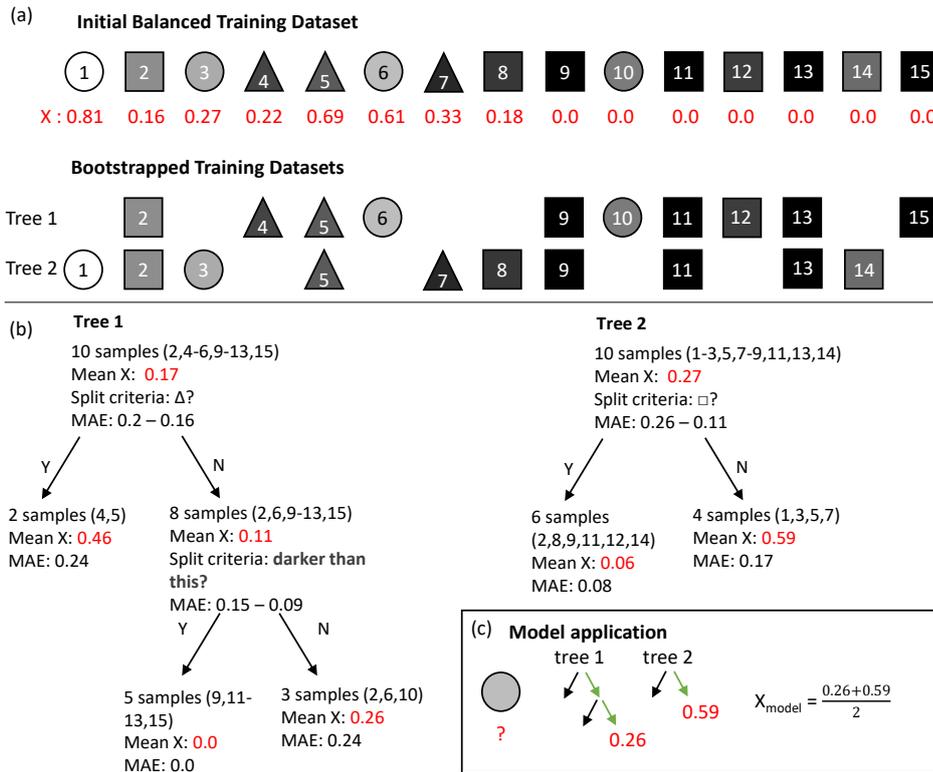
Figure 5.1: A simplified example of Random Forest Regression with a forest of two trees. The value of X for a sample is modelled based on its shape and colour. An initial dataset in (a) is bootstrapped to produce two slightly different datasets for use in tree 1 and tree 2. (b) Two trees which reduce mean absolute error. At each node, the number of samples, the mean value of the samples, the input feature on which the samples are split, and the mean absolute error of the samples before and after ("before - after") the split if they are assigned the mean value is listed. In (c) the value of X for a new sample is modelled from the average output across both trees.

Random Forests are relatively computationally inexpensive, and because of this, can use a large number of input features. Unlike, for example Logistic Regression, Random Forests do not require input features to be independent, which is advantageous here due since coherence is sensitive to both slope (due to decorrelation of $\gamma_{spatial}$, Section 2.4) and land cover, as well as the presence or absence of landslides. Input features of Random Forests do not need to be monotonic and can be categoric or continuous. Catani et al. (2013); Chen et al. (2017) and Masato et al. (2020) have demonstrated that Random Forests can yield good results in landslide detection. Random Forests are therefore well suited to the combination of SAR methods with static landslide predictors.

5.2.2 Implementation

To implement the Random Forests method, I used the python scikit-learn package (Pedregosa et al., 2011). The model is defined by a number of parameters that can have a noticeable effect on the model. First of these is the criteria on which a split should be assessed. In my model, splits were carried out that minimised mean absolute error (MAE). This criterion was selected based on Ziegler and König (2014). The second parameter describes the bootstrapping step (e.g. Figure 5.1a). Here the data were bootstrapped so that a number of random samples was taken equal to the number of pixels in the training dataset. Each individual pixel is therefore likely to appear in around two thirds of the bootstrapped datasets (Efron and Tibshirani, 1997). This process improves the stability of the model by ensuring that each tree is trained on a slightly different subset of the training data (Breiman, 2001).

Table 5.1 shows a further five parameters that define the setup of a Random Forest model in scikit-learn. First the number of trees, n_estimators, defines the number of decision trees that make up a forest. More trees can increase model accuracy up to a point, but also result in a more computationally expensive model. Second, max_features defines how the fraction of possible input features considered when carrying out a split is calculated. For example, here I had 17 input features, so with square root (sqrt) selected, four input features would be considered at each split. Max_depth defines the maximum "depth" of each decision tree i.e. the longest path length from the beginning of the tree to the end. For example, in Figure 5.1, tree 1 has a depth of 3 and tree 2 has a depth of 2. Finally, min_samples_split is the minimum number of samples a node has to contain before splitting for a split to be allowed, while min_samples_leaf is the minimum number of samples assigned to either branch after splitting for a split to be allowed. For each of these five parameters, I selected several possible options, which are shown in the final column of Table 5.1. I then used the GridSearchCV function in sci-kit learn to select an optimised model by running multiple models with every possible combination of these values (Pedregosa et al., 2011).

5.2.3 Landslide datasets

I used polygon landslide inventories compiled for three large earthquakes that each triggered thousands of landslides: the inventory of Roback et al. (2018) of 24,915 landslides triggered by the M_w 7.8 2015 Gorkha, Nepal earthquake; the inventory of Zhang et al. (2019) of 5,265 landslides triggered by the M_w 6.6 Hokkaido, Japan earthquake; and the inventory of Ferrario (2019) of 4,823 landslides triggered by the

Table 5.1: Options for the Random Forest in Scikit-learn over which a grid search optimisation was carried out (Pedregosa et al., 2011).

Parameter	Definition	GridSearch
n_estimators	The number of decision trees that make up a forest	[75, 100, 125]
max_features	The number of input features (as a function of the total) considered when looking for a split	['log2','sqrt']
max_depth	The maximum depth of the tree	[10,15,20,30]
min_samples_split	The minimum number of samples at a node for a split to be allowed	[2,3,4,5]
min_samples_leaf	The minimum number of samples that would result at each leaf for a split to be allowed	[2,10]

M_w 6.8 Lombok, Indonesia earthquake on 5 August, 2018 (See Figure 4.1 for the extent of triggered landslides from each of these earthquakes and the spatial and temporal coverage of the SAR data used in this chapter. The earthquake referred to as 'Lombok-2' in Chapter 4 is not included in this chapter). In Chapter 4, I assessed the ability of five SAR coherence methods to identify landslides against these datasets using Sentinel-1 and ALOS-2 data, which allows a direct comparison in this chapter between the performance of models developed here and that of existing SAR coherence methods of landslide detection. These polygon inventories were converted to rasters with a cell size of 20 x 22 m. As in Chapters 3 and 4, I then calculated an aggregate landslide surface with a resolution of 200 x 220 m, by calculating the landslide areal density within 10 x 10 squares of these 20 x 22 m cells.

5.2.4 Training and test datasets

Here I used two types of empirical landslide susceptibility model: "same-event" models trained on a small mapped area of an event to predict the landslide distribution across the rest of the affected area (e.g. Robinson et al., 2017) and global models trained on historic landslide inventories to predict a new event (e.g. Kritikos et al., 2015; Nowicki et al., 2014; Nowicki Jessee et al., 2018; Tanyas et al., 2019).

The idea behind a same-event model is that a small number of landslides can be mapped manually from optical satellite imagery in the days following the earthquake. The distribution of these landslides can then be used to predict the landslide distribution across the whole affected area in much less time than would be required to manually map the whole area (Robinson et al., 2017). For my same-event model, I began by using a quarter of each case study area to train the model and the remaining three quarters as test data. The locations of these test and training areas are shown on Figure 5.3. In order to produce a training dataset with equal numbers

of landslides and non-landslide cells (a balanced dataset), I randomly undersampled the non-landslide cells in the training dataset.

For the second approach, in which an empirical model is trained on a global inventory of past landslides, I trained the Random Forest on two of my case study events and predicted the third. In this case, I randomly undersampled both the landslide (>1% landslide areal density) and non-landslide pixels to select 1000 landslide and 1000 non-landslide pixels from each event. The resulting model was therefore trained on equal numbers of pixels from the two training events, rather than being dominated by whichever was larger. It should be noted that successful global empirical landslide prediction models are trained on considerably more data than this; for example, the model used by the USGS of Nowicki Jessee et al. (2018) was trained on 23 landslide inventories and the model of Tanyas et al. (2019) was trained on 25. However, Masato et al. (2020) demonstrated that when using fully polarimetric SAR data, it was possible to predict the spatial distribution of landslides triggered by the Hokkaido earthquake using a model trained on landslides triggered by a heavy rainfall event in Kyushu, 2017 (although they found it was not possible to predict landslides triggered by the Kyushu event using a model trained on Hokkaido). Fully polarimetric data are rarely available following an earthquake and are therefore not suitable for application in a global model. Therefore, here I assess whether models using single-polarisation SAR data, which are acquired by the majority of SAR satellites, can also be transferred between events.

5.2.5 Estimating uncertainty

To evaluate the most accurate way of generating landslide information, it is necessary to assess uncertainty in the Random Forest model outputs. In order to do this, I trained an ensemble of 100 models, redoing the random undersampling each time so that every model within the ensemble is trained on a slightly different set of cells. I then ran each model and took the median ensemble prediction. This process reduces variability and allows the calculation of upper and lower bounds for the landslide areal density of every pixel, as well as other statistical parameters, such as the variance.

5.2.6 Input features

A large number of possible input features have been used in previous work on landslide susceptibility mapping, including a wide range of topographic parameters, ground shaking estimates, rainfall data, lithology, landcover and distance to

features such as rivers, roads and faults. Here I limited the model input features to globally available datasets in order to ensure the widest applicability of the results. I targeted my model at earthquake- rather than rainfall-triggered landslides, as these have been more widely used as case studies when developing and testing SAR-based methods of landslide detection (e.g. Chapter 3; Aimaiti et al., 2019; Jung and Yun, 2019; Yun et al., 2015) and detailed polygon inventories of thousands of landslides triggered by a single earthquake (Ferrario, 2019; Roback et al., 2018; Zhang et al., 2019) provide a good source of test and training data for the model. The input features I used and their data sources are summarised in Table 5.2. Some input features were used only in the same-event models and not for the global models. This is specified in the fourth column of Table 5.2.

5.2.6.1 Topographic features

For input features derived from topography, I used the 30 m SRTM DEM (Farr et al., 2007). When processing the SAR data, this DEM was resampled to a resolution of 20 m $\times$ 22 m. From this resampled DEM, I calculated slope and aspect values of every cell. I aggregated 10 $\times$ 10 grids of these cells to produce input features at a 200 m $\times$ 220 m scale. For each aggregate 200 $\times$ 220 m cell, I calculated the average 20 m $\times$ 22 m cell elevation (used by Catani et al., 2013; Nowicki et al., 2014), the standard deviation of cell elevations (used by Catani et al., 2013), the maximum slope (used by Nowicki et al., 2014), the average slope (used by Nowicki Jessee et al., 2018; Robinson et al., 2017; Kritikos et al., 2015; Tanyas et al., 2019), the standard deviation of pixel slopes (used by Catani et al., 2013; Tanyas et al., 2019), the circular mean of the aspect (used by Chen et al., 2017) and the relief, or maximum elevation difference between 20 m $\times$ 22 m pixels within the aggregate cell (used by Tanyas et al., 2019).

5.2.6.2 Ground Shaking Estimates

The inclusion of ground shaking information is what differentiates between a static estimate of landslide susceptibility such as that of Nadim et al. (2006) and an earthquake-specific prediction of triggered landsliding. Past studies have used Modified Mercalli Intensity (Kritikos et al., 2015; Tanyas et al., 2019), peak ground acceleration (Robinson et al., 2018; Nowicki et al., 2014; Tanyas et al., 2019) and peak ground velocity (PGV) (Nowicki Jessee et al., 2018; Tanyas et al., 2019). Here, I used PGV, as this does not saturate at high shaking intensities (Nowicki Jessee et al., 2018).

Input feature	Description	Data source	Used in global model?
Elevation	The mean elevation of pixels within the aggregate pixel	SRTM DEM (Farr et al., 2007)	No
Elevation_std	The standard deviation of pixel elevations within the aggregate pixel	SRTM DEM (Farr et al., 2007)	Yes
Slope	The mean slope (calculated with a 3 x 3 moving pixel window) of pixels within the aggregate pixel	SRTM DEM (Farr et al., 2007)	Yes
Slope_std	The standard deviation of slopes (calculated with a 3 x 3 moving pixel window) of pixels within the aggregate pixel	SRTM DEM (Farr et al., 2007)	Yes
Slope_max	The maximum slope (calculated with a 3 x 3 moving pixel window) value of pixels within the aggregate pixel	SRTM DEM (Farr et al., 2007)	Yes
Relief	Elevation range across all pixels within the aggregate pixel	SRTM DEM (Farr et al., 2007)	Yes
Aspect	The circular mean direction faced by each pixel within the aggregate pixel	SRTM DEM (Farr et al., 2007)	No
PGV	The peak ground velocity estimated from ground motion prediction equations averaged within each aggregate cell	USGS ShakeMap website	Yes
Lithology	The dominant lithology within the aggregate pixel	Global Lithological Map database (Hartmann and Moosdorf, 2012)	Yes
Landcover	The dominant land cover type within the aggregate pixel	ESA CCI 2014 Landcover map (ESA, 2017)	Yes
Co-event coherence	Mean co-event SAR coherence of pixels within the aggregate pixel	1 pre-event and 1 post-event SAR image	Yes
ARIA	Decrease in co-event vs. pre-event coherence (Yun et al., 2015)	2 pre-event and 1 post-event SAR images	Yes
Bx-S	See Chapter 3	1 post-event and at least 6 pre-event SAR images	Yes
Post-event coherence	Mean post-event coherence of pixels within the aggregtate pixel	2 post-seismic SAR images	Sentinel-1 only
PECI	Increase in post-event vs. co-event coherence (Chapter 4)	1 pre-event and 2 post-event SAR images	Yes
Δ_sum	Sum of ARIA and PECI (Chapter 4)	2 pre-event and 2 post-event SAR images	Yes
Δ_max	Whichever is larger of ARIA or PECI (Chapter 4)	2 pre-event and 2 post-event SAR images	Yes

Table 5.2: Inputs used in model partitioned into static indicators of landslide likelihood (top) and SAR landslide detection methods (bottom)

An initial estimate of ground shaking is generally available within hours of an earthquake from the USGS ShakeMap webpage, and is then refined as more data become available. Allstadt et al. (2018) demonstrated that in some cases, such as the 2016 M$_w$ 7.8 Kaikōura, New Zealand earthquake, the version of the shaking estimate used can have a significant impact on the modelled landsliding. Further examples of this have been observed for the M$_w$ 7.1 2018 Anchorage,Alaska earthquake (Thompson et al., 2020) and for a recent M$_w$ 6.6 earthquake in the Phillippines (Figure 1.5). Although my results are presented as a timeline where the model was revised as SAR data became available, I used the same version of PGV throughout, which is the final available model for each event. My inital susceptibility model may therefore perform better than one that uses the data made available within the first few hours of the earthquake. However, since the availability of SAR data for ground deformation measurements is one of the factors that can significantly improve the shaking estimate, it is useful to examine the effect of adding SAR to models using later ShakeMap versions. Currently, it is commonly necessary to wait a couple of days for the first SAR image to be acquired (e.g. Figure 4.2), and comparison between a model released within hours of an earthquake and one incorporating SAR data acquired much later would not be useful.

5.2.6.3 Lithology

Lithology is one factor that determines rock strength, and therefore landslide likelihood (Nadim et al., 2006), and has been used in several empirical landslide susceptibility models (Chen et al., 2017; Kirschbaum and Stanley, 2018; Nowicki Jessee et al., 2018). I used the Global Lithological Map database (GLiM) (Hartmann and Moosdorf, 2012), which has 13 basic lithological classes, with additional 'water bodies', 'ice and glacier' and 'no data' classes, which are supplied as polygon data. For each 200 x 220 m pixel, I took the dominant basic lithological class, resulting in a categorical input feature. One advantage of Random Forests is their ability to use both continuous and categorical input features, but empty categories in the training data can lead to biases in the model (Au, 2018). To avoid this, I used the 'onehot' method, in which each category is supplied to the model as a separate dummy input feature i.e. a binary surface of, for example, 'unconsolidated sediment' and 'everything else' (Au, 2018).

5.2.6.4 Land Cover

Nowicki Jessee et al. (2018) used land cover as a proxy for vegetation coverage and type, as the composition of the soil and the presence or absence of plant roots

can affect slope stability. Here I used land cover data downloaded from the ESA Climate Change Initiative, which includes yearly maps of 22 land cover categories compiled at a 300 m resolution from 1992-2015 (ESA, 2017). I used the 2014 map as the most recent land cover map preceding all of my case study events. Like lithology, land cover is a categorical variable, thus I used the same 'onehot' method described in Section 5.2.6.3 to avoid biasing due to empty categories, and selected the dominant land cover type within each 200 m x 220 m aggregate cell.

5.2.6.5   SAR coherence features

In this Chapter, I aimed to combine SAR coherence methods with empirical models. To achieve this, I used multiple SAR coherence methods as input features. The coherence of an interferogram is estimated to indicate the signal quality of every pixel, and is sensitive to physical changes to the Earth's surface (See Chapter 2 for more detail). The first coherence method I used was the coherence of the co-event interferogram (formed from two images spanning the earthquake). The movement of material and removal of vegetation by a landslide alters the scattering properties of the Earth's surface, resulting in low coherence. This gives landslides a low coherence in a co-event interferogram. Chapter 3 of this thesis and Vajedian et al. (2018) demonstrated that this had some potential in triggered landslide detection. Second, I used the coherence of the post-event interferogram (formed from two images acquired after the earthquake). Coherence is dependent on the land cover, with vegetated areas generally having a lower coherence than bare rock (Chapter 2). Therefore the bare rock exposed following a landslide may have a higher coherence than the surrounding vegetation.

As well as the raw coherence surfaces, I used the five coherence-based methods tested in Chapter 4 as input features, all of which showed some level of landslide predictive skill in that chapter. The ARIA method of Yun et al. (2015) uses the decrease in coherence between a pre-event and co-event interferogram to identify 'damaged' pixels. The Bx-S method presented in Chapter 3 uses the difference between two co-event coherence estimates to remove large spatial scale coherence variations from the landslide detection surface. Finally three methods presented in Chapter 4 incorporate the coherence of a post-event interferogram, using the post-event coherence increase (PECI), the sum of the co-event decrease and the post-event increase (ΔC_sum), and ΔC_max, where for every pixel, whichever is largest of PECI or ARIA is taken, to detect landslides.

For each case study earthquake, I used ascending and descending track Sentinel-1 SAR imagery and a single track of ALOS-2 PALSAR-2 imagery (Figure 4.1).

This volume of SAR data is available in the immediate aftermath of the majority of earthquakes (Figure 4.2). These two satellite systems acquire SAR data at different wavelengths, and so interact slightly differently with the ground surface, with ALOS-2 generally being less noisy in heavily vegetated areas than Sentinel-1 (Section 2.4). The SAR data were processed using GAMMA software, with Sentinel-1 data processed using the LiCSAR package (Lazeckỳ et al., 2020). The data were processed in a Range × Azimuth coordinate system and then projected into a geographic coordinate system with a spatial resolution of 20 m × 22 m. A more detailed description of the SAR data processing can be found in Section 2.3.

The majority of the methods outlined in this section use a 'boxcar' coherence estimate, using pixels from within a 3 x 3 window surrounding the target pixel in the coherence estimation. The only exception to this is the Bx-S method, which also uses a 'sibling' coherence estimate in which an ensemble of pixels is selected from within a wider window for coherence estimation using the RapidSAR algorithm of Spaans and Hooper (2016) (Chapter 3). This sibling coherence estimation requires additional data (a minimum of 6 pre-seismic images), and so it was not possible to calculate this using ALOS-2 data for the 2015 Nepal earthquake, as this event occurred very early in the lifetime of the satellite. The Bx-S method with ALOS-2 data was therefore not used in Nepal, or in any of the global models tested here.

5.2.7   Feature importances

The importance of each input feature was calculated from the decrease in MAE resulting from splits on that feature for each tree, then averaged over all the trees to obtain feature importance at forest level. This calculation gives an indication of how reliant the model is on each feature, with the sum of importances across all input features equal to one (Liaw et al., 2002). Feature importance therefore helps with interpreting the model and can allow unimportant features to be eliminated from future models, reducing computation time (e.g. Catani et al., 2013; Díaz-Uriarte and De Andres, 2006). However, it should be noted that the importance of categorical input features (here lithology and landcover), is often underestimated, since in this case the number of possible splits is limited to the number of categories present in the training data.

5.2.8   Statistical tests

Each model generated a raster of continuous predictor variables, corresponding to the modelled landslide areal density in the range [0,1]. I assessed model per-

formance by comparing the test areas of these predicted surfaces with the mapped landslide areal density calculated in Section 5.2.3.

First, in order to allow direct comparison with the results presented in Chapter 4, I carried out ROC analysis. ROC analysis requires a binary landslide surface, so, as in Chapter 4, I applied a threshold to the mapped landslide areal density surface calculated in Section 5.2.3, assigning aggregate cells with landslide areal density >25% as 'landslide' and <25% as 'non-landslide'. The false positive rate (the fraction of mapped non-landslide pixels wrongly assigned as 'landslide' by the model) and true positive rate (the fraction of mapped landslide pixels correctly assigned as 'landslide' by the model) were then calculated at a range of thresholds and plotted against each other to produce a curve. The area under this curve (AUC) then indicates the predictive skill of the model, with a value of 0.5 indicating no skill and 1.0 indicating a perfect model (Hanley and McNeil, 1982).

ROC AUC values are useful, as they allow comparison with results presented in Chapter 4, but ROC analysis is not sensitive to systematic over- or underprediction of landslide areal density by the model. Therefore, I also calculated the root mean squared error (RMSE) of every model from the difference between modelled and mapped landslide areal density (LAD^{model} and LAD^{map} respectively) for every pixel i in the test area of the dataset according to Equation 5.1, where n is the number of test pixels (Chai and Draxler, 2014).

$$RMSE = \sqrt{\frac{1}{n}\sum_{i=1}^{n}(LAD_i^{model} - LAD_i^{map})^2} \qquad (5.1)$$

The RMSE therefore gives an indication of the level of misfit between the modelled and mapped landslide areal density, while the AUC value gives an indication of the model's ability to identify pixels severely impacted by landslides.

5.3 Results

5.3.1 Same-event models

Figure 5.2 shows the effect on model AUC (panels a, b, c) and RMSE (panels d, e, f) of adding Sentinel-1 and ALOS-2 data to a landslide susceptibility model trained on a quarter of the study area and tested on the remaining three quarters. In the initial empirical model, we see AUC values of 0.54 in Hokkaido, 0.70 in Nepal and 0.52 in Lombok, and RMSE values of 0.11, 0.08 and 0.05 respectively. In almost all cases, adding SAR data improved model performance in terms of AUC, with

the biggest improvement observed when the first ALOS-2 image was added. The addition of this first ALOS-2 image also resulted in a decrease in RMSE for each case study region. The biggest improvement was seen in Hokkaido, where the addition of this ALOS-2 image resulted in a decrease in RMSE from 0.11 to 0.10, and an increase in AUC from 0.54 up to 0.88.

The model to which only ALOS-2 data were added outperformed the model to which only Sentinel-1 were added, but the addition of Sentinel-1 data did result in a general improvement in ROC AUC in all cases, and these data are often available earlier than ALOS-2, as Sentinel-1 has a more frequent revisit interval than ALOS-2. The best-performing model in almost all cases incorporated both ALOS-2 and Sentinel-1 data. The addition of SAR data acquired within 2 weeks following the earthquake, which has been identified as a critical timeframe in emergency response (Williams et al., 2018), led to an increase in AUC from 0.54 to 0.95 in Hokkaido, from 0.70 to 0.82 in Nepal and from 0.52 to 0.65 in Lombok.

This improvement in performance can also be observed visually in Figure 5.3, which shows the initial model results without SAR, the model using all of the SAR data acquired within the first two weeks, and the final model using 4 Sentinel-1 images and 2 ALOS-2 images. The improvement is most obvious in the case of Hokkaido, however in Nepal, there is a clear reduction in noise in the southern part of models using more SAR data, and an increase in signal strength along the Langtang valley, where a large number of landslides took place (labelled on Figure 5.3). In Lombok, there appears to be a strong false positive signal immediately around the volcanic crater, which may be due to the steep slopes at this location, but the addition of SAR data still resulted in a modest improvement in comparison with the initial model.
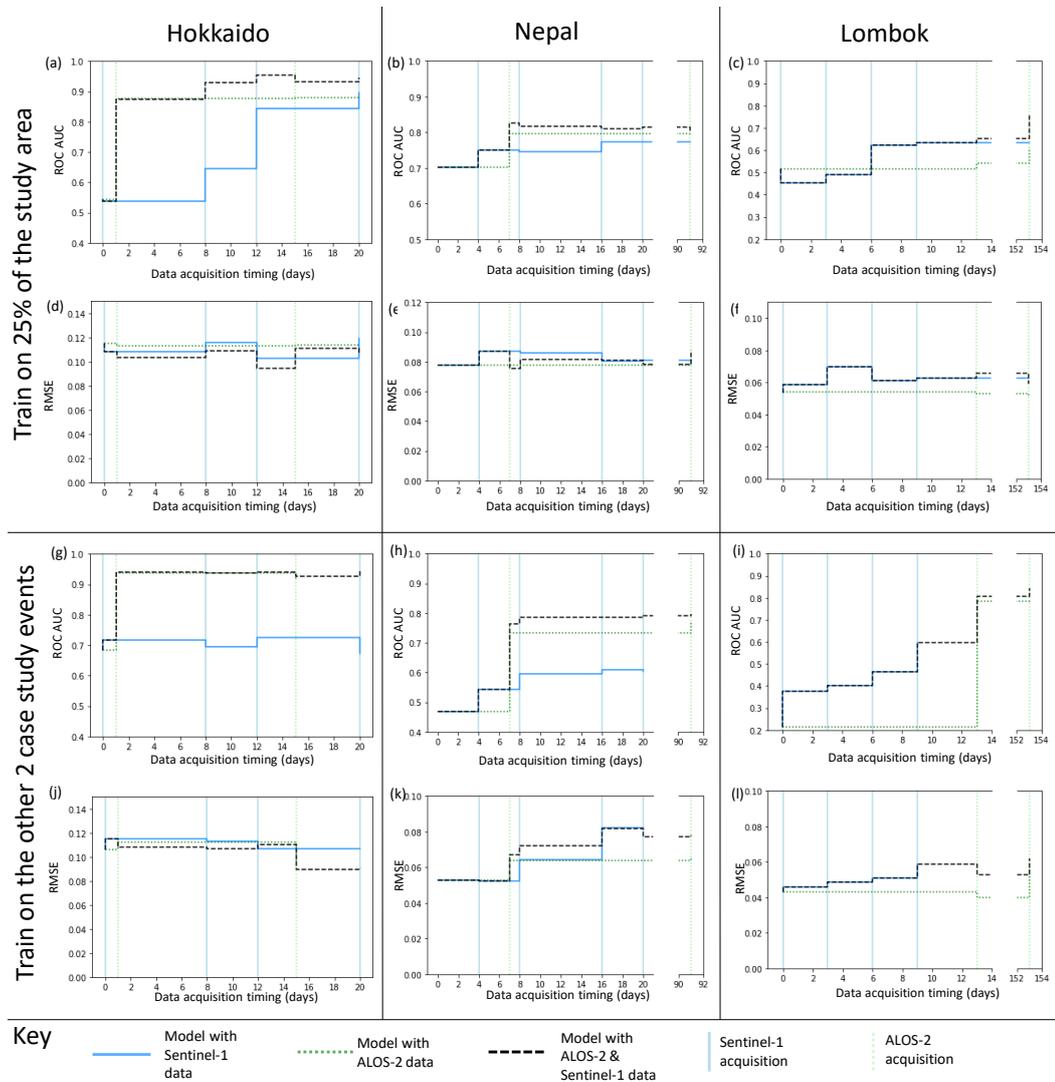
Figure 5.2: Step plots showing the change in ROC AUC (a-c, g-i) and RMSE (d-f, j-l) for each of the three events. Models in panels (a-f) were trained on a small part of each study area, while in panels (g-l) landslide areal density was predicted using a model trained on the other two case study regions in each case.
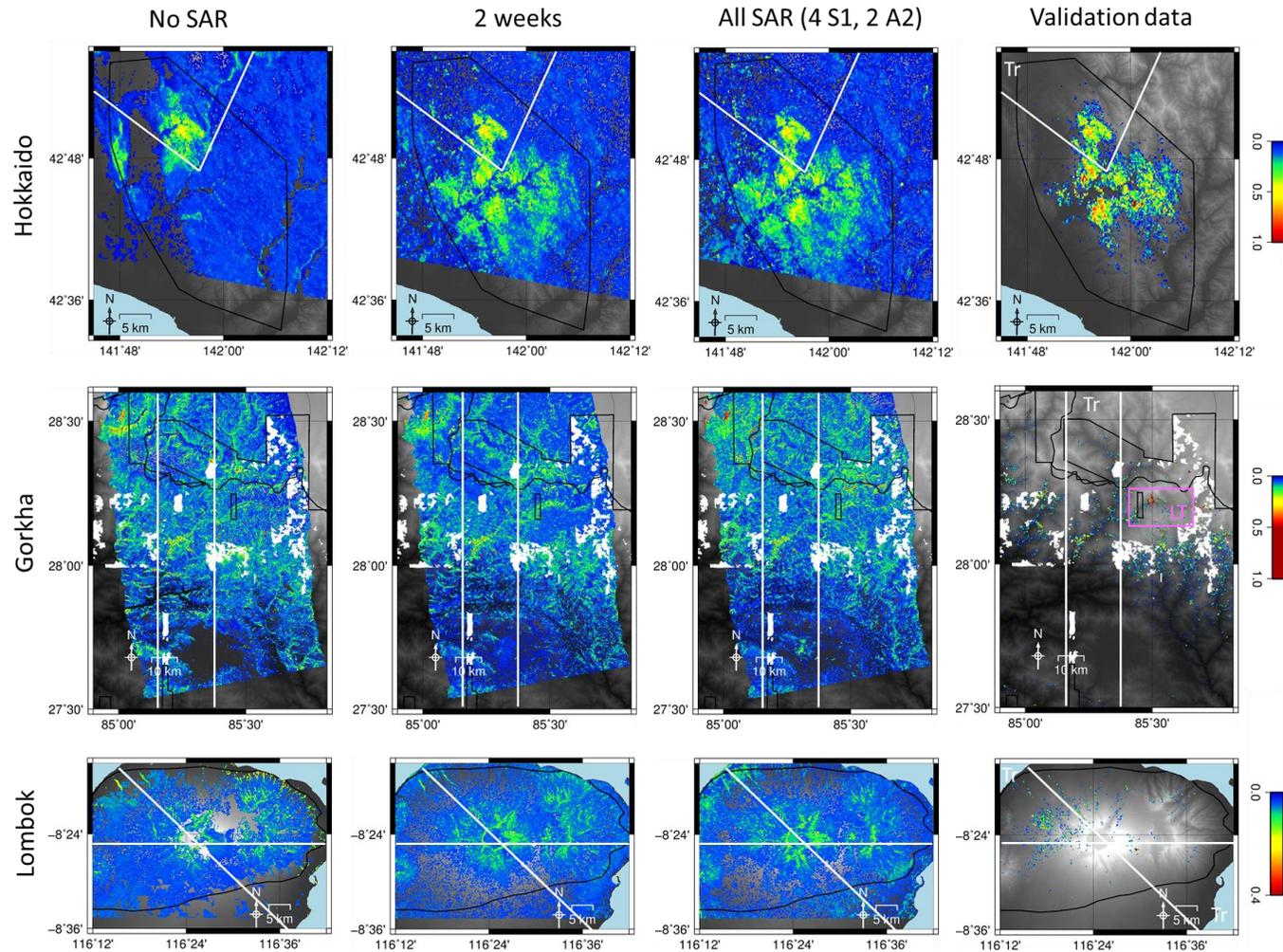
Figure 5.3: Timelines of modelled landslide areal density for each event, starting with no SAR data (left column). The second column shows the model using SAR data acquired within 2 weeks of the earthquake, and the third shows the model using all of the SAR data used in this study - 4 Sentinel-1 (S1) and 2 ALOS-2 (A2) in each case. The final column shows landslide areal density calculated from polygon inventories for each event (Ferrario, 2019; Roback et al., 2018; Zhang et al., 2019). The mapping extent of each of these inventories is shown by a black polygon. Areas that were used to train the model are outlined in white and marked "Tr" in the final column. The pink box marked "LT" on the final column of the Gorkha row shows the location of the Langtang Valley, which experienced particularly severe and large landslides following the earthquake.
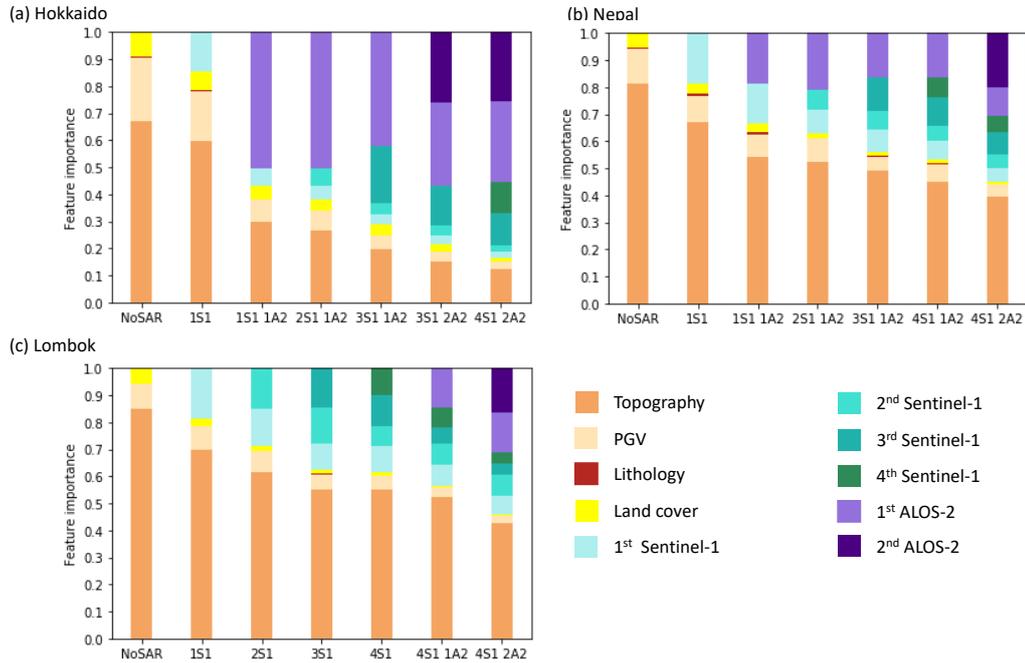
Figure 5.4: The relative importance of the different input datasets as SAR data are added to the model for models trained on a subsection of the study area.

Figure 5.4 shows the relative importance of each parameter in the model. For simplicity, the parameters have been grouped by the data required to create them, for example the importance of 'topography' on Figure 5.4 was calculated as the sum of the importances of maximum slope, mean slope, standard deviation of slope, elevation, standard deviation of elevation, relief and aspect. For each case study, topography was initially the most important input feature but its importance gradually decreased as more SAR data are added, particularly in Hokkaido, where it ceased to be the most important feature after the first ALOS-2 data were added to the model. In the final models, ALOS-2 data were consistently more important than Sentinel-1.

As described in Section 5.2.5, I ran ensembles of models trained on slightly different set of pixels in order to assess the variability in model output. An example of this for Hokkaido using three Sentinel-1 images and 1 ALOS-2 image is shown in Figure 5.5. The square root of the model variance is plotted in panel (d), and is highest in non-landslide areas of the model. The misfit, plotted in panel (c), shows that the model underpredicted landslide areal density in some areas and overpredicted it in others. There is an area to the west of the model, in which $\sqrt{variance}$ in panel (d) is relatively high and landsliding was overpredicted. This area corresponds to the town of Atsuma so may represent building damage due to the earthquake, which is known to affect SAR coherence (Yun et al., 2015). There is also an area
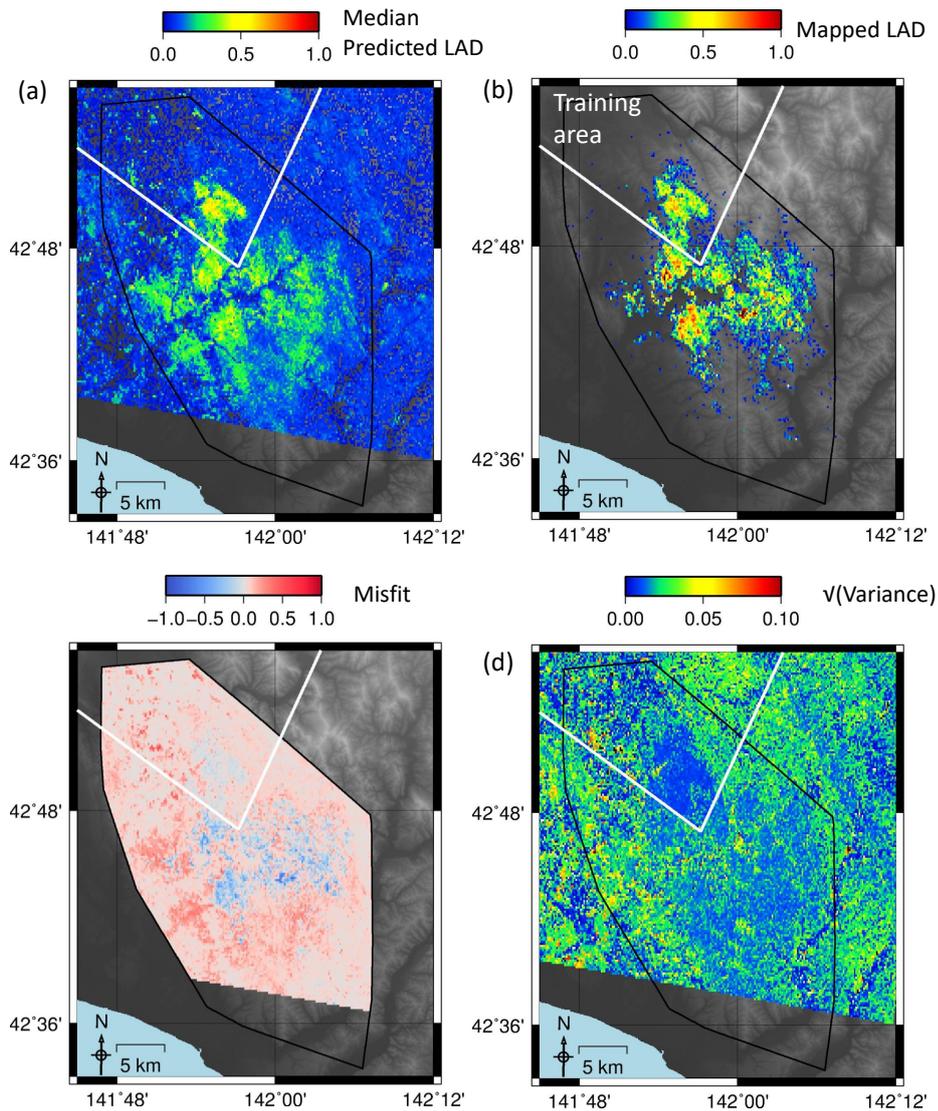
Figure 5.5: (a) The median modelled landslide areal density (LAD) for the M_w 6.6 Hokkaido earthquake using three Sentinel-1 images and 1 ALOS-2 image. (b) Validation dataset produced from the polygon inventory of (Zhang et al., 2019). (c) The misfit between the predicted landslide density in (a) and the mapped landslides in (b). (d) The square root of model variance.

of overprediction south of the main area of landslides, which corresponds to the area of false positives seen in the ALOS-2 data in Chapter 4, where I attributed it to wind damage associated with Typhoon Jebi. The areas of panel (b) which experienced the highest landslide areal density were underpredicted in the model. This reflects a potential problem with the application of Random Forest Regression to same-event landslide density prediction: the model cannot extrapolate and so no values can be predicted in the test area that are outside the range of those seen
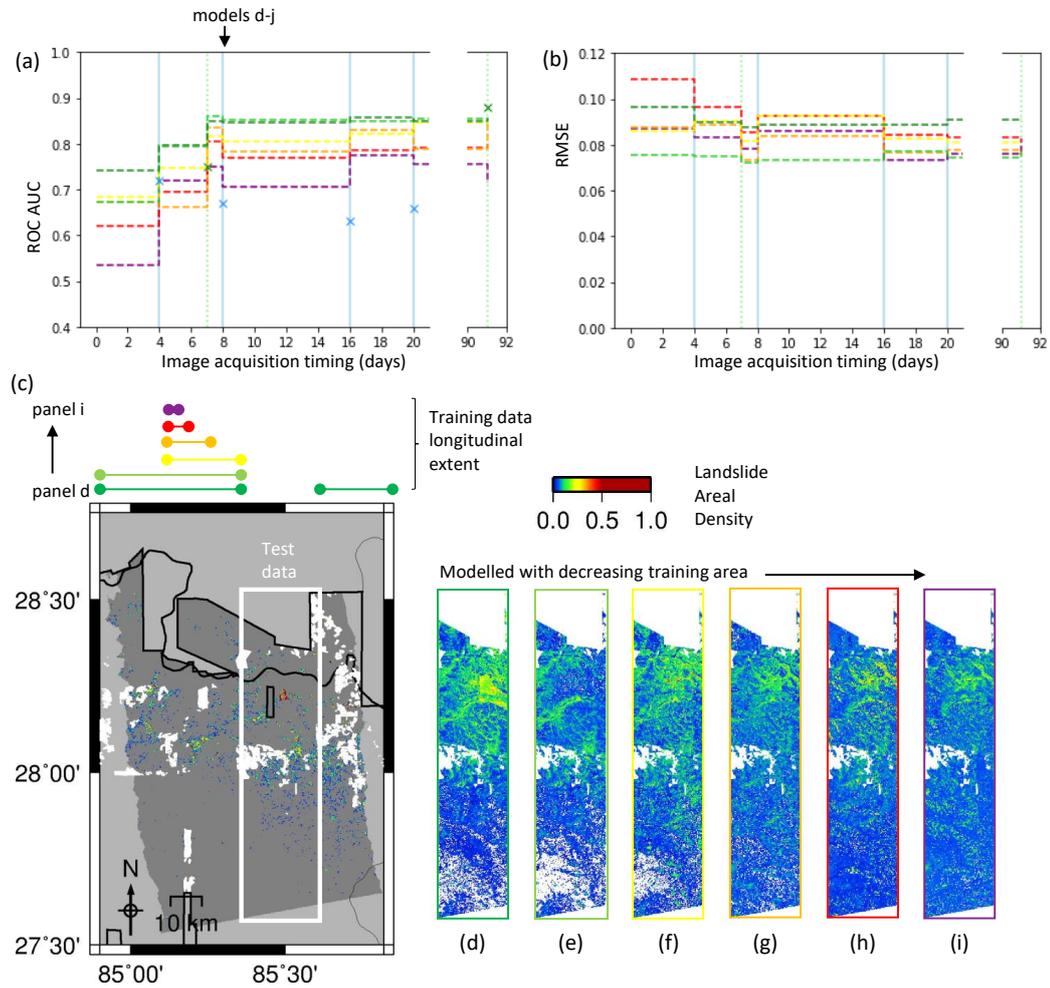
Figure 5.6: The effect of altering the extent of the training data in terms of ROC AUC (a) and RMSE (b). The clours of the lines in (a,b) correspond to the lateral extent of the training data marked on (c). (c) The mapped landslide inventory for the 2015 Gorkha earthquake of Roback et al. (2018), reproduced as landslide areal density for 200 x 220 m pixels. (d-i) Modelled landslide areal density with decreasing areas of data used for training the model.

in the training area.

5.3.1.1 What area of mapped landslides is needed to train the model?

The volume of data required to train any same-event model is key to its applicability in emergency response, due to the time required to generate these training data from optical satellite imagery. I used the Nepal earthquake to test this, as this event covered the largest area. I began with a training dataset using all of the data

outside the test area (Figure 5.6d), which contained 5,210 cells with landslide areal density $> 1\%$ across an area of 47 km^2, so that after balancing by undersampling the non-landslide cells (see Section 5.2.2), the training dataset comprised 10,420 cells. The model shown in (e) used only the data west of the training area (6,106 pixels after balancing across an area 21 km^2). From here, the longitudinal extent of the training data used was halved each time, resulting in balanced training datasets of 3,728 (f), 1466 (g), 538 (h) and 180 (i) cells.

Figure 5.6a clearly shows that models trained on a smaller area have lower AUC values, which is to be expected, and generally a similar effect on performance is seen in terms of RMSE in panel (b). However, as more SAR data were added to the model, the difference in AUC and RMSE between the best and worst models decreased. Panels (d-i) show the model using all SAR data acquired in the first two weeks following the earthquake (two Sentinel-1 images and 1 ALOS-2). Noise in the northern area of the model increases from e-i, and the signal strength where the landslides are decreases. However, panel (d), in which the model was trained on all of the available data (plotted in dark green on panels (a,b)) appears noisier than panel (e), in which only data to the west of the test area were used.

5.3.2 Global models

An alternative to training on a small part of the affected area is to train the model on landslide inventories from past earthquakes. To test the effect that SAR data might have on such models using my three case studies, I trained models on two earthquakes and predicted the landslide areal density triggered by the third. Figure 5.2 shows the effect on model ROC AUC (panels g, h, i) and RMSE (panels j, k, l) of adding ALOS-2 and Sentinel-1 SAR data to the input features used in training the model. A reasonable initial model of the Hokkaido was obtained with an AUC value 0.68, but the initial models in Lombok and Nepal were both extremely poor with AUC values < 0.5, indicating a model performance worse than random. In most cases, adding SAR data improved model performance in terms of AUC. However, the majority of SAR additions worsened the model in terms of RMSE in Nepal and Lombok. As in section 5.3.1, the biggest improvement was seen when the first ALOS-2 image was added to the models, and the best performing model overall incorporated both Sentinel-1 and ALOS-2 imagery.

5.3.3 Do these models outperform individual SAR methods ?

To assess whether a combined model of SAR and static landslide susceptibility input features is useful, it is necessary to compare it to the information that could

be obtained from SAR alone. The case studies and SAR data I used in this chapter are the same as those I used in Chapter 4 to systematically assess the performance of SAR coherence methods. I calculated AUC values at the same resolution and with the same definition of a landslide or non-landslide aggregate cell, and so the results presented in this chapter are directly comparable to those presented in Chapter 4. To assess the value added to the SAR methods by the static landslide predictors (lithology, PGV ets.), I also applied the Random Forest modelling technique using only the SAR coherence surfaces. Figure 5.7 shows AUC and RMSE values for the combined model, a SAR-only model, and the best performing SAR coherence surface at each point in time from Chapter 4.
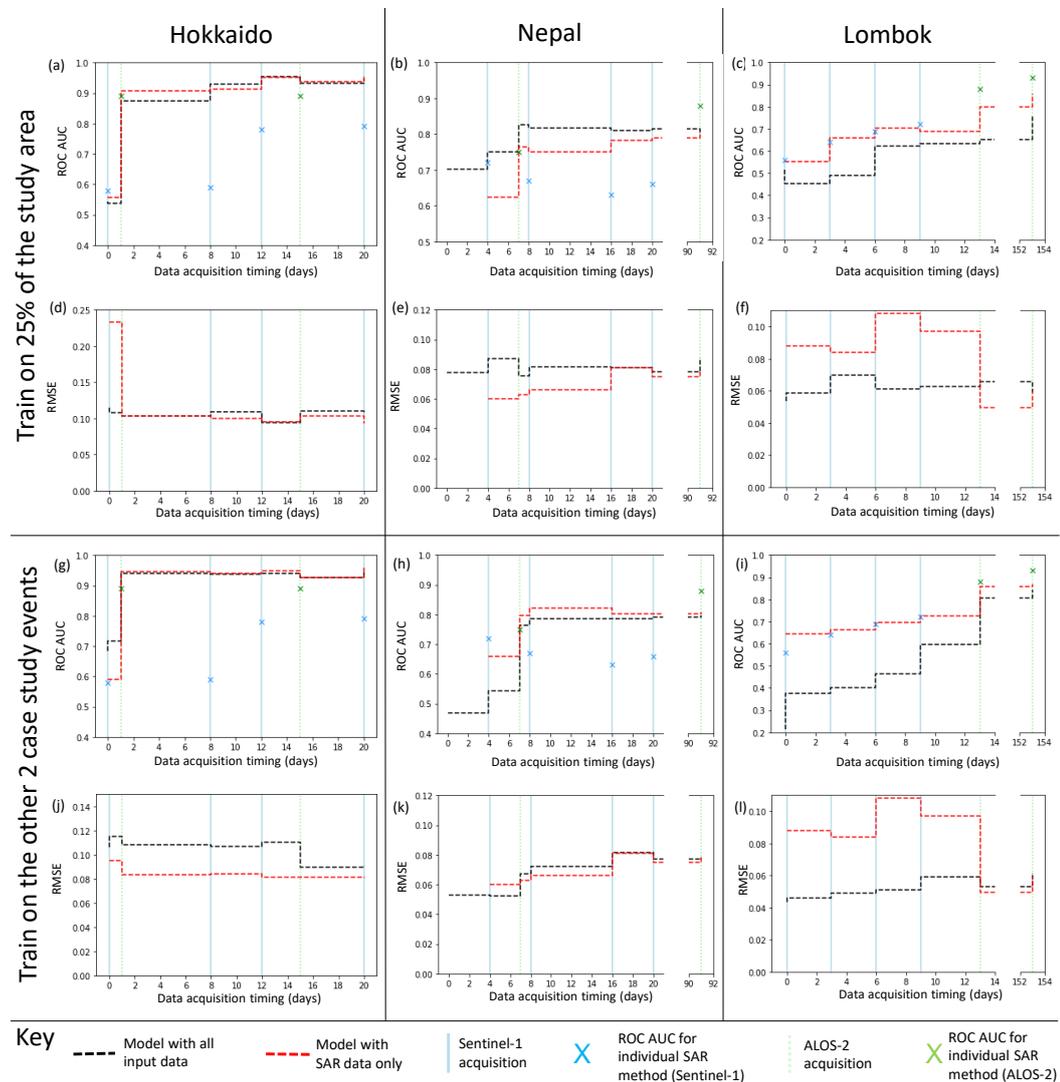

Figure 5.7: A comparison between the performance of individual SAR methods (blue and green crosses), a combined model using all input data listed in Section 5.2.6 (black line), a model omitting PGV (orange line) and a model using available SAR data alone (both Sentinel-1 and ALOS-2, red line)

For models trained on 25% of the affected area (Panels a-f), the combined model clearly outperformed the SAR-only model in the days after the earthquake in terms of ROC AUC in Hokkaido and Nepal and RMSE in all three cases. In Nepal, the difference in performance between the two models decreased as more SAR data were added. Both models outperformed the individual SAR methods at almost all stages in Hokkaido and Nepal. In Lombok, the SAR-only model performed better than the combined model in terms of AUC. The individual SAR methods had similar AUC to the models when only Sentinel-1 was available, and outperformed the models when ALOS-2 data became available. However, in terms of RMSE, the combined model consistently outperformed the SAR-only model.

For the global models, the SAR-only model outperformed the combined model in most cases in terms of ROC AUC in Nepal and Lombok, and had a similar performance in Hokkaido after the first ALOS-2 image was added. In terms of RMSE, the relative performance was more mixed, with the SAR-only model outperforming the combined model in Hokkaido, the models performing similarly in Nepal and the combined model outperforming the SAR-only model in Lombok. The SAR-only model had similar AUC values to the individual SAR methods presented in Chapter 4 in Lombok, and outperformed them in most cases in Hokkaido and Nepal.

5.4 Discussion

5.4.1 The same-event models

In Section 5.3.1, I demonstrated that the performance of a same-event Random Forest model of landslide areal density could be improved by incorporating SAR data. For each of the three events tested here a good model could be generated by incorporating SAR data acquired within two weeks of the earthquake, which means this could be implemented within an emergency response timeframe. In this section, I briefly discuss some factors which influence the applicability of these models.

5.4.1.1 Selection of the training data for the same-event model

The selection of training data for the same-event model directly affects the time taken for these data to be generated and so the applicability of the model to emergency response. In Section 5.3.1.1, I assessed the effect on model performance of changing the area used to train the model for Nepal, but did not consider differ-

Table 5.3: ROC AUC values for a model trained on a balanced set of 500 pixels randomly selected from across the target area.

Event	ROC AUC (initial model)	ROC AUC (2-week model)
Hokkaido	0.59-0.71	0.85-0.92
Nepal	0.65-0.78	0.79-0.84
Lombok	0.69-0.83	0.84-0.92

ent possible mapping strategies that could be applied in an emergency response situation.

The static same-event empirical model of Robinson et al. (2017), which is based on fuzzy logic theory, achieved AUC values in the range 0.76-0.87. It is not possible to directly compare AUC values between studies with different model outputs, ground truth data and spatial resolutions. However, it is clear that the model of Robinson et al. (2017) performed well, while in Hokkaido and Lombok, my initial model was extremely poor, with AUC values of around 0.5, which indicates a model with no skill at all. It may be that in the case of these two events, the area I chose to use as training data did not represent the entire study area well.

Robinson et al. (2017) found that a model trained on 250 landslides randomly distributed through the affected area performed well in the case of Nepal. This is an extremely useful result, as such a small number of training landslides could be mapped in a relatively short period of time after an earthquake. To test the improvement offered by SAR to a comparable model, I randomly selected 250 landslide and 250 non-landslide aggregate pixels across the whole mapped area and used these to train my model for each case study event, testing on the remaining pixels. I repeated this 10 times to obtain a range of AUC values which could be expected from such a model for each event. These are presented in Table 5.3.

There is a clear improvement in the initial model in Hokkaido and Lombok in comparison to the models trained on a coherent quarter of the study area (Section 5.3.1). As in Section 5.3.1, there is a significant increase in AUC when the SAR data available in the first two weeks are incorporated into the model, at which point the AUC values in Table 5.3 are similar to those in Figure 5.2 in Hokkaido and Nepal, and higher in Lombok. This demonstrates that the value added to the empirical model by the SAR data also applies when the model is trained on data distributed across the study area. The observation that the performance of the initial model for Hokkaido and Lombok was significantly poorer in Section 5.3.1 than in Table 5.3, but that the models incorporating SAR performed more similarly in both model setups may demonstrate that when SAR data are added to the model, it becomes less sensitive to how clustered the training samples are. This

clustering effect was observed to be detrimental to model performance by Robinson et al. (2017), but it is often necessary for training landslides to be clustered when only small parts of the affected area are visible through gaps in cloud. Therefore if the addition of SAR data lessens this effect, it would be a significant advantage in applying same-event models

5.4.1.2 Training data format

The landslide areal density data I used here to train the model were calculated from polygon inventories. These inventories are extremely time-consuming to produce and are unlikely to be available during an emergency response. The model of Robinson et al. (2017) was trained on point-mapped landslide data, which can be generated much more quickly following an earthquake. However, the overall spatial distribution of landslide number density, which can be calculated from point-mapped landslides, and the landslide areal density used here are generally very similar (e.g. Ferrario, 2019). Thus I expect that the improvement observed in the models tested here when SAR data were added should be transferrable to models trained on landslide number density and therefore applicable in emergency response.

5.4.2 Towards a global landslide prediction model

The advantage of a global landslide prediction model, such as those of Nowicki Jessee et al. (2018) and Tanyas et al. (2019), is that there is no need to map any of the landslides triggered by an earthquake before a model of their likely spatial distribution and impacts can be produced. All of the model inputs used here are available globally, and thus could be extended to a global model. However, my 'global' models were trained on only two events, and as such were not expected to perform well. In particular, the initial models for Lombok and Nepal performed very badly, with ROC AUC below 0.5, which is not representative of the performance of similar models trained on a global dataset of earthquakes (Nowicki Jessee et al., 2018; Tanyas et al., 2019; Thompson et al., 2020).

In the case where categories of lithology or land cover are present for one event but absent from the other two, my "global" model will not have captured their effect on landslide likelihood. Furthermore, the unusually high landslide density on shallow slopes in Hokkaido, could result in bias when this event makes up half of the training data, particularly as topography is the dominant feature in the model before any SAR data are added (Figure 5.4). I attribute the poor performance of the combined

model in comparison to the SAR-only model in Lombok and Nepal to this effect (Figure 5.4h, i, k, l). This may also explain the failure of Masato et al. (2020) to predict the landslides triggered by a rainfall event in Kyushu using a model trained on the Hokkaido landslides despite the fact that the reverse worked well. I therefore expect the performance of the initial models to improve for a model trained on more events, particularly as working global landslide susceptibility models have already been developed without SAR data (e.g. Nowicki Jessee et al., 2018).

However, the addition of SAR data to my 'global' models improved their ability (Figure 5.2g-j), which suggests that a similar model trained on more events could perform very well. The addition of the SAR data would be particularly useful in the case of complicated events, such as Hokkaido, where landslides were triggered by both rainfall and an earthquake (Zhang et al., 2019). The training and testing of my model was limited to landslides in vegetated areas. Due to significant differences in background coherence between arid and vegetated regions (Section 2.4), it is likely that separate models would be required for vegetated and arid regions of the world. It is unknown whether the models could be trained and applied equally well in arid regions. However, based on my results here, the advantage of incorporating SAR data in landslide models of vegetated regions could be significant and is worth exploring in the future.

5.4.3 Future possible SAR inputs

Although here I limited the SAR inputs to coherence-based landslide detection methods, there are other options which could be beneficial. The first of these would be the amplitude of the SAR signal, which is also sensitive to landslides. As amplitude is not calculated from multiple pixels, it can be used to obtain information at a higher spatial resolution than coherence. In Section 2.5, I described a number of studies who demonstrated that a number of methods based on SAR amplitude had some skill in landslide detection (Ge et al., 2019; Konishi and Suga, 2018, 2019; Mondini et al., 2019). There have also been three studies, which successfully combined surfaces derived from amplitude and coherence to detect landslides triggered by the Hokkaido earthquake (Aimaiti et al., 2019; Ge et al., 2019; Jung and Yun, 2019), suggesting that amplitude methods may be beneficial to my model. However, amplitude depends on several factors including soil moisture content and slope orientation relative to the satellite sensor. Landslides can therefore result in both increases and decreases in amplitude, and false positives can easily arise. Amplitude change is thus not usually reliable in landslide detection (Czuchlewski et al., 2003; Park and Lee, 2019).

A second option would be polarimetric SAR, in which data are recorded by the SAR satellite at two polarisations (dual-pol) or both projected and recorded at two polarisations (quad-pol). Polarimetric SAR data thus describe the scattering properties of the Earth's surface more completely than the single-polarisation data I have used here (See Section 2.1.3). It has been demonstrated that quad-pol data can be used to map landslides (Czuchlewski et al., 2003; Masato et al., 2020; Park and Lee, 2019). However, few SAR systems acquire quad-pol data, and those that do (e.g. ALOS-2) do not acquire them routinely. Therefore these data are often not available immediately after an earthquake. The applicability of dual-pol SAR data to landslide-detection is less well explored, but as these data are acquired more commonly and are routinely acquired by Sentinel-1 they are likely to be available following an earthquake and so could be incorporated. When testing a range of polarimetric parameters that could be used in landslide detection, Park and Lee (2019) demonstrated that landslides could be identified in surfaces generated from dual-pol data, although using dual-pol methods resulted in more noise than quad-pol. Thus, when combined with the other landslide detection and susceptibility parameters used in this study, dual-pol Sentinel-1 data may offer an additional benefit.

It is also worth considering which SAR satellites could provide data to be incorporated into empirical models. Here I used two tracks of Sentinel-1 data and one of ALOS-2. ALOS-2 data are acquired at a longer wavelength than Sentinel-1 (L-band rather compared to C-band), so the data retain a higher coherence in vegetated areas, a significant advantage in landslide mapping. It is therefore unsurprising that the addition of the first ALOS-2 image to the models offered the greatest improvement to prediction of landslide areal density in the majority of cases I considered here. The ALOS-2 satellite system has a 14-day repeat time and one of the aims of the mission is to enable emergency response, so this first ALOS-2 image is very likely to be available within two weeks of an earthquake. However, I found that in almost all cases, the addition of Sentinel-1 data also offers an improvement to the model, and these data are often available sooner after an earthquake than ALOS-2. Thus I would recommend the use of both datasets in the case where the added data processing and storage capacity are easily available.

It is also important to note that the limited swath width of the ALOS-2 data used here (50 - 70 km, compared 250 km for Sentinel-1) is a disadvantage for earthquakes that trigger landslides across a large area. For example, in the Nepal earthquake, the ALOS-2 scene I used in this study covers less than half of the landslides that were triggered by the earthquake (Figure 4.1a). Therefore, in order to obtain a complete model of a landslide event of this spatial extent, it would be necessary

to combine several adjacent scenes, which are likely to be acquired on different days. Here I did not test whether a model trained on one SAR scene could be then applied for the same event using data from an adjacent scene, or whether it would be necessary to map landslides from within every scene for the purpose of training the model. However, the relative success I have had in training on two events and testing on a third, which is a significantly more difficult problem, suggests that this might be possible.

In the future, the planned NASA-ISRO NiSAR mission, which is due to launch in 2022, may offer a solution to the limited swath width of ALOS-2 data. NiSAR will also obtain L-band SAR data, but with a wider swath width of 240 km (Sharma, 2019). The NiSAR mission will acquire data continually with a 12 day repeat time. Thus, after the launch of this satellite system, it may be possible to use both ascending and descending tracks of L-band SAR data, rather than just one track as I have used here.

5.4.4   Possible application to rainfall-triggered landslides

Here I based my models on an initial model designed to predict the locations of earthquake-triggered landslides based on, for the most part, topography and peak ground velocity, and demonstrated that the addition of SAR data could improve the performance of these models. Landslides can also be triggered by rainfall events, and as with earthquake-triggered landslides, cloud cover can cause significant problems with mapping landslides using optical satellite imagery. In particular, long rainfall events such as the monsoon in Nepal are associated with almost continuous cloud cover for several months (Robinson et al., 2019). This means that it is currently extremely difficult to obtain landslide information beyond that predicted by static empirical models such as that of Kirschbaum and Stanley (2018).

Landslides in vegetated regions are likely to result in decreased coherence regardless of their triggering mechanism due to associated movement of material and vegetation removal, which alters the microwave scattering properties of the Earth's surface. Therefore, it seems likely that the added prediction ability that can be gained by adding SAR to static models of earthquake-triggered landslide susceptibility could also apply to models of rainfall-triggered landslide susceptibility.

5.5   Conclusions

In this chapter, I have tested the relative performance of SAR-coherence-based classifiers, empirical landslide susceptibility models and a combination of these. I

found that adding SAR data to the empirical landslide susceptibility models improved their ability to predict landslide areal density after large earthquakes. The largest improvement was seen when the first ALOS-2 data acquired following the earthquake was added to the model, but the best performing model incorporated both Sentinel-1 and ALOS-2 data. Importantly, a significant improvement was seen using SAR data acquired within two weeks of each case study earthquake, meaning that the improvement to the initial model could be made quickly enough to be used in emergency response. Although I did not use enough case study events here to generate a comprehensive global model, it appears that SAR data are also beneficial in this case, although further case study regions would need to be tested, and such a model might have to be limited to vegetated areas.

CHAPTER 6

Discussion

6.1 Synopsis

In Chapter 1, I set out three key aims of this thesis, which would allow SAR coherence methods to be applied more widely for landslide detection for emergency response:

1. The development of new SAR coherence methods targeted at landslide detection.

2. Systematic testing of SAR coherence methods across different SAR datasets and case study events.

3. Integration of SAR coherence methods with empirical models of landslide susceptibility.

First, when I began this project, the only SAR coherence method that had been applied to landslide detection was to use the decrease in coherence of a co-event interferogram relative to a pre-event interferogram (The ARIA method; Yun et al., 2015). This method was developed for use in building damage detection, so I wanted to examine whether it could be improved upon for application to landslides. In Chapter 3, I presented a new method for landslide detection, in which the difference between two different spatial estimates of coherence is used for landslide detection (The Bx-S method). I tested this method using Sentinel-1 SAR data for the M_w 7.8 2015 Gorkha, Nepal Earthquake, and demonstrated that in this case, the Bx-S method offered a significant improvement in landslide detection ability compared to existing methods. Furthermore, in Chapter 4, I presented another three new coherence-based methods which make use of additional post-event SAR imagery (PECI, ΔC_sum, ΔC_max). These take advantage of the fact that the bare rock exposed by a landslide has a high coherence in a post-event interferogram (Section 2.4). These methods also outperformed existing methods, although

the additional waiting time for a second post-event image is a disadvantage in emergency response.

The second problem I raised in Chapter 1 was that, while a range of SAR coherence methods for landslide detection have been developed, in most cases they have been tested on a single event using data from a single SAR sensor. Therefore there has been no systematic testing across different events and sensor types. In Chapter 4, I tested five methods (ARIA, Bx-S, PECI, ΔC_sum, ΔC_max) using ALOS-2 PALSAR-2 (L-band) and Sentinel-1 (C-band) data on four landslide inventories. I found that, while SAR data could be successfully used to identify landslides triggered by the four events, the best performing method depended on the SAR data available. The best performing method with a single post-event image was the ARIA method with ALOS-2, but in most cases, Sentinel-1 data were available first, and in this case the Bx-S method performed best. Methods incorporating a second post-event image (PECI, ΔC_sum, ΔC_max) performed more consistently and in most cases better across events than methods using only one post-event image. Again with these events, ALOS-2 data performed better than Sentinel-1. Thus Chapter 4 allowed me to make recommendations on which method to use according to what data are available after an earthquake.

Finally, SAR coherence methods and empirical models of landslide likelihood both offer an alternative to manual-mapping with optical satellite imagery. In Chapter 5, I assessed the contribution that SAR data could make to empirical models of landslide detection by combining SAR-coherence-based classifiers with static predictors of landslide likelihood, such as topographic slope and ground shaking estimates using Random Forest Regression. Here I demonstrated that adding SAR coherence data to empirical models offered an improvement to model performance, with the biggest improvement seen when the first L-band image was added. These combined models also outperformed the individual SAR coherence methods.

6.2 Application of SAR coherence methods to future events

My thesis shows that SAR coherence methods have great promise for the detection of landslides triggered by future earthquakes in vegetated regions. I have demonstrated that at a resolution of around 200 m, landslide information can be generated from SAR within two weeks of an earthquake, a critical time for emergency response coordination (Williams et al., 2018). One important question that remains to be considered is what SAR data will be available within this timeframe

in the future?

In terms of C-band SAR, the constellation producing the largest volume of data is the Sentinel-1 system operated by ESA, whose imagery I used in this thesis. This constellation has a repeat time of 12 days globally and 6 in Europe, meaning that C-band imagery a few days after an earthquake is almost guaranteed. The first of these satellites, Sentinel-1a was launched in 2014, followed by Sentinel-1b in 2016. These are expected to operate for between 5 and 10 years, and will be replaced by Sentinel-1c and -1d, which are already being prepared (Torres et al., 2017). Therefore it seems likely that the availability of C-band SAR data will remain high in the years to come. These data are openly available online soon after acquisition.

L-band SAR performed better than C-band in this study, both in terms of SAR coherence methods in Chapter 4, and the improvement offered to empirical models with SAR data in Chapter 5. This is unsurprising, as my research has focussed on landslides in vegetated regions and L-band SAR is known to be less sensitive to vegetation-related decorrelation (See section 2.4 for details). Currently, the acqsution strategy of Sentinel-1 means that C-band SAR imagery is acquired much more regularly than L-band, and in several cases the L-band interferograms I have used in this study had to be formed from images acquired several weeks or months apart. In Nepal and Lombok, the methods in Chapter 4 relying on a second post-seismic image could not have been applied within the emergency response timeframe ($\sim$2 weeks, Section 1.1) due to the delay before the acquisition of the second image. Furthermore, with the exception of track A018d in Hokkaido, the L-band data used here did not give complete coverage of the triggered landslides, which would be a significant disadvantage if applying these data to a new event. However, in the future, the launch of the L-band NASA-ISRO NiSAR and ESA ROSE-L missions, planned in 2022 and 2026 respectively, will greatly increase the availability of L-band SAR data (Pierdicca et al., 2019; Sharma, 2019). The planned acquisition strategies of these missions will also provide data with a wider swath width than the ALOS-2 PALSAR-2 data used in this study (240-250 km compared to 30-70 km), making it more likely that the L-band imagery acquired following an earthquake will cover the entire area affected by triggered landslides. These data will also have a similar open-access strategy to Sentinel-1 so will be freely available to download.

6.2.1 Implementation in an emergency response setting

In an emergency response setting, there are some extra steps that would need to be carried out, and some further work required before the landslide detection methods

I have presented in this thesis could be applied. First, the approximate limits of the area possibly affected by landslides need to be established. The simplest way to do this would be using ground shaking estimates, which are published on the USGS website within hours of all large earthquakes. With this area established, it will be possible to identify C- and L-band SAR tracks which cover this area and to establish when data on each track will be acquired. Although covering a larger area will require more SAR data to be processed and stored, it would be advisable for this estimate to be relatively generous as the initial shaking estimate is not always representative of the true extent of the shaking (e.g. Dixit et al., 2015) and the exclusion of an area that is later found to have been badly damaged by landslides could lead to this area being neglected in the emergency response.

The next step is to decide which method to use. The methods I have worked on in this thesis can be divided into two categories: the SAR-coherence-based methods in Chapters 3 and 4 and the combination of SAR coherence and empirical modelling in Chapter 5. The outcomes of these two would be different and there are advantages and disadvantages to each.

The methods in Chapters 3 and 4 could be used to generate a landslide intensity proxy map similar to the building damage proxy maps currently generated by the NASA ARIA project using SAR coherence (Yun et al., 2015). In these maps, damaged pixels are coloured according to their signal strength and undamaged pixels are left uncoloured, which requires a threshold between damaged and undamaged to be set. To establish a similar threshold between 'landslide' and 'non-landslide' pixels, there are two questions to answer. First, to what extent do we want a pixel to have been impacted by landsliding before it is classed as 'landslide'. This is important, since in Chapter 3, I demonstrated that more severely impacted pixels could be detected with greater accuracy. Second: is it possible to identify a threshold, or a method to calculate a threshold that is reliably transferrable between events? To answer this will require investigation of more events.

It would also be helpful to identify areas where the ability of the applied SAR coherence method is likely to be poor, such as urban or snow-covered areas (Section 4.4.2), and to mask and label these in any products supplied to emergency response coordinators. In Chapter 4, I gave a set of recommendations on when each method should be used depending on the available SAR data. However, there is a question over at what point the methods become useful. With only a single Sentinel-1 image, the best performing method (The Bx-S method) had ROC AUC values ranging from 0.55-0.74, which is not reliable enough, and would probably not offer an improvement compared to empirical models (e.g. Nowicki Jessee et al., 2018). In Nepal, the accuracy of this method was improved by decreasing the spatial

resolution (An improvement of ROC AUC from 0.59 up to 0.75 when the output resolution was decreased from 20 m × 22 m to 300 m × 330 m), but more testing would be required to see whether sufficiently consistent and high accuracy could be obtained from a single Sentinel-1 image at lower resolutions, for example at the 1 km^2 resolution often used in landslide susceptibility model (e.g. Nowicki Jessee et al., 2018). At present, when applying the methods tested in Chapter 4 it would be better to wait for either an L-band image of the affected area or for a pair of post-seismic Sentinel-1 images.

Combining SAR methods with empirical modelling, as in Chapter 5, would have several advantages over applying the methods individually. First, in terms of ROC AUC, the modelled surfaces in Chapter 5 are higher than the individual methods in Chapter 4. Second, predicted landslide density is more easily understood than the landslide intensity proxy discussed in the previous paragraph. Third, the modelling process allows ascending and descending tracks to be combined so that it is not necessary to mask slopes that are unfavourably orientated to the satellite and so not imaged well (e.g. Section 3.2.2.4). This means that the landslide areal density model of Chapter 5 is more complete than the products I presented in Chapters 3 and 4. The disadvantage to the combined empirical modelling approach is that, for the same-event model, some landslide mapping within the affected area is required to identify some of the landslides triggered by the earthquake that can then be used to train the model. This requires some availability of cloud-free optical imagery and the time and manpower to map the landslides. This would not be necessary for a global model. In Chapter 5, I found that a global model appeared promising and it has been shown elsewhere that global empirical models perform well without the addition of SAR data (e.g. Nowicki Jessee et al., 2018; Tanyas et al., 2019) but more events would need to be included in the training dataset, and further testing will be required before this kind of model incorporating SAR could be rolled out.

6.3 Further research

6.3.1 The effects of varying landslide type

I did not attempt to draw any conclusions in this thesis on how the properties of landslides might affect their signal in SAR surfaces. Landslides can be divided into five main categories based on their movement: falls, topples, slides, lateral spreads and flows (Varnes, 1978). The landslides triggered by the four case studies used in Chapters 3, 4 and 5 were typical of landslides commonly triggered by earthquakes, with the majority of ground failures being slides of rock or soil, with shallow failure

surfaces (Collins and Jibson, 2015; Ferrario, 2019; Keefer, 1984; Yamagishi and Yamazaki, 2018). In Nepal, ground failures were primarily a mixture of slides and falls (Collins and Jibson, 2015). In theory, any landslide of sufficient area is expected to disrupt the Earth's surface, altering its scattering properties and resulting in a temporary coherence loss. However, since I have not attempted to test different types of landslides separately, and my analysis includes very few or no flow-, topple- or lateral-spread-type landslides, it is not certain that all types would have the same signal in coherence-based landslide methods. For methods of landslide detection based on SAR amplitude (e.g. Konishi and Suga, 2018), I would expect that landslides which strongly alter the orientation of a pixel to the SAR sensor by the removal or addition of material would have a stronger signal. Landslides that either alter the material detected by the SAR sensor, for example when vegetation is removed and bare rock is exposed, should also show up strongly in amplitude images, while, for example, a lateral-spread-type landslide may not result in such a strong signal.

The effect that landslide type has on different SAR-based detection is worth investigating for two reasons. First, if a SAR-based detection method is not capable of detecting all landslide types, this must be taken into account when interpreting any output, regardless of whether it is used for research or for emergency response. Second, if different landslide types have different signals in SAR data, it may be possible to draw information on landslide type from SAR, providing a more complete understanding of the effect that an earthquake has had on the landscape. In particular, it may become possible to derive information on landslide type using data from increasing numbers of high resolution SAR satellites, such as the recently launched commercial ICEYE SAR constellation, which has an azimuthal resolution of up to 25 cm (ICEYE, 2020). Therefore, while it was beyond the scope if this thesis, I believe it would be beneficial to investigate the SAR coherence and amplitude signals of different types of landslides.

6.3.2 Detection of rainfall-triggered landslides

My focus in this thesis has been on earthquake-triggered landslides. A large proportion of SAR-based landslide detection methods, particularly those using SAR coherence have also used earthquakes as case studies (Aimaiti et al., 2019; Ge et al., 2019; Jung and Yun, 2019; Konishi and Suga, 2019; Yun et al., 2015). Those applied to rainfall-triggered landslides often focus on individual large landslides (e.g. Czuchlewski et al., 2003; Mondini et al., 2019) as opposed to large-scale detection of landslides across a landscape, or use polarimetric SAR, which is not acquired after most events (e.g. Czuchlewski et al., 2003; Masato et al., 2020). However,

the application of large-scale, SAR-based landslide detection methods to rainfall triggered landslides would be advantageous for several reasons. There is an obvious correlation between rainfall and cloud cover, so that optical satellite imagery of rainfall-triggered landslides is likely to be obscured by cloud. Also, although earthquakes can trigger thousands of landslides, they occur relatively rarely, while some areas of the world experience rainfall-triggered landsliding every year.

The preference for testing on earthquake-triggered landslides is unsurprising. First, since it is common practice to use InSAR to map ground deformation after the earthquake, SAR data are commonly acquired and processed after an earthquake (NASA, 2018). In some cases, areas of landslides corresponding to areas of low coherence in an interferogram are obvious (e.g. Fujiwara et al., 2019; Vajedian et al., 2018), which would naturally encourage their use as landslide detection case studies. Satellites that are intended for use in emergency response, such as ALOS-2, are likely to acquire a SAR image following an earthquake for use in ground deformation measurements, but historically there has been no need to acquire SAR data after a rainfall event. This has only recently begun to change with the launch of Sentinel-1a in 2014. Currently, the Sentinel-1 satellites acquire either ascending or descending track SAR imagery every 12 days over all land masses globally, and both tracks over tectonic belts (ESA, 2019). This makes it far more likely that SAR data will be available for landslide mapping after a rainfall event. Second, ground shaking due to an earthquake generally lasts for less than a minute, and it can be assumed that landslides occur during, or shortly after this interval, which means that the timing of the landslides is already known, and in a time series of interferograms, we know which one to consider as 'co-event'. The majority of landslide-detection methods, including all of those I have presented here, require this information. They also require all landslides to occur in the same interferogram, which may not be the case, particularly for long rainfall events such as the Nepal monsoon. One solution to this could be to increase the time window of the interferogram, however this has an adverse effect on background coherence, particularly in vegetated regions. I gave an example of this in Chapter 4 when I compared the performance of the same methods on landslides triggered by a single earthquake in the 2018 Lombok earthquake sequence and on landslides triggered by the whole sequence.

A further complication of applying SAR coherence methods to rainfall-triggered landslides is that the rainfall itself can also affect the coherence. It has been demonstrated that rainfall can cause significant decorrelation of an interferogram as wet and dry soil have very different dielectric properties (Nolan and Fatland, 2003; Scott et al., 2017). Theoretically, this could be a significant problem when applying SAR coherence methods to rainfall-triggered landslides. However, the success in

detecting landslides triggered by the M_w 6.6 Hokkaido, Japan earthquake, which closely followed Typhoon Jebi, not only in Chapters 4 and 5 of this study, but also in various other studies (Aimaiti et al., 2019; Ge et al., 2019; Jung and Yun, 2019; Konishi and Suga, 2019) indicates that this may not be prohibitive, although this may not be the case in arid environments (Discussed further in Section 6.3.3).

Therefore, I expect that SAR coherence methods could be applied to rainfall-triggered landslides in vegetated regions. It will, however, be necessary to make some adjustments to existing methods to allow for the fact that the timings of landslides triggered by rainfall events are less certain.

6.3.3 Landslide detection in arid environments

The majority of studies of landslide detection using SAR coherence have been carried out in vegetated areas (Aimaiti et al., 2019; Czuchlewski et al., 2003; Jung and Yun, 2019; Konishi and Suga, 2018; GDAL/OGR contributors, 2020; Masato et al., 2020; Yun et al., 2015); very little work has been done in arid environments (e.g. Cabré et al., 2020; Olen and Bookhagen, 2018, 2020; Vajedian et al., 2018). The four case studies I used in this thesis were all located in vegetated areas. I made this choice for several reasons. First, regions where rain falls frequently are both more likely to support heavy vegetation and more likely to experience cloud cover following an earthquake. All the case studies I used occurred in an area of Asia considered likely to be obscured by cloud (Figures 1.3 and 1.6). Second, the removal of vegetation by a landslide is likely to result in severe decorrelation in an interferogram, so a strong signal can be expected in vegetated regions, and one that would be similar between my four case studies. Third, in order to evaluate a new method, a set of observations is required and more inventories of landslides in vegetated regions have been compiled from optical satellite imagery, as the contrast between the green vegetation and brown upturned soil makes them easier to map, particularly using multispectral optical imagery for NDVI (e.g. Borghuis et al., 2007). This final reason could also be motivation to explore the application of SAR to arid environments: although they are less likely to be obscured by cloud cover, landslides in arid environments are more difficult to map with optical satellite imagery (Barlow et al., 2015).

A landslide in an arid environment will move surface material around, but will not result in an entirely different material being exposed, as in vegetated regions. However, the movement of material downslope will still result in the movement and reorientation of scatterers, alter the roughness of the ground surface and potentially alter the wetness of the soil that is exposed to the SAR sensor, all of which

could result in temporal decorrelation of the image. Additionally, the absence of vegetation should result in higher background coherence, particularly when using C- or X-band SAR data. Vajedian et al. (2018) noted decorrelation of InSAR due to a small number of landslides triggered by the M_w 7.3 2017 Sarpol-e Zahab earthquake in Iran. Therefore, it may be possible to apply the methods developed here in Chapters 3 and 4 in arid environments, although the empirical models in Chapter 5 could probably not be trained on an event in a temperate environment and used to predict landslides in an arid environment.

If instead of earthquake-triggered landslides, we consider rainfall-triggered landslides in arid environments, another problem arises with applying SAR coherence methods: changes to the soil moisture content affect the SAR signal (Nolan and Fatland, 2003; Scott et al., 2017). As discussed in Section 6.3.2, this is not a major barrier to the application of SAR coherence methods in vegetated environments. However, in arid environments, it has been demonstrated that changes in soil moisture content can result in significant decorrelation of an interferogram (Nolan and Fatland, 2003; Scott et al., 2017). This discrepancy is likely to be due to the fact that in a pixel containing vegetation, some microwave energy will be scattered by the vegetation and will not interact with the soil beneath. Therefore, the effect of soil moisture on coherence is likely to be stronger in arid environments than in vegetated environments and, as discussed above, the decorrelation due to landslides may be less strong.

Using the ARIA method, or the methods presented in Chapter 4 that rely on a coherence change through time (PECI, ΔC_sum, ΔC_max), decorrelation due to soil moisture changes could lead to large areas of false positives. It's possible that the Bx-S method (Chapter 3) may be more useful in this case, removing large-scale coherence signals due changes in soil moisture content while leaving the signals from landslides. It has also been demonstrated that decorrelation due to a rainfall event is a transient effect. A co-event interferogram made up of one image acquired before the rainfall and one immediately after will be decorrelated since the soil is dry in the first image and wet in the second. However, if the second image is acquired a long time after the first and the water has evaporated, this decorrelation does not occur (Scott et al., 2017). Using this, Cabré et al. (2020) developed a method of differentiating between permanent coherence loss following a rainfall event due to erosion and debris flows, and temporary loss due to rainfall. While this study demonstrated that SAR coherence methods can be applied in arid environments for research purposes, when generating landslide information for emergency response, it is not practical to wait for months after the rainfall event for the ground to dry out.

Therefore, I expect that it will be possible to apply SAR coherence methods such as those developed here to landslides triggered in more arid landscapes. However the sensitivity of SAR coherence to rainfall in such settings will have to be taken into account, and it may not be possible to generate information on landslides that occur concurrently with a rainfall event quickly enough for use in emergency response. I also expect that systematic testing of SAR coherence-based landslide detection methods may be problematic due to the difficulty in mapping landslides in arid environments in optical satellite imagery. For example, Cabré et al. (2020) validated their method against data collected on a field campaign following the rainfall event, and Olen and Bookhagen (2018) do not validate their predicted landslide locations against any inventory of mapped landslides.

6.3.4 Generation of landslide information for research purposes

Here, my focus was on landslide detection for use in emergency response. For this, the aim was to generate an overview of landslide locations at relatively low resolution but across a large area within days of an earthquake. The information requirements of landslide inventories generated for research purposes are very different. A low-resolution overview of landslide locations is not likely to be sufficient for most research-based applications of landslide information. However, there are some advantages of SAR coherence methods that would be useful in a research setting.

Landslide mapping with optical imagery allows detailed maps of individual landslides to be produced. However, as with landslide mapping for emergency response, cloud cover can be problematic. A delay of days or weeks between an earthquake and useable optical imagery being acquired does not render the information useless as it does in emergency response, but it does mean that the landslide inventory produced from this imagery has poor temporal resolution. In some cases, where two or more trigger events occur in quick succession, mapped landslides cannot be attributed to one event or the other, as was the case for the 2018 Lombok, Indonesia earthquake sequence (Ferrario, 2019) and for some landslides mapped following the M_w 7.8 2015 Gorkha, Nepal earthquake, which was followed 17 days later by a M_w 7.3 aftershock (Martha et al., 2017; Roback et al., 2018). In such cases, SAR coherence methods could be applied to each earthquake, and could help to assign landslides to one event or the other even at lower resolutions than the optically-derived dataset.

6.3.5 Automatic landslide detection with SAR and optical satellite imagery together

SAR and optical satellite data are sensitive to landslides in different ways, and so using them together in landslide detection may allow the strengths of both to be combined. There are various ways that this could be done. In Section 6.3.4, I suggested that the high spatial resolution of optical satellite data and the high temporal resolution of SAR data make them suitable together for mapping landslides triggered by long rainfall events or sequences of rainfall. In Chapter 5, landslides mapped manually using optical satellite imagery were used to train a model which then used SAR methods to predict landslide density, which takes advantage of the high accuracy of optical satellite imagery, and the fact that SAR data can be acquired in all weather conditions.

Another option would be a combined automated landslide detection method using both optical and SAR imagery. The time-consuming nature of manual landslide mapping means that even in the case where cloud-free imagery is available, automatic methods would be beneficial in emergency response. Several studies have demonstrated that automatic landslide mapping using multi-spectral optical imagery can yield good results (e.g. Borghuis et al., 2007; Ghorbanzadeh et al., 2019; Heleno et al., 2016). As SAR and optical imagery represent independent measurements of the ground surface that are sensitive to landslides, there may be some advantage in combining these. For example, Borghuis et al. (2007) noted that dry riverbeds, roads and bare farmland were incorrectly identified as landslides as their signal in multi-spectral imagery was similar. These are not likely to have a similar signal to landslides in the coherence methods presented in this study. Similarly, possible changes in SAR coherence due to soil moisture changes would not have a signal in multi-spectral optical imagery (Nolan and Fatland, 2003; Scott et al., 2017). Therefore, providing that the SAR and optical satellite datasets can be georeferenced, a combined approach might lead to improved accuracy. Machine learning offers many viable options for combining such datasets. The Random Forests approach I applied to landslide detection in Chapter 5 could easily incorporate optical data as well. Alternatively, Ghorbanzadeh et al. (2019) compare several machine learning methods for combining topographic and multi-spectral optical data and suggest that (provided the model is well designed) a deep learning approach is likely to yield the best results.

6.4 Concluding Remarks

The generation of landslide information from SAR data would be extremely advantageous in an emergency response situation, as such data are now available within days of an earthquake anywhere on Earth in all weather conditions. However, research into this area has not previously been sufficiently advanced for these methods to be widely applied. Here, I have presented new methods of generating landslide information from SAR data, demonstrated that these methods are widely applicable in vegetated regions. I have made recommendations on when different methods should be used, which depend on the available data. Finally, I have demonstrated that incorporating SAR-based landslide detection methods into empirical models of landslide susceptibility can greatly improve their performance. When the research I present here is considered alongside other recent studies on this subject, it is clear that SAR data will greatly improve the availability of landslide data following an earthquake in the years to come. While the focus of my research was on the detection of earthquake-triggered landslides in vegetated regions for emergency response, the results are also likely to be relevant to those researching rainfall-triggered landslides or landslides in arid environments, and for generating landslide information for research purposes.

Appendix A: Assessment of Distorted SAR pixels

In Chapters 3 and 4, SAR pixels which are heavily distorted due to the imaging geometry of the SAR system relative to the slope direction are removed from the analysis, as these are likely to exhibit severe spatial decorrelation and so not be useful in landslide detection. In this appendix, I demonstrate how distorted pixels were identified and removed from the analysis, using data from Chapter 3

Figure A.1a shows a map of pre-seismic coherence (image pair 2015-04-05, 2015-04-17) for the region of Jharlang, Nepal. An example of a slope along which pixels have been distorted is indicated, where the pixels are visibly elongate and the image appears striped. In order to identify these distorted pixels, I calculated the geographic area which contributed to each pixel in radar geometry. Across the study area, this pixel contributing area ranged between 0 and 19,000 m^2. In contrast, each multilooked pixel in geographic coordinates is around 400 m^2 in size. I masked pixels with a contributing area above a given threshold. This threshold was incrementally lowered from 5000 m^2 to 2000 m^2 to 1000 m^2 (Figure A.1b, c, d respectively). With the threshold set at 1000 m^2, visibly distorted pixels were removed from the image (Figure A.1d). I therefore did not lower the threshold further, as this would have removed data without justification.

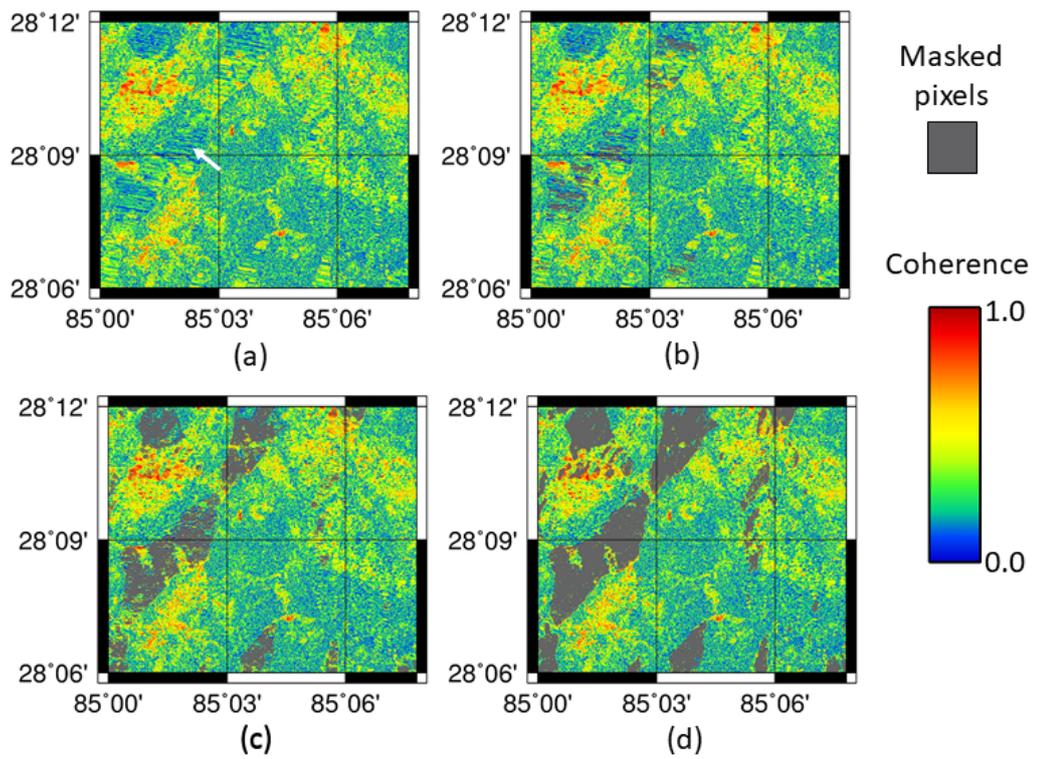Figure A.1: (a) Pre-event coherence map for Jharlang with white arrow indicating distorted pixels. (b, c, d) The effect of masking pixels for which the contributing area was over 5000, 2000 and 1000 m2 respectively

Appendix B: Figure 3.8 before pixel aggregation

Figure A.2 shows the smaller area shown in Figure 3.8 before pixel aggregation, i.e. at the resolution of the multi-looked Sentinel-1 SAR data (20 m $\times$ 22 m).
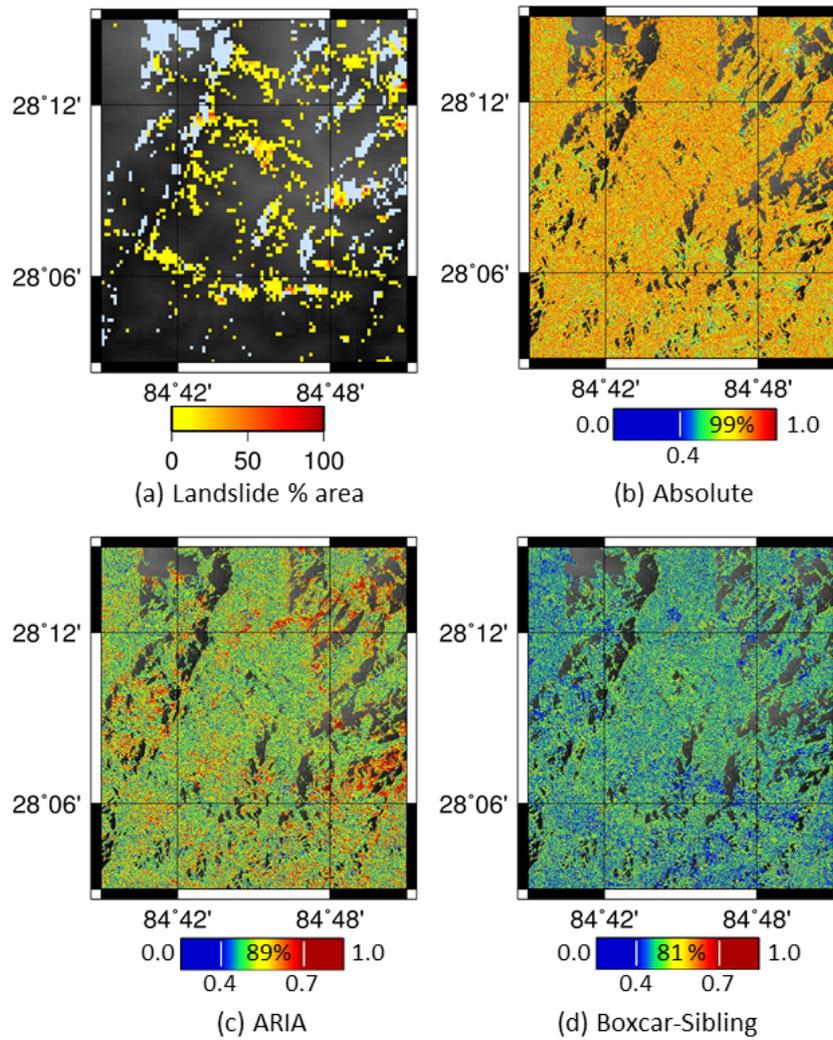
Figure A.2: (a) The percentage of each 10 x 10 aggregate pixel made up of landslide pixels (Roback et al., 2018). (b,c,d) The classifier value before aggregation for the surfaces produced by absolute, ARIA and Bx-S methods respectively. Each surface has been normalised to range between 0 and 1 with 1 most likely to be a landslide. Colour bars are non-linear, but linear between the white lines and labelled with the percentage of pixels across the whole area that lie in this linear range. The area shown corresponds to the smaller area shown in Figure 3.8

Bibliography

Y. Aimaiti, W. Liu, F. Yamazaki, and Y. Maruyama. Earthquake-Induced Landslide Mapping for the 2018 Hokkaido Eastern Iburi Earthquake Using PALSAR-2 Data. *Remote Sensing*, 11(20):2351, 2019.

K. E. Allstadt, R. W. Jibson, E. M. Thompson, C. I. Massey, D. J. Wald, J. W. Godt, and F. K. Rengers. Improving Near-Real-Time Coseismic Landslide Models: Lessons Learned from the 2016 Kaikōura, New Zealand, EarthquakeImproving Near-Real-Time Coseismic Landslide Models. *Bulletin of the Seismological Society of America*, 108(3B):1649–1664, 2018.

E. Antikidis, O. Arino, H. Laur, and A. Arnaud. Deforestation evaluation by synergetic use of ERS SAR coherence and ATSR hot spots- The Indonesian fire event of 1997. *Earth Observation Quarterly*, 59:34–38, 1998.

G. Aslan, M. Foumelis, D. Raucoules, M. De Michele, S. Bernardie, and Z. Cakir. Landslide Mapping and Monitoring Using Persistent Scatterer Interferometry (PSI) Technique in the French Alps. *Remote Sensing*, 12(8):1305, 2020.

T. C. Au. Random forests, decision trees, and categorical predictors: the "Absent levels" problem. *The Journal of Machine Learning Research*, 19(1):1737–1766, 2018.

J. Barlow, I. Barisin, N. Rosser, D. Petley, A. Densmore, and T. Wright. Seismically-induced mass movements and volumetric fluxes resulting from the 2010 Mw= 7.2 earthquake in the Sierra Cucapah, Mexico. *Geomorphology*, 230: 138–145, 2015.

S. Beguería. Validation and evaluation of predictive models in hazard assessment and risk management. *Natural Hazards*, 37(3):315–329, 2006.

R. Behling, S. Roessner, H. Kaufmann, and B. Kleinschmit. Automated spatiotemporal landslide mapping over large areas using rapideye time series data. *Remote Sensing*, 6(9):8026–8055, 2014.

D. P. Bekaert, A. L. Handwerger, P. Agram, and D. B. Kirschbaum. InSAR-based detection method for mapping and monitoring slow-moving landslides in remote regions with steep and mountainous terrain: An application to Nepal. *Remote Sensing of Environment*, 249:111983, 2020.

E. Bessette-Kirton, J. Coe, J. Kean, J. Godt, F. Rengers, W. Schulz, R. Baum, E. Jones, and D. Staley. Map data showing concentration of landslides caused by Hurricane Maria in Puerto Rico. *United States Geological Survey: Reston, VA, USA*, 2017.

E. K. Bessette-Kirton, C. Cerovski-Darriau, W. H. Schulz, J. A. Coe, J. W. Kean, J. W. Godt, M. A. Thomas, and K. S. Hughes. Landslides Triggered by Hurricane Maria: Assessment of an Extreme Event in Puerto Rico. *GSA Today*, 29(6), 2019.

X. Blaes and P. Defourny. Retrieving crop parameters based on tandem ERS 1/2 interferometric coherence images. *Remote Sensing of Environment*, 88(4):374–385, 2003.

R. Bonì, M. Bordoni, A. Colombo, L. Lanteri, and C. Meisina. Landslide state of activity maps by combining multi-temporal A-DInSAR (LAMBDA). *Remote sensing of environment*, 217:172–190, 2018.

A. Borghuis, K. Chang, and H. Lee. Comparison between automated and manual mapping of typhoon-triggered landslides from SPOT-5 imagery. *International Journal of Remote Sensing*, 28(8):1843–1856, 2007.

L. Breiman. Random forests. *Machine learning*, 45(1):5–32, 2001.

K. Burrows, R. J. Walters, D. Milledge, K. Spaans, and A. L. Densmore. A new method for large-scale landslide classification from satellite radar. *Remote Sensing*, 11(3):237, 2019.

K. Burrows, R. J. Walters, D. Milledge, and A. L. Densmore. A systematic exploration of satellite radar coherence methods for rapid landslide detection. *Natural Hazards and Earth System Sciences Discussions*, pages 1–26, 2020.

A. Cabré, D. Remy, G. Aguilar, S. Carretier, and R. Riquelme. Mapping rainstorm erosion associated with an individual storm from InSAR coherence loss validated by field evidence for the Atacama Desert. *Earth Surface Processes and Landforms*, 2020.

F. Catani, D. Lagomarsino, S. Segoni, and V. Tofani. Landslide susceptibility estimation by random forests technique: sensitivity and scaling issues. *Natural Hazards and Earth System Sciences*, 13(11):2815, 2013.

T. Chai and R. R. Draxler. Root mean square error (RMSE) or mean absolute error (MAE)?–Arguments against avoiding RMSE in the literature. *Geoscientific model development*, 7(3):1247–1250, 2014.

K.-T. Chang, S.-H. Chiang, and M.-L. Hsu. Modeling typhoon-and earthquake-induced landslides in a mountainous watershed using logistic regression. *Geomorphology*, 89(3-4):335–347, 2007.

E. Chaussard, F. Amelung, H. Abidin, and S.-H. Hong. Sinking cities in Indonesia: ALOS PALSAR detects rapid subsidence due to groundwater and gas extraction. *Remote sensing of environment*, 128:150–161, 2013.

W. Chen, X. Xie, J. Wang, B. Pradhan, H. Hong, D. T. Bui, Z. Duan, and J. Ma. A comparative study of logistic model tree, random forest, and classification and regression tree models for spatial prediction of landslide susceptibility. *Catena*, 151:147–160, 2017.

Y. Chen, G. Zhang, X. Ding, and Z. Li. Monitoring earth surface deformations with InSAR technology: principles and some critical issues. *Journal of Geospatial Engineering*, 2(1):3–22, 2000.

M. Chini, R. Pelich, L. Pulvirenti, N. Pierdicca, R. Hostache, and P. Matgen. Sentinel-1 InSAR coherence to detect floodwater in urban areas: Houston and Hurricane Harvey as a test case. *Remote Sensing*, 11(2):107, 2019.

S. R. Cloude and E. Pottier. A review of target decomposition theorems in radar polarimetry. *IEEE transactions on geoscience and remote sensing*, 34(2):498–518, 1996.

S. R. Cloude and E. Pottier. An entropy based classification scheme for land applications of polarimetric SAR. *IEEE transactions on geoscience and remote sensing*, 35(1):68–78, 1997.

B. D. Collins and R. W. Jibson. Assessment of existing and potential landslide hazards resulting from the April 25, 2015 Gorkha, Nepal earthquake sequence. Technical report, US Geological Survey, 2015.

D. Coltuc, P. Bolon, and J.-M. Chassery. Exact histogram specification. *IEEE Transactions on Image Processing*, 15(5):1143–1152, 2006.

P. Confuorto, D. Di Martire, G. Centolanza, R. Iglesias, J. J. Mallorqui, A. Novellino, S. Plank, M. Ramondini, K. Thuro, and D. Calcaterra. Post-failure evolution analysis of a rainfall-triggered landslide by multi-temporal interferometry SAR approaches integrated with geotechnical analysis. *Remote sensing of environment*, 188:51–72, 2017.

P. Cui, Y.-y. Zhu, Y.-s. Han, X.-q. Chen, and J.-q. Zhuang. The 12 May Wenchuan earthquake-induced landslide lakes: distribution and preliminary risk evaluation. *Landslides*, 6(3):209–223, 2009.

K. R. Czuchlewski, J. K. Weissel, and Y. Kim. Polarimetric synthetic aperture radar study of the Tsaoling landslide generated by the 1999 Chi-Chi earthquake, Taiwan. *Journal of Geophysical Research: Earth Surface*, 108(F1), 2003.

M. P. Dahlquist and A. J. West. Initiation and runout of post-seismic debris flows: Insights from the 2015 Gorkha Earthquake. *Geophysical Research Letters*, 2019.

K. Dai, Z. Li, R. Tomás, G. Liu, B. Yu, X. Wang, H. Cheng, J. Chen, and J. Stockamp. Monitoring activity at the Daguangbao mega-landslide (China) using Sentinel-1 TOPS time series interferometry. *Remote Sensing of Environment*, 186:501–513, 2016.

A. Datta, S. Sigdel, K. Oven, N. Rosser, A. Densmore, and S. Rijal. The role of scientific evidence during the 2015 Nepal earthquake relief effort. *Overseas Development Institute Report, London: UK.*, 2018.

A. A. Deijns, A. R. Bevington, F. van Zadelhoff, S. M. de Jong, M. Geertsema, and S. McDougall. Semi-automated detection of landslide timing using harmonic modelling of satellite imagery, Buckinghorse River, Canada. *International Journal of Applied Earth Observation and Geoinformation*, 84:101943, 2020.

C.-A. Deledalle, L. Denis, F. Tupin, A. Reigber, and M. Jäger. NL-SAR: A unified nonlocal framework for resolution-preserving (Pol)(In) SAR denoising. *IEEE Transactions on Geoscience and Remote Sensing*, 53(4):2021–2038, 2014.

R. Díaz-Uriarte and S. A. De Andres. Gene selection and classification of microarray data using random forest. *BMC bioinformatics*, 7(1):3, 2006.

A. M. Dixit, A. T. Ringler, D. F. Sumy, E. S. Cochran, S. E. Hough, S. S. Martin, S. Gibbons, J. H. Luetgert, J. Galetzka, S. N. Shrestha, et al. Strong-motion observations of the M 7.8 Gorkha, Nepal, earthquake sequence and development of the N-SHAKE strong-motion network. *Seismological Research Letters*, 86(6): 1533–1539, 2015.

B. Efron and R. Tibshirani. Improvements on cross-validation: the 632+ bootstrap method. *Journal of the American Statistical Association*, 92(438):548–560, 1997.

ESA. Land Cover CCI Product User Guide Version 2. `maps.elie.ucl.ac.be/CCI/viewer/download/ESACCI-LC-Ph2-PUGv2_2.0.pdf`, 2017.

ESA. Sentinel-1 Constellation Observation Scenario: Revisit and Coverage Frequency. `https://sentinel.esa.int/web/sentinel/missions/sentinel-1/observation-scenario`, 2019.

T. G. Farr, P. A. Rosen, E. Caro, R. Crippen, R. Duren, S. Hensley, M. Kobrick, M. Paller, E. Rodriguez, L. Roth, et al. The shuttle radar topography mission. *Reviews of geophysics*, 45(2), 2007.

M. Ferrario. Landslides triggered by multiple earthquakes: insights from the 2018 Lombok (Indonesia) events. *Natural Hazards*, pages 1–18, 2019.

A. Ferretti, A. Fumagalli, F. Novali, C. Prati, F. Rocca, and A. Rucci. A new algorithm for processing interferometric data-stacks: SqueeSAR. *IEEE Transactions on Geoscience and Remote Sensing*, 49(9):3460–3470, 2011.

F. Fiedrich, F. Gehbauer, and U. Rickers. Optimized resource allocation for emergency response after earthquake disasters. *Safety science*, 35(1-3):41–57, 2000.

E. J. Fielding, M. Talebian, P. A. Rosen, H. Nazari, J. A. Jackson, M. Ghorashi, and R. Walker. Surface ruptures and building damage of the 2003 Bam, Iran, earthquake mapped by satellite synthetic aperture radar interferometric correlation. *Journal of Geophysical Research: Solid Earth*, 110(B3), 2005.

G. Franceschetti, R. Marino, M. Migliaccio, and D. Riccio. SAR simulation of three-dimensional scenes. In *SAR Data Processing for Remote Sensing*, volume 2316, pages 192–202. International Society for Optics and Photonics, 1994.

J. E. Fransson, A. Pantze, L. E. Eriksson, M. J. Soja, and M. Santoro. Mapping of wind-thrown forests using satellite SAR images. In *2010 IEEE International Geoscience and Remote Sensing Symposium*, pages 1242–1245. IEEE, 2010.

A. Freeman and S. L. Durden. A three-component scattering model for polarimetric SAR data. *IEEE Transactions on Geoscience and Remote Sensing*, 36(3):963–973, 1998.

O. Frey, M. Santoro, C. L. Werner, and U. Wegmuller. DEM-based SAR pixel area estimation for enhanced geocoding refinement and radiometric normalization. In *Fringe 2011*, volume 697, page 76, 2012.

N. V. Frith, R. G. Hilton, J. D. Howarth, D. R. Gröcke, S. J. Fitzsimons, T. Croissant, J. Wang, E. L. McClymont, J. Dahl, and A. L. Densmore. Carbon export from mountain forests enhanced by earthquake-triggered landslides over millennia. *Nature Geoscience*, 11(10):772–776, 2018.

S. Fujiwara, T. Nakano, Y. Morishita, T. Kobayashi, H. Yarai, H. Une, and K. Hayashi. Detection and interpretation of local surface deformation from the 2018 Hokkaido Eastern Iburi Earthquake using ALOS-2 SAR data. *Earth, Planets and Space*, 71(1):64, 2019.

G. J. Funning, B. Parsons, T. J. Wright, J. A. Jackson, and E. J. Fielding. Surface displacements and source parameters of the 2003 Bam (Iran) earthquake from Envisat advanced synthetic aperture radar imagery. *Journal of Geophysical Research: Solid Earth*, 110(B9), 2005.

S. F. Gallen, M. K. Clark, J. W. Godt, K. Roback, and N. A. Niemi. Application and evaluation of a rapid response earthquake-triggered landslide model to the 25 April 2015 Mw 7.8 Gorkha earthquake, Nepal. *Tectonophysics*, 714:173–187, 2017.

GDAL/OGR contributors. *GDAL/OGR Geospatial Data Abstraction software Library*. Open Source Geospatial Foundation, 2020. URL `https://gdal.org`.

P. Ge, H. Gokon, K. Meguro, and S. Koshimura. Study on the Intensity and Coherence Information of High-Resolution ALOS-2 SAR Images for Rapid Massive Landslide Mapping at a Pixel Level. *Remote Sensing*, 11(23):2808, 2019.

O. Ghorbanzadeh, T. Blaschke, K. Gholamnia, S. R. Meena, D. Tiede, and J. Aryal. Evaluation of different machine learning methods and deep-learning convolutional neural networks for landslide detection. *Remote Sensing*, 11(2):196, 2019.

Global Logistics Cluster. Nepal Lessons Learned Report. `http://www.logcluster.org/global-meeting-document/nepal-lessons-learned-report`, 2015. Accessed on 19 June 2017.

A. Goorabi. Detection of landslide induced by large earthquake using insar coherence techniques–northwest zagros, iran. *The Egyptian Journal of Remote Sensing and Space Science*, 2019.

T. Guneriussen, K. A. Hogda, H. Johnsen, and I. Lauknes. InSAR for estimation of changes in snow water equivalent of dry snow. *IEEE Transactions on Geoscience and Remote Sensing*, 39(10):2101–2108, 2001.

A. L. Handwerger, E. J. Fielding, M.-H. Huang, G. L. Bennett, C. Liang, and W. H. Schulz. Widespread initiation, reactivation, and acceleration of landslides in the northern California Coast Ranges due to extreme rainfall. *Journal of Geophysical Research: Earth Surface*, 2019.

J. A. Hanley and B. J. McNeil. The meaning and use of the area under a receiver operating characteristic (ROC) curve. *Radiology*, 143(1):29–36, 1982.

R. F. Hanssen. *Radar interferometry: data interpretation and error analysis*, volume 2. Springer Science & Business Media, 2001.

E. L. Harp, D. K. Keefer, H. P. Sato, and H. Yagi. Landslide inventories: the essential part of seismic landslide hazard analyses. *Engineering Geology*, 122 (1-2):9–21, 2011.

J. Hartmann and N. Moosdorf. The new global lithological map database GLiM: A representation of rock properties at the Earth surface. *Geochemistry, Geophysics, Geosystems*, 13(12), 2012.

S. Heleno, M. Matias, P. Pina, and A. J. Sousa. Semiautomated object-based classification of rain-induced landslides with VHR multispectral images on Madeira Island. *Nat. Hazards Earth Syst. Sci*, 16:1035–1048, 2016.

E. W. Hoen and H. A. Zebker. Penetration depths inferred from interferometric volume decorrelation observed over the Greenland ice sheet. *IEEE Transactions on Geoscience and Remote Sensing*, 38(6):2571–2583, 2000.

H. Hong, C. Xu, and D. T. Bui. Landslide susceptibility assessment at the xiushui area (china) using frequency ratio model. *Procedia Earth and Planetary Science*, 15:513–517, 2015.

X. Hu, R. Bürgmann, Z. Lu, A. L. Handwerger, T. Wang, and R. Miao. Mobility, thickness, and hydraulic diffusivity of the slow-moving Monroe landslide in California revealed by L-band satellite radar interferometry. *Journal of Geophysical Research: Solid Earth*, 124(7):7504–7518, 2019.

Y. Huang, W. Chen, and J. Liu. Secondary geological hazard analysis in beichuan after the wenchuan earthquake and recommendations for reconstruction. *Environmental Earth Sciences*, 66(4):1001–1009, 2012.

E. Hussain, A. Hooper, T. J. Wright, R. J. Walters, and D. P. Bekaert. Interseismic strain accumulation across the central North Anatolian Fault from iteratively unwrapped InSAR measurements. *Journal of Geophysical Research: Solid Earth*, 121(12):9000–9019, 2016.

ICEYE. New benchmark in imaging from SAR microsatellites: ICEYE presents 25 cm resolution. `https://www.iceye.com/satellite-data/blog/new-benchmark-in-imaging-from-sar-microsatellites-iceye-presents-25-cm-azimuth-re`, 2020. Accessed 22nd October 2020.

ICIMOD. Snow cover statistic - Nepal. `http://www.icimod.org/?q=10216`, 2013.

Inter-Agency Standing Committee. Multi-Sector Initial Rapid Asessment Guidance. `https://www.humanitarianresponse.info/en/programme-cycle/space/document/multi-sector-initial-rapid-assessment-guidance-revision-july-2015`, 2015. Accessed on 16 October 2018.

JAXA. High-Resolution Land Use and Land Cover 30m resolution map of Japan [2014-2016]. `https://www.eorc.jaxa.jp/ALOS/en/lulc/lulc_index.html`, 2018. Version 18.03.

JAXA. ALOS-2 project / PALSAR-2. `https://www.eorc.jaxa.jp/ALOS-2/en/about/palsar2.htm`, 2020. Accessed 23rd July 2020.

G. Jia, Q. Tang, and X. Xu. Evaluating the performances of satellite-based rainfall data for global rainfall-induced landslide warnings. *Landslides*, 17(2):283–299, 2020.

J. Jung and S.-H. Yun. A Hybrid Damage Detection Approach Based on Multi-Temporal Coherence and Amplitude Analysis for Disaster Response. In *IG-ARSS 2019-2019 IEEE International Geoscience and Remote Sensing Symposium*, pages 9330–9333. IEEE, 2019.

J. Jung, D.-j. Kim, M. Lavalle, and S.-H. Yun. Coherent change detection using insar temporal decorrelation model: A case study for volcanic ash detection. *IEEE Transactions on Geoscience and Remote Sensing*, 54(10):5765–5775, 2016.

J. S. Kargel, G. J. Leonard, D. H. Shugar, U. K. Haritashya, A. Bevington, E. Fielding, K. Fujita, M. Geertsema, E. Miles, J. Steiner, et al. Geomorphic and geologic controls of geohazards induced by Nepal's 2015 Gorkha earthquake. *Science*, 351 (6269):aac8353, 2016.

D. K. Keefer. Landslides caused by earthquakes. *Geological Society of America Bulletin*, 95(4):406–421, 1984.

D. Kirschbaum and T. Stanley. Satellite-based assessment of rainfall-triggered landslide hazard for situational awareness. *Earth's future*, 6(3):505–523, 2018.

T. Konishi and Y. Suga. Landslide detection using COSMO-SkyMed images: a case study of a landslide event on Kii Peninsula, Japan. *European Journal of Remote Sensing*, 51(1):205–221, 2018.

T. Konishi and Y. Suga. Landslide detection with ALOS-2/PALSAR-2 data using convolutional neural networks: a case study of 2018 Hokkaido Eastern Iburi earthquake. In *Proc. of SPIE Vol*, volume 11154, pages 111540H–1, 2019.

J. T. Koskinen, J. T. Pulliainen, and M. T. Hallikainen. The use of ERS-1 SAR data in snow melt monitoring. *IEEE Transactions on geoscience and remote sensing*, 35(3):601–610, 1997.

T. Kritikos, T. R. Robinson, and T. R. Davies. Regional coseismic landslide hazard assessment without historical landslide inventories: A new approach. *Journal of Geophysical Research: Earth Surface*, 120(4):711–729, 2015.

M. Lazeckỳ, K. Spaans, P. J. González, Y. Maghsoudi, Y. Morishita, F. Albino, J. Elliott, N. Greenall, E. Hatton, A. Hooper, et al. Licsar: An automatic insar tool for measuring and monitoring tectonic and volcanic activity. *Remote Sensing*, 12(15):2430, 2020.

G. Li, A. J. West, A. L. Densmore, Z. Jin, R. N. Parker, and R. G. Hilton. Seismic mountain building: Landslides associated with the 2008 Wenchuan earthquake in the context of a generalized model for earthquake volume balance. *Geochemistry, Geophysics, Geosystems*, 15(4):833–844, 2014.

G. Li, A. J. West, A. L. Densmore, D. E. Hammond, Z. Jin, F. Zhang, J. Wang, and R. G. Hilton. Connectivity of earthquake-triggered landslides with the fluvial network: Implications for landslide sediment transport after the 2008 Wenchuan earthquake. *Journal of Geophysical Research: Earth Surface*, 121(4):703–724, 2016.

A. Liaw, M. Wiener, et al. Classification and regression by randomForest. *R news*, 2(3):18–22, 2002.

Z. Lu and O.-i. Kwoun. Radarsat-1 and ERS InSAR analysis over southeastern coastal Louisiana: Implications for mapping water-level changes beneath swamp forests. *IEEE Transactions on Geoscience and Remote Sensing*, 46(8):2167–2184, 2008.

K. D. Marano, D. J. Wald, and T. I. Allen. Global earthquake casualties due to secondary effects: a quantitative analysis for improving rapid loss analyses. *Natural hazards*, 52(2):319–328, 2010.

O. Marc and N. Hovius. Amalgamation in landslide maps: effects and automatic detection. *Natural Hazards & Earth System Sciences*, 15(4), 2015.

O. Marc, R. Behling, C. Andermann, J. Turowski, L. Illien, S. Roessner, and N. Hovius. Long-term erosion of the Nepal Himalayas by bedrock landsliding: the role of monsoons, earthquakes and giant landslides. *Earth Surface Dynamics*, 7:107–128, 2019.

T. R. Martha, P. Roy, R. Mazumdar, K. B. Govindharaj, and K. V. Kumar. Spatial characteristics of landslides triggered by the 2015 M w 7.8 (Gorkha) and M w 7.3 (Dolakha) earthquakes in Nepal. *Landslides*, 14(2):697–704, 2017.

S. Martinis, J. Kersten, and A. Twele. A fully automated TerraSAR-X based flood service. *ISPRS Journal of Photogrammetry and Remote Sensing*, 104:203–212, 2015.

O. Masato, T. Abe, T. Takeo, and S. Masanobu. Landslide detection in mountainous forest areas using polarimetry and interferometric coherence. *Earth, Planets and Space (Online)*, 72(1), 2020.

F. Meyer. Spaceborne synthetic aperture radar: principles, data access and basic processing techniques. In A. I. Flores-Anderson, K. E. Herndon, R. B. Thapa, and E. Cherrington, editors, *The SAR Handbook: Comprehensive Methodologies for Forest Monitoring and Biomass Estimation*. SERVIR, 2019.

F. Meyer, D. McAlpin, W. Gong, O. Ajadi, S. Arko, P. Webley, and J. Dehn. Integrating SAR and derived products into operational volcano monitoring and decision support systems. *ISPRS journal of photogrammetry and remote sensing*, 100:106–117, 2015.

A. C. Mondini, M. Santangelo, M. Rocchetti, E. Rossetto, A. Manconi, and O. Monserrat. Sentinel-1 SAR Amplitude Imagery for Rapid Landslide Detection. *Remote Sensing*, 11(7):760, 2019.

A. Moreira, P. Prats-Iraola, M. Younis, G. Krieger, I. Hajnsek, and K. P. Papathanassiou. A tutorial on synthetic aperture radar. *IEEE Geoscience and remote sensing magazine*, 1(1):6–43, 2013.

M. Mulas, A. Corsini, G. Cuozzo, M. Callegari, B. Thiebes, and V. Mair. Quantitative monitoring of surface movements on active landslides by multi-temporal, high-resolution X-Band SAR amplitude information: Preliminary results. In *12th International Symposium on Landslides (Napoli, Italy, 12-19 June 2016)*, volume 2, pages 1511–1516. CRC Press 2016, 2016.

F. Nadim, O. Kjekstad, P. Peduzzi, C. Herold, and C. Jaedicke. Global landslide and avalanche hotspots. *Landslides*, 3(2):159–173, 2006.

NASA. Advanced Rapid Imaging and Analysis (ARIA) Project for Natural Hazards. `https://aria.jpl.nasa.gov/`, 2018. Accessed on 27 June 2018.

G. Nico, M. Pappalepore, G. Pasquariello, A. Refice, and S. Samarelli. Comparison of SAR amplitude vs. coherence flood detection methods-a GIS application. *International Journal of Remote Sensing*, 21(8):1619–1631, 2000.

M. Nolan and D. R. Fatland. Penetration depth as a DInSAR observable and proxy for soil moisture. *IEEE Transactions on Geoscience and Remote Sensing*, 41(3): 532–537, 2003.

M. A. Nowicki, D. J. Wald, M. W. Hamburger, M. Hearne, and E. M. Thompson. Development of a globally applicable model for near real-time prediction of seismically induced landslides. *Engineering geology*, 173:54–65, 2014.

M. Nowicki Jessee, M. Hamburger, K. Allstadt, D. J. Wald, S. Robeson, H. Tanyas, M. Hearne, and E. Thompson. A Global Empirical Model for Near-Real-Time Assessment of Seismically Induced Landslides. *Journal of Geophysical Research: Earth Surface*, 123(8):1835–1859, 2018.

M. A. Nowicki Jessee, M. Hamburger, M. Ferrara, A. McLean, and C. FitzGerald. A global dataset and model of earthquake-induced landslide fatalities. *Landslides*, pages 1–14, 2020.

S. Olen and B. Bookhagen. Mapping damage-affected areas after natural hazard events using Sentinel-1 coherence time series. *Remote Sensing*, 10(8):1272, 2018.

S. Olen and B. Bookhagen. Applications of sar interferometric coherence time series: Spatiotemporal dynamics of geomorphic transitions in the south-central andes. *Journal of Geophysical Research: Earth Surface*, 125(3):e2019JF005141, 2020.

S.-E. Park and S.-G. Lee. On the use of single-, dual-, and quad-polarimetric SAR observation for landslide detection. *ISPRS International Journal of Geo-Information*, 8(9):384, 2019.

F. Pedregosa, G. Varoquaux, A. Gramfort, V. Michel, B. Thirion, O. Grisel, M. Blondel, P. Prettenhofer, R. Weiss, V. Dubourg, J. Vanderplas, A. Passos, D. Cournapeau, M. Brucher, M. Perrot, and E. Duchesnay. Scikit-learn: Machine learning in Python. *Journal of Machine Learning Research*, 12:2825–2830, 2011.

D. Petley. Global patterns of loss of life from landslides. *Geology*, 40(10):927–930, 2012.

N. Pierdicca, M. Davidson, M. Chini, W. Dierking, S. Djavidnia, J. Haarpaintner, G. Hajduch, G. V. Laurin, M. Lavalle, C. López-Martínez, et al. The Copernicus L-band SAR mission ROSE-L (Radar Observing System for Europe)(Conference Presentation). In *Active and Passive Microwave Remote Sensing for Environmental Monitoring III*, volume 11154, page 111540E. International Society for Optics and Photonics, 2019.

D. Reale, D. O. Nitti, D. Peduto, R. Nutricato, F. Bovenga, and G. Fornaro. Postseismic deformation monitoring with the COSMO/SKYMED constellation. *IEEE Geoscience and Remote Sensing Letters*, 8(4):696–700, 2011.

W. Rees. Technical note: Simple masks for shadowing and highlighting in SAR images. *International Journal of Remote Sensing*, 21(11):2145–2152, 2000.

P. Reichenbach, M. Rossi, B. D. Malamud, M. Mihir, and F. Guzzetti. A review of statistically-based landslide susceptibility models. *Earth-science reviews*, 180: 60–91, 2018.

C. Reyes-Carmona, A. Barra, J. P. Galve, O. Monserrat, J. V. Pérez-Peña, R. M. Mateos, D. Notti, P. Ruano, A. Millares, J. López-Vinielles, et al. Sentinel-1 dinsar for monitoring active landslides in critical infrastructures: The case of the rules reservoir (southern spain). *Remote Sensing*, 12(5):809, 2020.

K. Roback, M. K. Clark, A. J. West, D. Zekkos, G. Li, S. F. Gallen, D. Chamlagain, and J. W. Godt. The size, distribution, and mobility of landslides caused by the 2015 Mw7. 8 Gorkha earthquake, Nepal. *Geomorphology*, 301:121–138, 2018.

T. R. Robinson, N. J. Rosser, A. L. Densmore, J. G. Williams, M. E. Kincey, J. Benjamin, and H. J. Bell. Rapid post-earthquake modelling of coseismic landsliding intensity and distribution for emergency response decision support. *Natural hazards and earth system sciences.*, 17(9):1521–1540, 2017.

T. R. Robinson, N. J. Rosser, T. R. Davies, T. M. Wilson, and C. Orchiston. Near-Real-Time Modeling of Landslide Impacts to Inform Rapid Response: An Example from the 2016 Kaikōura, New Zealand, EarthquakeNear-Real-Time Modeling of Landslide Impacts to Inform Rapid Response. *Bulletin of the Seismological Society of America*, 108(3B):1665–1682, 2018.

T. R. Robinson, N. Rosser, and R. J. Walters. The Spatial and Temporal Influence of Cloud Cover on Satellite-Based Emergency Mapping of Earthquake Disasters. *Scientific Reports*, 9(1):1–9, 2019.

P. A. Rosen, S. Hensley, I. R. Joughin, F. K. Li, S. N. Madsen, E. Rodriguez, and R. M. Goldstein. Synthetic aperture radar interferometry. *Proceedings of the IEEE*, 88(3):333–382, 2000.

A. Rosi, V. Tofani, L. Tanteri, C. T. Stefanelli, A. Agostini, F. Catani, and N. Casagli. The new landslide inventory of Tuscany (Italy) updated with PS-InSAR: geomorphological features and landslide distribution. *Landslides*, 15(1): 5–19, 2018.

M. Rüetschi, D. Small, and L. T. Waser. Rapid detection of windthrows using Sentinel-1 C-band SAR data. *Remote Sensing*, 11(2):115, 2019.

T. Saito and M. Rehmsmeier. The precision-recall plot is more informative than the roc plot when evaluating binary classifiers on imbalanced datasets. *PloS one*, 10(3):e0118432, 2015.

G. Scaringi, X. Fan, Q. Xu, C. Liu, C. Ouyang, G. Domènech, F. Yang, and L. Dai. Some considerations on the use of numerical methods to simulate past landslides and possible new failures: the case of the recent Xinmo landslide (Sichuan, China). *Landslides*, 15(7):1359–1375, 2018.

C. Scott, R. Lohman, and T. Jordan. InSAR constraints on soil moisture evolution after the March 2015 extreme precipitation event in Chile. *Scientific reports*, 7 (1):4903, 2017.

X. Shan, J. Ma, C. Wang, J. Liu, X. Song, and G. Zhang. Co-seismic ground deformation and source parameters of Mani M7.9 earthquake inferred from spaceborne D-InSAR observation data. *Science in China Series D: Earth Sciences*, 47(6):481–488, 2004.

P. Sharma. Updates in Commissioning Timeline for NASA-ISRO Synthetic Aperture Radar (NISAR). In *2019 IEEE Aerospace Conference*, pages 1–12. IEEE, 2019.

X. Shi, L. Zhang, M. Liao, and T. Balz. Deformation monitoring of slow-moving landslide with L-and C-band SAR interferometry. *Remote sensing letters*, 5(11): 951–960, 2014.

X. Shi, L. Zhang, Y. Zhong, L. Zhang, and M. Liao. Detection and characterization of active slope deformations with Sentinel-1 InSAR analyses in the Southwest Area of Shanxi, China. *Remote Sensing*, 12(3):392, 2020.

L. Solari, M. Del Soldato, F. Raspini, A. Barra, S. Bianchini, P. Confuorto, N. Casagli, and M. Crosetto. Review of Satellite Interferometry for Landslide Detection in Italy. *Remote Sensing*, 12(8):1351, 2020.

K. Spaans and A. Hooper. InSAR processing for volcano monitoring and other near-real time applications. *Journal of Geophysical Research: Solid Earth*, 121 (4):2947–2960, 2016.

T. Strozzi, P. Farina, A. Corsini, C. Ambrosi, M. Thüring, J. Zilger, A. Wiesmann, U. Wegmüller, and C. Werner. Survey and monitoring of landslide displacements by means of L-band satellite SAR interferometry. *Landslides*, 2(3):193–201, 2005.

T. Strozzi, J. Klimeš, H. Frey, R. Caduff, C. Huggel, U. Wegmüller, and A. C. Rapre. Satellite SAR interferometry for the improved assessment of the state of activity of landslides: A case study from the Cordilleras of Peru. *Remote sensing of environment*, 217:111–125, 2018.

S. Takeuchi and S. Yamada. Monitoring of forest fire damage by using JERS-1 InSAR. In *IEEE International Geoscience and Remote Sensing Symposium*, volume 6, pages 3290–3292. IEEE, 2002.

M. A. Tanase, M. Santoro, U. Wegmüller, J. de la Riva, and F. Pérez-Cabello. Properties of X-, C-and L-band repeat-pass interferometric SAR coherence in Mediterranean pine forests affected by fires. *Remote Sensing of Environment*, 114(10):2182–2194, 2010.

H. Tanyas, M. Rossi, M. Alvioli, C. J. van Westen, and I. Marchesini. A global slope unit-based method for the near real-time prediction of earthquake-induced landslides. *Geomorphology*, 327:126–146, 2019.

The British Geological Survey. Ecuador disaster response 2016. `http://www.bgs.ac.uk/research/earthHazards/epom/ecuadorEarthquake.html`, 2016. Accessed on 8 July 2018.

E. M. Thompson, S. K. McBride, G. P. Hayes, K. E. Allstadt, L. A. Wald, D. J. Wald, K. L. Knudsen, C. B. Worden, K. D. Marano, R. W. Jibson, et al. Usgs near-real-time products—and their use—for the 2018 anchorage earthquake. *Seismological Research Letters*, 91(1):94–113, 2020.

R. Torres, S. Lokas, G. Di Cosimo, D. Geudtner, and D. Bibby. Sentinel 1 evolution: Sentinel-1C and-1D models. In *2017 IEEE International Geoscience and Remote Sensing Symposium (IGARSS)*, pages 5549–5550. IEEE, 2017.

UNAVCO. Synthetic Aperture Radar (SAR) satellites. `https://www.unavco.org/instrumentation/geophysical/imaging/sar-satellites/sar-satellites.html`, 2019. Accessed on 6 July 2020.

S. Vajedian, M. Motagh, Z. Mousavi, K. Motaghi, E. Fielding, B. Akbari, H.-U. Wetzel, and A. Darabi. Coseismic deformation field of the MW 7.3 12 November 2017 Sarpol-e Zahab (Iran) earthquake: A decoupling horizon in the northern Zagros Mountains inferred from InSAR observations. *Remote Sensing*, 10(10): 1589, 2018.

V. Vakhshoori and M. Zare. Is the roc curve a reliable tool to compare the validity of landslide susceptibility maps? *Geomatics, Natural Hazards and Risk*, 9(1): 249–266, 2018.

D. J. Varnes. Slope movement types and processes. *Special report*, 176:11–33, 1978.

F. Wang, X. Fan, A. P. Yunus, S. S. Subramanian, A. Alonso-Rodriguez, L. Dai, Q. Xu, and R. Huang. Coseismic landslides triggered by the 2018 Hokkaido, Japan (M w 6.6), earthquake: spatial distribution, controlling factors, and possible failure mechanism. *Landslides*, 16(8):1551–1566, 2019.

U. Wegnüller, C. Werner, T. Strozzi, A. Wiesmann, O. Frey, and M. Santoro. Sentinel-1 support in the gamma software. *Procedia Computer Science*, 100: 1305–1312, 12 2016. doi: 10.1016/j.procs.2016.09.246.

J. G. Williams, N. J. Rosser, M. E. Kincey, J. Benjamin, K. J. Oven, A. L. Densmore, D. G. Milledge, T. R. Robinson, C. A. Jordan, and T. A. Dijkstra. Satellite-based emergency mapping using optical imagery: experience and reflections from the 2015 Nepal earthquakes. *Natural hazards and earth system sciences.*, 18:185–205, 2018.

T. J. Wright, B. E. Parsons, and Z. Lu. Toward mapping surface deformation in three dimensions using InSAR. *Geophysical Research Letters*, 31(1), 2004.

C. Xu, X. Xu, Y. Tian, L. Shen, Q. Yao, X. Huang, J. Ma, X. Chen, and S. Ma. Two comparable earthquakes produced greatly different coseismic landslides: The 2015 Gorkha, Nepal and 2008 Wenchuan, China events. *Journal of Earth Science*, 27(6):1008–1015, 2016.

C. Xu, S. Ma, Z. Tan, C. Xie, S. Toda, and X. Huang. Landslides triggered by the 2016 Mj 7.3 Kumamoto, Japan, earthquake. *Landslides*, 15(3):551–564, 2018.

H. Yamagishi and F. Yamazaki. Landslides by the 2018 Hokkaido Iburi-Tobu Earthquake on September 6. *Landslides*, 15(12):2521–2524, 2018.

Y. Yamaguchi, T. Moriyama, M. Ishido, and H. Yamada. Four-component scattering model for polarimetric SAR image decomposition. *IEEE Transactions on Geoscience and Remote Sensing*, 43(8):1699–1706, 2005.

Y. Yamaguchi, M. Umemura, D. Kanai, K. Miyazaki, and H. Yamada. ALOS-2 polarimetric SAR observation of Hokkaido-Iburi-Tobu earthquake 2018. *IEICE Communications Express*, 8(2):26–31, 2019.

C. Yonezawa and S. Takeuchi. Decorrelation of SAR data by urban damages caused by the 1995 Hyogoken-nanbu earthquake. *International Journal of Remote Sensing*, 22(8):1585–1600, 2001.

S.-H. Yun, E. Fielding, F. Webb, and M. Simons. Damage proxy map from interferometric synthetic aperture radar coherence. U.S. Patent 9,207,318, 2012.

S.-H. Yun, K. Hudnut, S. Owen, F. Webb, M. Simons, P. Sacco, E. Gurrola, G. Manipon, C. Liang, E. Fielding, et al. Rapid Damage Mapping for the 2015 M w 7.8 Gorkha Earthquake Using Synthetic Aperture Radar Data from COSMO–SkyMed and ALOS-2 Satellites. *Seismological Research Letters*, 86(6):1549–1556, 2015.

H. A. Zebker and J. Villasenor. Decorrelation in interferometric radar echoes. *IEEE Transactions on geoscience and remote sensing*, 30(5):950–959, 1992.

S. Zhang, R. Li, F. Wang, and A. Iio. Characteristics of landslides triggered by the 2018 Hokkaido Eastern Iburi earthquake, Northern Japan. *Landslides*, pages 1–18, 2019.

A. Ziegler and I. R. König. Mining data with random forests: current options for real-world applications. *Wiley Interdisciplinary Reviews: Data Mining and Knowledge Discovery*, 4(1):55–63, 2014.

M. Zink, G. Krieger, H. Fiedler, and A. Moreira. The TanDEM-X Mission Concept. *Proceedings of the European Conference on Synthetic Aperture Radar (EUSAR)*, 2008.

Colophon